

University of Alberta

The binary phase behaviour of positional isomers of triacylglycerols

by

Marc Vedantprakash Boodhoo



A thesis submitted to the Faculty of Graduate Studies and Research
in partial fulfillment of the requirements for the degree of

Master Degree
in
Food Science and Technology

Department of Agricultural, Food and Nutritional Science

Edmonton, Alberta
Fall 2007



Library and
Archives Canada

Bibliothèque et
Archives Canada

Published Heritage
Branch

Direction du
Patrimoine de l'édition

395 Wellington Street
Ottawa ON K1A 0N4
Canada

395, rue Wellington
Ottawa ON K1A 0N4
Canada

Your file *Votre référence*
ISBN: 978-0-494-33204-7
Our file *Notre référence*
ISBN: 978-0-494-33204-7

NOTICE:

The author has granted a non-exclusive license allowing Library and Archives Canada to reproduce, publish, archive, preserve, conserve, communicate to the public by telecommunication or on the Internet, loan, distribute and sell theses worldwide, for commercial or non-commercial purposes, in microform, paper, electronic and/or any other formats.

The author retains copyright ownership and moral rights in this thesis. Neither the thesis nor substantial extracts from it may be printed or otherwise reproduced without the author's permission.

AVIS:

L'auteur a accordé une licence non exclusive permettant à la Bibliothèque et Archives Canada de reproduire, publier, archiver, sauvegarder, conserver, transmettre au public par télécommunication ou par l'Internet, prêter, distribuer et vendre des thèses partout dans le monde, à des fins commerciales ou autres, sur support microforme, papier, électronique et/ou autres formats.

L'auteur conserve la propriété du droit d'auteur et des droits moraux qui protègent cette thèse. Ni la thèse ni des extraits substantiels de celle-ci ne doivent être imprimés ou autrement reproduits sans son autorisation.

In compliance with the Canadian Privacy Act some supporting forms may have been removed from this thesis.

Conformément à la loi canadienne sur la protection de la vie privée, quelques formulaires secondaires ont été enlevés de cette thèse.

While these forms may be included in the document page count, their removal does not represent any loss of content from the thesis.

Bien que ces formulaires aient inclus dans la pagination, il n'y aura aucun contenu manquant.


Canada

ABSTRACT

One method of producing low *trans* margarines and shortenings is by random chemical interesterification. This process introduces positional isomers of triacylglycerols (TAGs), which may be implicated in the formation of undesirable eutectics. This study investigated the polymorphism, melting and crystallization behavior, microstructure and relative hardness of three binary systems of positional isomers, namely 1, 3 dilauroyl-2-stearoyl *-sn-* glycerol (LSL)/1, 2-dilauroyl-3-stearoyl *-sn-* glycerol (LLS), 1, 3 dimyristoyl-2-stearoyl *-sn-* glycerol (MSM)/ 1, 2-dimyristoyl-3-stearoyl *-sn-* glycerol (MMS) and 1, 3 dipalmitoyl-2-stearoyl *-sn-* glycerol (PSP)/1, 2-dimyristoyl-3-stearoyl *-sn-* glycerol (PPS) as a function of two crystallization rates. These TAGs are likely to be formed in formulations utilizing fully hydrogenated Canola oil and palm or coconut oils. It is proposed that since TAGs generally crystallize in metastable states, depressions or eutectics may be shifted or mitigated using a processing solution. In this study, eutectic behaviour was observed for the LSL/LLS and PSP/PPS systems, while a monotectic behavior was observed for the MSM/MMS system. Depressions in solid fat content and relative hardness were encountered which did not correlate with the eutectic point but the composition at which they occurred was dependent upon crystallization rate.

ACKNOWLEDGEMENTS

I would like to express my sincere gratitude to my academic supervisor Dr. Suresh Narine for his guidance, constructive advice and encouragement throughout the course of my studies. His energetic personality, ultra keen sense of observation, unwavering confidence in my abilities and support during my low points have left an indelible impact on me as a person and are truly appreciated. I feel privileged to express my profound gratitude to the members of my supervisory committee, Drs. David Bressler and Phillip Choi for their suggestions and criticisms of my dissertation. I owe special thanks to Dr. Laziz Bouzidi who has been integrally involved in all aspects of my work. He spent countless hours helping and his patience is remarkable.

I gratefully acknowledge the technical help of Mr. Erredad Kharraz who trained me in the use of equipment and introduced me to experimental work on lipids. On a personal level he has been like a brother to me. I acknowledge the help and co-operation of my fellow graduate students, in particular Kerry Lyn Humphrey with whom I have shared academic discussions, read each other's work, talk about food and people and exchange blunt and honest opinions of all sorts. To Marie – Josee Dumont, thanks for the distractions and long walks.

My sincere thanks are expressed to Mr. and Mrs. Jagroop and family with whom I have lived with during most of my course of study. They have been like second parents to me, I need not say more. I appreciate the support of Mr. and Mrs. Dewnandan and family. Thanks are also expressed to my golden aunt, Mrs. Patrica Pinto for her support during my studies. Finally I would like to thank my parents and younger brother and sister. Though a continent away, they never allowed their distance to come in the way of helping and supporting me. Words cannot express my gratitude and thanks for their patience and faith in me without which I would not have been able to achieve my goals. The funding agencies of the Alberta Lipid Utilization Program namely, AARI, ACPC, ACIDF, AARP, Bunge Oils and NSERC are acknowledged.

TABLE OF CONTENTS

1. General Introduction	
1.1. Fats and oils	1
1.1.1 Triacylglycerols	3
1.2. Phase Behavior and Phase diagrams.....	6
1.2.1 Eutectics	8
1.3 Structure and Phase Behavior of Triacylglycerols.....	8
1.3.1 Polymorphism.....	10
1.4. Phase Behaviour Studies of fats: A literature review.....	15
1.4.1. Pure Triacylglycerol Studies.....	15
1.4.2. Binary Phase Behaviour Studies.....	21
1.5. Objectives.....	25
1.6. References.....	27
2. The binary phase behavior of LSL and LLS.....	33
2.1. Introduction.....	34
2.2. Materials and Methods.....	34
2.2.1. Sample Preparation.....	34
2.2.2. Thermal Processing.....	35
2.2.3. X-ray Diffraction (XRD).....	35
2.2.4. Differential Scanning Calorimetry (DSC).....	35
2.2.5. Solid Fat Content (SFC)	35
2.2.6. Relative Hardness.....	36
2.2.7. Microscopy.....	36
2.3. Results and Discussion.....	37
2.3.1. XRD Results.....	37
2.3.2. DSC Results.....	41
2.3.2.1. Crystallization Behavior.....	41
2.3.2.2. Melting Behavior.....	43
2.3.2.3. Phase Diagram of the LLS/LSL Binary System.....	44

2.3.2.4. Inter-polymorphic Transformations.....	50
2.3.2.5. Determination of Energy of Activation for Nucleation.....	52
2.3.3. Solid Fat Content (SFC).....	54
2.3.4. Relative Hardness.....	61
2.3.5. Microscopy.....	63
2.4. Conclusion.....	67
2.5. References.....	69
3. The binary phase behavior of MSM and MMS.....	71
3.1. Introduction.....	71
3.2. Materials and Methods.....	71
3.3. Results and Discussion.....	72
3.3.1 XRD Results.....	72
3.3.2. DSC Results.....	78
3.3.2.1. Crystallization Behavior.....	78
3.3.2.2. Melting Behavior.....	81
3.3.2.3. Phase Diagram of the MSM/MMS Binary System.....	83
3.3.2.4. Determination of Energy of Activation for Nucleation.....	85
3.3.3. Solid Fat Content (SFC).....	88
3.3.4. Relative Hardness.....	93
3.3.5. Microscopy.....	95
3.4. Conclusion.....	98
3.5. References.....	100
4. The binary phase behavior of PSP and PPS.....	102
4.1. Introduction.....	102
4.2. Materials and Methods.....	102
4.3. Results and Discussion.....	103
4.3.1 XRD Results.....	104
4.3.2. DSC Results.....	106
4.3.2.1. Crystallization Behavior.....	106

4.3.2.2. Melting Behavior.....	108
4.3.2.3. Phase Diagram of the PSP/PPS Binary System.....	109
4.3.2.4. Determination of Energy of Activation for Nucleation.....	113
4.3.3. Solid Fat Content (SFC).....	113
4.3.4. Relative Hardness.....	120
4.3.5. Microscopy.....	120
4.4. Conclusion.....	124
4.5. References.....	125
5. General Conclusions.....	126
5.1. References.....	139

LIST OF TABLES

Table 1-1 Summary of pure TAG phase behaviour studies.....	19
Table 2-1 Exponential constants (k, Z and X) and energy of activation for nucleation (Q _m) for LSL/LLS.....	55
Table 2-2 Avrami constant (A) and exponent (n) determined using the modified form of the Avrami equation for mixtures of LSL and LLS crystallized at 0.1 °C/min.....	59
Table 2-3. Avrami constant (A) and exponent (n) determined using the modified form of the Avrami equation for pure and binary mixtures of LSL and LLS crystallized at 3.0 °C/min.....	60
Table 3-1 Exponential constants (k, Z and X) and energy of activation for nucleation (Q _m) for MSM/MMS.....	87
Table 3-2 Avrami constant (A) and exponent (n) determined using the modified form of the Avrami equation for pure and binary mixtures of MSM and MMS crystallized at 0.1 °C/min.....	91
Table 3-3 Avrami constant (A) and exponent (n) determined using the modified form of the Avrami equation for pure and binary mixtures of MSM and MMS crystallized at 3.0 °C/min.....	92
Table 4-1 Exponential constants (k, Z and X) and energy of activation for nucleation (Q _m) for pure and binary mixtures of PSP and PPS crystallized at 0.1 °C/min.....	115
Table 4-2 Avrami constant (A) and exponent (n) determined using the modified form of the Avrami equation for pure and binary mixtures of PSP and PPS crystallized at 0.1 °C/min.....	118
Table 4-3 Avrami constant (A) and exponent (n) determined using the modified form of the Avrami equation for pure and binary mixtures of PSP and PPS crystallized at 3.0 °C/min.....	121

Table 5-1 Summary of phase behavior and ρ values for the fitted solidus and liquidus lines for the LSL/LLS, MSM/MMS and PSP/PPS binary systems.....130

Table 5-2 Summary of correlations between eutectic composition, depressions in SFC and relative hardness at 0.1 and 3.0 °C/min.....134

LIST OF FIGURES

Figure 1-1. (A) Structural arrangement of a TAG molecule. R1, R2 and R3 represent esterified fatty acids (B) Structure of linoleic acid.....	4
Figure 1-2. Generalized phase diagram demonstrating eutectic behavior.....	9
Figure 1-3. (A) Molecular interactions between TAG molecules (B) Subcell and layered structures in crystallized TAGs.....	11
Figure 1-4. Subcell structures for the α , β' and β polymorphs.....	13
Figure 1-5. Structural hierarchy of fat crystal networks.....	26
Figure 2-1. XRD spectra of LSL/LLS mixtures crystallized at 0.1°C/min.....	38
Figure 2-2. (A) Stacking mode of LSL/LLS mixtures. d_1 and d'_1 represent the parallel and perpendicular lamellar periodicities and θ is the angle of tilt (B) Variation of d_1 , d'_1 , d_2 and d'_2 long spacing vs. LSL molar fraction (C) Variation of $d_{1\beta}$ and $d_{2\beta}$ short spacing vs. LSL molar fraction. Error bars are standard deviations, n= 3.....	40
Figure 2-3. (A) Crystallization curves of LSL/LLS binary mixtures vs. LSL molar fraction at 0.1 °C/min (B) Crystallization curves of LSL/LLS binary mixtures vs. LSL molar fraction at 3.0 °C/min (C) Peak maximum of crystallization vs. of LSL molar fraction at 0.1 and 3.0 °C/min (D) Enthalpy of crystallization vs. LSL molar fraction at 0.1 and 3.0 °C/min. Error bars are standard deviations, n= 3.....	42
Figure 2-4. (A) Melting curves of LSL/LLS binary mixtures vs. LSL molar fraction at 0.1 °C/min (B) Melting curves of LSL/LLS binary mixtures vs. LSL molar fraction at 3.0 °C/min (C) Enthalpy of melting vs. LSL molar fraction at 0.1 and 3.0 °C/min. Error bars are standard deviations, n= 3.....	45

Figure 2-5. Phase diagram of the LSL/LLS binary system constructed using DSC data obtained for the samples crystallized at 0.1 °C/min (A) Fit of the liquidus line considering an ideal solution, using equations 1 and 2 (solid line) and considering non-ideality of mixing, using equations 4 and 5 (dashed line). (B) Simultaneous fit of the liquidus and solidus lines (solid lines) considering nonideality of mixing, using equations 6 and 7. Error bars are standard deviations, n= 3.....49

Figure 2-6. Phase diagram of the LSL/LLS binary system constructed using DSC data obtained for the samples crystallized at 3.0 °C/min. Experimental (symbols) and calculated liquidus line considering an ideal solution, using equations 1 and 2 (solid line) and considering non-ideality of mixing, using equations 4 and 5 (dashed line). Error bars are standard deviations, n= 3.....51

Figure 2-7. (A) Normalized nucleation rate $\frac{J}{J_{max}}$ vs. the supercooling exposure time (β) fitted to an exponential (solid line). (B) Normalized nucleation rate $\frac{J}{J_{max}}$ vs. the inverse square root of cooling rate fitted to an exponential (solid line). (C) Activation energy of nucleation vs. LSL molar composition. The solid line is a linear fit. Error bars are standard deviations, n= 3.....56

Figure 2-8. (A) SFC (%) vs. time plots for pure and binary mixtures of LSL and LLS crystallized at 0.1 °C/min (B) SFC (%) vs. time plots for pure and binary mixtures of LSL and LLS crystallized at 3.0 °C/min (C) Final (%) SFC vs. LSL molar composition at 0.1 and 3.0 °C/min.....58

Figure 2-9. Relative hardness vs. LSL molar composition for LSL/LLS binary mixtures crystallized at 0.1 and 3.0 °C/min. Error bars are standard deviations, n= 10.....62

Figure 2-10. Microstructure of pure and binary mixtures of LSL and LLS crystallized at 3.0 °C/min. Magnification = 100 x. Bar =1 μ m.....64

Figure 2-11. Microstructure of pure and binary mixtures of LSL and LLS crystallized at 0.1 °C/min. Magnification = 100 x. Bar =1 μm.....	65
Figure 3-1. XRD spectra of MSM/MMS mixtures crystallized at 0.1°C/min.....	73
Figure 3-2. (A) Stacking mode of MSM/MMS mixtures. d_1 and d'_1 represent the parallel and perpendicular lamellar periodicities and θ is the angle of tilt (B) Variation of d_1 , d'_1 , d_2 and d'_2 long spacing vs. MSM molar fraction (C) Variation of $d_{1\beta}$ and $d_{2\beta}$ short spacing vs. MSM molar fraction. Error bars are standard deviations, n= 3.....	74
Figure 3-3. XRD spectra of MSM/MMS mixtures crystallized at 3.0 °C/min.....	76
Figure 3-4. (A) Variation of long spacing as a function of MSM molar fraction (B) Stacking mode of MSM/MMS mixtures. Error bars are standard deviations, n= 3.....	77
Figure 3-5. (A) Crystallization curves of MSM/MMS binary mixtures vs. MSM molar fraction at 0.1 °C/min (B) Crystallization curves of MSM/MMS binary mixtures vs. MSM molar fraction at 3.0 °C/min (C) Peak maximum of crystallization vs. of MSM molar fraction at 0.1 and 3.0 °C/min (D) Enthalpy of crystallization vs. MSM molar fraction at 0.1 and 3.0 °C/min. Error bars are standard deviations, n= 3.....	79
Figure 3-6. (A) Melting curves of MSM/MMS binary mixtures vs. MSM molar fraction at 0.1 °C/min (B) Melting curves of MSM/MMS binary mixtures vs. MSM molar fraction at 3.0 °C/min (C) Enthalpy of melting vs. of MSM molar fraction at 0.1 and 3.0 °C/min (D) Enthalpy of melting vs. MSM molar fraction at 0.1 and 3.0 °C/min. Error bars are standard deviations, n= 3.....	82
Figure 3-7. Phase diagram of the MSM/MMS binary system constructed using DSC data obtained for the samples crystallized at 0.1 °C/min. Calculated liquidus and solidus lines (solid lines) were obtained considering nonideality of mixing by simultaneous fit of the data to equations 6 and 7. Error bars are standard deviations, n= 3.....	84

Figure 3-8. (A) Normalized nucleation rate $\frac{J}{J_{max}}$ vs. the supercooling exposure time (β) fitted to an exponential (solid line). (B) Normalized nucleation rate $\frac{J}{J_{max}}$ vs. the inverse square root of cooling rate fitted to an exponential (solid line) (C) Activation energy of nucleation vs. MSM molar composition... Error bars are standard deviations, n=3.....86

Figure 3-9. (A) SFC (%) vs. time plots for pure and binary mixtures of MSM and MMS at 0.1 °C/min (B) SFC (%) vs. time plots for pure and binary mixtures of MSM and MMS at 3.0 °C/min (C) Final (%) SFC vs. MSM molar fraction at 0.1 and 3.0 °C/min. Error bars are standard deviations, n= 3.89

Figure 3-10. Relative hardness vs. MSM molar fraction for MSM/MMS binary mixtures crystallized at 0.1 and 3.0 °C/min. Error bars are standard deviations, n= 10.94

Figure 3-11. Microstructure of pure and binary mixtures of MSM and MMS crystallized at 3.0 °C/min. Magnification = 100 x. Bar =1 μ m.....96

Figure 3-12. Microstructure of pure and binary mixtures of MSM and MMS crystallized at 3.0 °C/min. Magnification = 100 x. Bar =1 μ m.....97

Figure 4-1 XRD spectra of PSP/PPS mixtures crystallized at 0.1°C/min.....104

Figure 4-2. (A) Possible stacking modes in PSP/PPS mixtures (B) Variation of d_1 and d_2 long spacing vs. PSP molar fraction. Error bars are standard deviations, n=3.....105

Figure 4-3. (A) Crystallization curves of PSP/PPS binary mixtures vs. PSP molar fraction at 0.1 °C/min. Insert highlights the crystallization curves of the 0.4, 0.6 and 0.8 PSP samples (B) Crystallization curves of PSP/PPS binary mixtures vs. PSP molar fraction at 3.0 °C/min (C) Enthalpy of crystallization of the resolved crystallization peaks P_1 and P_2 vs. PSP molar fraction at 0.1 °C/min (D) Peak maximum of crystallization vs. PSP molar fraction at 0.1 and 3.0 °C/min (E) Total enthalpy of crystallization vs. PSP molar fraction at 0.1 and 3.0 °C/min.....107

Figure 4-4. (A) Melting curves of PSP/PPS binary mixtures crystallized at 0.1 °C/min vs. PSP molar fraction (B) Melting curves of PSP/PPS binary mixtures crystallized at 3.0 °C/min vs. PSP molar fraction (C) Enthalpy of melting vs. PSP molar fraction at 0.1 and 3.0 °C/min (D) Enthalpy of melting vs. PSP molar fraction at 0.1 and 3.0°C/min.....110

Figure 4-5. Phase diagram of the PSP/PPS binary system constructed using DSC data obtained for the samples crystallized at 0.1 °C/min. Calculated liquidus and solidus lines (solid lines) were obtained considering nonideality of mixing by simultaneous fit of the data to equations 6 and 7. Error bars are standard deviations, n= 3.....112

Figure 4-6. Variation of activation energy of nucleation vs. PSP molar composition Error bars are standard deviations, n= 3.....114

Figure 4-7. (A) SFC (%) vs. time plots for pure and binary mixtures of PSP and PPS at 0.1 °C/min (B) Induction time (s) vs. PSP molar composition at 0.1 and 3.0 °C/min (C) SFC (%) vs. time plots for pure and binary mixtures of PSP and PPS at 3.0 °C/min (D) Final (%)SFC vs. PSP molar composition at 0.1 and 3.0 °C/min Error bars are standard deviations, n= 3.....117

Figure 4-8. Relative hardness vs. PSP molar composition at 0.1 and 3.0 °C/min. Error bars are standard deviations, n=3.....121

Figure 4-9. Microstructure of pure and binary mixtures of PSP and PPS crystallized at 3.0 °C/min. Magnification = 100 x. Bar =1 µm.....122

Figure 4-10. Microstructure of pure and binary mixtures of PSP and PPS crystallized at 0.1 °C/min. Magnification = 100 x. Bar =1 µm.....123

Figure 5-1. Melting curves (5.0 °C/min) of pure TAGs crystallized at 0.1 and 3.0 °C/min (A) Melting curves of LSL, MSM and PSP at 3.0 °C/min (B) Melting curves of LLS, MMS and PPS at 3.0 °C/min (C) Melting curves of LSL, MSM and PSP at 0.1 °C/min (D) Melting curves of LLS, MMS and PPS at 0.1 °C/min.....127

Figure 5-2. Final (%) SFC vs. (LSL, MSM, PSP) molar composition (A) Final (%) SFC vs. (LSL, MSM, PSP) molar composition at 0.1 °C/min (B) Final (%) SFC vs. (LSL, MSM, PSP) molar composition at 3.0 °C/min.....131

Figure 5-3. Relative hardness vs. (LSL, MSM, PSP) molar composition (A) Relative hardness vs. (LSL, MSM, PSP) molar composition at 0.1 °C/min (B) Relative hardness vs. (LSL, MSM, PSP) molar composition at 3.0 °C/min.....133

Figure 5-4.(A) Microstructure of LSL and LLS crystallized at 0.1 and 3.0 °C/min. Magnification = 100x. Bar = 1 μm.....135

Figure 5-4.(B) Microstructure of MSM and MMS crystallized at 0.1 and 3.0 °C/min. Magnification = 100x. Bar = 1 μm.....136

Figure 5-4.(C) Microstructure of PSP and PPS crystallized at 0.1 and 3.0 °C/min. Magnification = 100x. Bar = 1 μm.....137

LIST OF ABBREVIATIONS

DSC	Differential Scanning Calorimetry
FT-IR	Fourier Transformed Infra Red Spectroscopy
NMR	Nuclear Magnetic Resonance
PLM	Polarized Light Microscope
XRD	X-ray Diffraction
SFC	Solid Fat Content
FWHM	Full Width at Half Maximum

Triacylglycerol (TAG) Names

LLS	1, 2-dilauroyl-3-stearoyl <i>-sn-</i> glycerol
LSL	1, 3 dilauroyl-2-stearoyl <i>-sn-</i> glycerol
MMS	1, 2-dimyristoyl-3-stearoyl <i>-sn-</i> glycerol
MSM	1, 3 dimyristoyl-2-stearoyl <i>-sn-</i> glycerol
PPS	1, 2-dipalmitoyl-3-stearoyl <i>-sn-</i> glycerol
PSP	1, 3 dipalmitoyl-2-stearoyl <i>-sn-</i> glycerol

Other TAGs will be mentioned in this thesis such as SSS, SOS, POS, LLL, LLL, MMM, EPE, EEP. In these instances L=lauric acid, M=myristic acid, O=oleic acid, P=palmitic acid, S=stearic acid.

Symbols

α	alpha polymorph
β	beta polymorph
β'	beta prime polymorph
ρ	adjustable parameter for non – ideality
Q_m	energy of activation for nucleation

Acronyms

A.A.R.I.	Alberta Agricultural Research Institute
A.C.P.C.	Alberta Canola Producers Association
A.C.I.D.F.	Alberta Crop Industry Development Fund
A.A.F.R.D.	Alberta Agriculture Food and Rural Development

1. General Introduction

1.1. Fats and Oils

Fats and oils originating from plants and animals are mainly constituted of a series of molecules referred to as triacylglycerols (TAGs). Additionally, fats and oils may include other minor components such as monoglycerides (MAG), diglycerides (DAG), sterols, phospholipids, tocopherols, resins, proteins, pesticide residue and pigments such as gossypol, carotene and chlorophyll (O' Brien, 2004). The terms fats and oils are used interchangeably depending upon the phase of the material being solid or liquid, respectively.

Fats and oils play an essential role in human nutrition; they provide a number of essential physiological functions such as, the provision of calories, a source of essential fatty acids, and as vitamin carriers (Padley and Podmore, 1985). From a food processing perspective, fats and oils provide characteristics such as texture and functionality, while adding to the palatability of foods (Bruin, 1999). Understanding the physical nature of these characteristics can aid in the processing of fats and oils into new and or improved food products; this is of great importance to the food processing industry. Towards this endeavor, this thesis focuses on providing a greater understanding of the physical properties, particularly the phase behaviour, of fats by examining detailed studies of fat systems composed of binary mixtures of TAG molecules.

Relating the phase behaviour of pure TAGs species to the physical properties of complex natural fat systems is a significant endeavor, to which our research group, the Alberta Lipid Utilization Program is committed. This thesis investigates a small subset of this large endeavor, i.e. the phase behaviour of symmetric and asymmetric positional isomers of saturated TAGs.

Natural fats and oils of plant and animal origin have limited functionality due to their fatty acid content which is distributed in an organism - specific manner within their constituent TAGs (Sreenivasan, 1978). In order to extend functionality, two main modification processes are utilized in industry namely; hydrogenation and interesterification.

Hydrogenation involves exposure of oil to hydrogen in the presence of a metal catalyst. The resulting changes include; saturation of double bonds (primary change), isomerization of *cis* double bonds to *trans* double bonds and shifting of double bonds along the carbon chain. The main functionalities which are enhanced by partial hydrogenation are shelf life, hardness and melting behaviour. Given recent health concerns regarding trans fatty acids, food manufacturers are forced to reduce trans fatty acid content but maintain functionality.

Interesterification has emerged as one of the solutions to producing trans free products. Interesterification involves the reshuffling of fatty acids along the glycerol backbone of TAG molecules. In this process fatty acid profile, geometric isomerism and degree of saturation all remain unchanged. Most importantly, no trans fatty acids are introduced. By reshuffling fatty acids on TAGs from a fully hydrogenated or saturated fat and from liquid oil, interesterification mimics the effect of partial hydrogenation and as such delivers comparable functionality in some instances. Indeed, the patent literature contains many references for the preparation of margarine and shortenings by interesterification of a wide variety of naturally occurring and trans free fully hydrogenated fats (List et al., 1995). Interesterification may be carried out enzymatically or chemically. Enzymatic interesterification offers some control of the randomization process as the lipases used are usually specific to the *sn*-1 and *sn*-3 positions on the glycerol backbone, leaving the *sn*-2 position unchanged (Soumanou et al., 1998). Chemical interesterification may be directed or random. The implication of random chemical interesterification is of particular interest as the process introduces positional isomers.

Theoretically the random chemical interesterification of equimolar amounts of two TAGs, AAA and BBB, should yield the following percentages at equilibrium AAA (12.5%), BBB (12.5%), AAB (25%), BBA (25%), ABA (12.5%) and BAB (12.5%). The mixed species would consist of 66% symmetrical TAGs and 33% asymmetrical TAGs (Rozenaal, 1992).

In some interesterification studies (Nor Aini et al., 2002; Rodrigues and Gioioelli, 2003), eutectic interactions were observed and they were often accompanied by depressions in solid fat content. This change in phase behaviour was attributed to the

composition of classes of symmetric (SUS, USU) and asymmetric (SSU, UUS) TAG species, where S = saturated fatty acid and U = unsaturated fatty acid. The relative proportions of these classes of TAGs are altered by interesterification. This study is unique as we investigate the phase behaviour of positional TAGs isomers within the class of saturated (SSS) TAGs. Such phase behaviour studies have not been performed before. In applications where solid fat content is important, eutectic formation would pose a problem for low *trans* fats produced using interesterification. Generally, the SFC of a fat or oil is responsible for properties such as appearance, ease of packaging, spreadability, oil exudation and organoleptic properties.

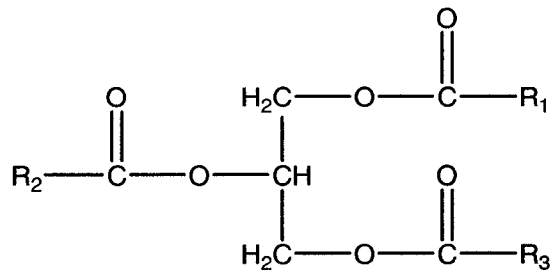
It is our hypothesis that the interaction between symmetric and asymmetric positional isomers can lead to disruptive packing in the solid state and as such result in eutectic formation. Furthermore, we hypothesize that the degree of mismatch in fatty acid chain length can further influence crystalline packing and phase behaviour. As such a series of three binary systems were studied, namely LSL/LLS, MSM/MMS and PSP/PPS, which have a chain length mismatch of 6, 4 and 2 carbon – carbon bond lengths respectively. Our detailed hypotheses are listed at the end of this chapter.

1.1.1. Triacylglycerols

A TAG molecule (Figure 1-1 (A)) is made up of a glycerol backbone (trihydroxy propane) esterified to three fatty acid moieties. An example of a fatty acid (linoleic acid) is shown in Figure 1-1 (B). The backbone carbons of the glycerol are identified as *sn*-1, *sn*-2 or *sn*-3 based on the “stereospecific numbering system”, *sn* which is a recommended IUPAC nomenclature (IUPAC, 1978).

The physical and chemical properties of a particular TAG molecule depend on the fatty acid constituents and their position on the glycerol backbone. The numerous possible combinations of fatty acids on the glycerol backbone lead to a wide TAG diversity in natural systems (Sreenivasan, 1978). TAGs possessing three identical acyl chains are referred to as monoacid TAGs and those with more than one type of acyl chains are called mixed acid TAGs. Fats are usually classified as saturated, monounsaturated, polyunsaturated or and super-unsaturated based on the fatty acids dominating the composition of the TAGs present in the fat.

(A)



(B)

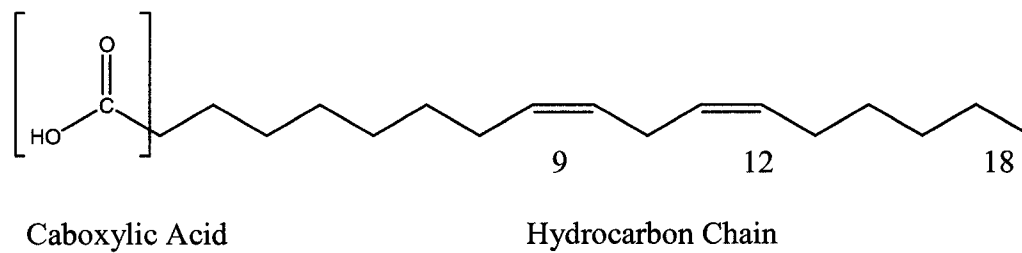


Figure 1-1. (A) Structural arrangement of a TAG molecule, R₁, R₂ and R₃ represent esterified fatty acids (B) Structure of linoleic acid

The structures of the fatty acid substituents in TAGs vary based on chain length, isomeric form and number and position of double bonds if they are present. The isomerization of the double bond (*i.e.* *cis* vs. *trans*) has been of recent interest due to reports that the *trans* configuration of the fatty acid double bond has adverse health implications associated with their consumption (Mensink and Katan, 1993).

Saturated fatty acids contain carbon – carbon single bonds and possess a consistent “zig – zag” or what is loosely referred to as a “straight chain” structure which is conducive to crystalline packing. It is therefore not surprising that highly saturated TAGs usually exist as solids at room temperature.

Monounsaturated fatty acids contain a single carbon-carbon double bond. The introduction of this bond which may be *cis* or *trans* affects close molecular packing thereby reducing the melting point of monounsaturated TAGs relative to saturated TAGs. The effect of the *cis* configuration on melting point is more drastic as the two hydrogens are on the same side of the carbon-carbon double bond resulting in a “bent or kinked” shape. However, in the *trans* configuration, the hydrogens are located diagonally and the chain maintains a relatively “straight” conformation, similar to that of saturated fatty acids. It is, therefore, not surprising that *trans* fatty acids have higher melting points than *cis* fatty acids because of the latter’s reduced ability to pack more closely. For example, oleic acid (18:1 Δ^{9cis}) melts at 13.2 °C and elaidic acid (18:1 Δ^{9trans}) at 43.7 °C. The *trans* isomer melts almost 30°C higher than the *cis* isomer.

Polyunsaturated fatty acids (PUFA’s) contain two or more carbon-carbon double bonds which are interrupted by a methylene group. The presence of more than one double bond introduces multiple kinks in the acyl chain inhibiting packing into a crystalline structure; hence the resulting TAGs are usually liquids at room temperature.

Four naming systems are commonly used to name fatty acids, all of which attempt to denote chain length, number of double bonds and their positions. These systems are; the trivial name, the IUPAC nomenclature, the carboxyl (Δ or *n*) reference and the methyl (ω) references. The carboxyl reference gives the location of the double bonds relative to the carboxyl group while the methyl reference gives the position relative to the methyl end of the molecule. Biologists usually prefer the methyl reference due to the physiological difference between the ω -3 and ω -6 fatty acids. For example, using the

four systems the fatty acid in Figure 1-1 (B) is named, linoleic acid (trivial name), 9, 12-octadecanoic acid (IUPAC), $18:2\Delta^{9,12}$ (carboxyl) and 18:2 (ω -6).

1.2. Phase Behaviour and Phase Diagrams

A phase is defined as a homogenous macroscopic domain with uniform chemical composition and physical properties (Atkins, 1998; Moore, 1983). Phase behaviour refers to the relationship and occurrence of a phase change. Fats, or an ensemble of TAG molecules, can be thought of as a system of coexisting homogenous domains which are not necessarily in equilibrium (Humphrey and Narine, 2004b).

Understanding phase behaviour of lipids is very important to the food industry as most foods contain natural or structured multiphase dispersions of lipids (Bruin, 1999). By better understanding phase behaviour of lipids, their beneficial role in foods can be maximized. Phase diagrams and iso-solid lines are powerful tools which provide a wealth of information on fat blends that is particularly useful for the industrial processing of fats (Timms, 2003).

A phase diagram is a graphical representation of a set of conditions (temperature, pressure and concentration) corresponding to an equilibrium between phases in a system of one or more components. A component is a chemical species, and a phase may consist of a number of components, provided that the components are homogeneously dispersed. In lipid systems, the vapor pressures are very low and, as a result, changes in pressure (particularly at or near atmospheric pressure) have negligible effects on the system. Such systems, termed condensed systems, are usually described by their temperature and composition variables. Phase diagrams are plotted two dimensionally for binary systems and three dimensionally for ternary systems which requires one or two axes for composition, respectively, and a separate axis for temperature (Bailey, 1951).

Phase diagrams are governed by the Gibbs phase rule which states that the number of intensive variables that can be changed independently without altering the number of phases (degrees of freedom f) is given by:

$$f = c + 2 - p$$

where c is the number of components and p the number of phases.

If the degree of freedom is 1, it means that only one intensive variable may be arbitrarily specified. If one temperature is chosen, this temperature automatically determines the composition of the two phases. If one composition is fixed then there can be only one value for the composition of the other phase and one for temperature (Bailey, 1951). Throughout this thesis only binary systems were investigated, so the remainder of the discussions will concern binary phase behaviour.

The phase behaviour displayed by a binary system of TAGs depends on their intersolubility behaviour (Knoster and DeBruijne, 1972). Ideal solubility behaviour of a binary lipid mixture occurs without any heat or volume changes and can be predicted by the Hildebrand equation (Hildebrand, 1929; Knoster and DeBruijne, 1972).

$$\ln x = \frac{\Delta H_{\text{fus}}}{R} \left(\frac{1}{T} - \frac{1}{T_0} \right)$$

where, x = solubility of high melting component (mol / mol), ΔH_{fus} = heat of fusion of high melting component (KJ/mol), T = melting temperature of high melting component, T_0 = experimental temperature (K) and R = universal gas constant (8.314472 J / mol. K). Deviations from ideality can occur at high solute to solvent ratios as the change in volume increases the entropy of mixing during melting (Knoster and DeBruijne, 1972). In solid solutions the differences in solubility between perfect and imperfect crystals also contribute to deviations (Humphrey and Narine, 2004b).

Timms (Timms, 1984) grouped the binary phase behaviour of TAGs into four categories: monotectic continuous solid solution, monotectic partial solid solution, eutectic, and peritectic (Minato et al., 1997). Minato and coworkers (Minato et al., 1997), listed the occurrence of three phases (the solid phase, eutectic phase and compound formation) in which the two components are completely miscible at all concentrations in the liquid phase. Of the three binary systems investigated in this thesis two demonstrated eutectic phase behaviour. Therefore, eutectic phase behaviour will be discussed. The interested reader is referred to Humphrey and Narine (Humphrey and Narine, 2004b) for a complete and exhaustive discussion of binary phase behaviour.

1.2.1. Eutectics

Eutectic systems tend to occur when molecular volumes, shapes or polymorphs of pure components differ (Timms, 1984). A eutectic indicates a melting or boiling point for a particular composition which is lower than either of the pure components. A general phase diagram for a binary mixture demonstrating eutectic phase behaviour is shown in Figure 1-2; the eutectic point labeled as E occurs where the depressed liquidus line meets the solidus line. At this point three phases exist simultaneously, solid A, solid B and the melt (liquid). However, the eutectic point in some systems may be indicated only by a depression in the liquidus line which does not necessarily meet the solidus line. The nature of the pure components and the thermal processing history usually determines the temperature and composition at which the eutectic point or eutectic minima occurs. An example of such a binary system is tri-palmitoyl-*sn*-glycerol (PPP) and tri-stearoyl-*sn*-glycerol (SSS) (Timms, 1984). Eutectics may be formed because of steric hindrances or other interactions which are disruptive to the crystalline packing (Sato, 2001). This is of significant importance to industry as there is usually a higher liquid content than solid at the eutectic point. Such a property can be disadvantageous in the case of margarines or shortenings where solid fat content is important. Conversely, this eutectic phase behaviour is advantageous in instances where crystallization of the liquid phase is to be avoided, such as in salad dressings (Humphrey et al., 2003).

1.3. Structure and Phase Behaviour of Triacylglycerols

A full understanding of phase behaviour cannot be achieved without knowledge of the molecular structure and orientation of the various components, particularly in the solid state. A discussion of the solid structures of TAGs cannot be carried out without a discussion of polymorphism, as there can often be more than one polymorphic form of each TAG present in the mixture.

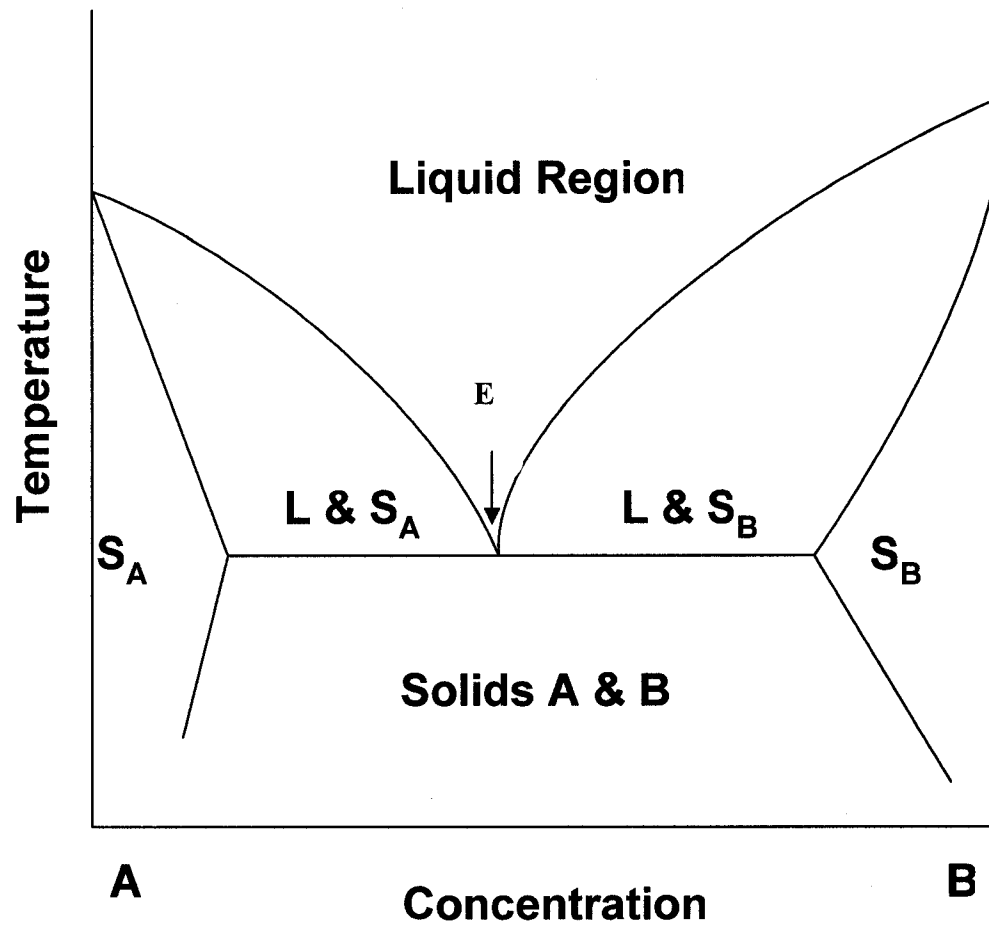


Figure 1-2. Generalized phase diagram demonstrating eutectic behaviour. L = liquid, S_A = solid A, S_B = solid B and E = eutectic point.

1.3.1. Polymorphism

Polymorphism is defined as the existence of two or more distinct crystalline forms of the same substance. The different polymorphic states of a particular substance often demonstrate quite different physical properties, such as melting behaviour and hardness. Crystallization conditions influence the rate of crystallization, crystal size, crystal morphology and polymorphism ultimately the final fat crystal network. Furthermore, polymorphic transformations are influenced by internal factors (*i.e.* molecular structure) and external factors (temperature, shear rate experienced during crystallization, solvent, pressure, impurities, etc.) (Sato, 2001).

Given the wide diversity of TAG species present in natural fat systems, it is difficult to understand the effect of TAG structure on the crystallization process. Hence it is fundamentally important to study the phase behaviour and polymorphism of pure TAG systems in isolation as a function of different cooling rates.

In this section, the intermolecular interactions between TAGs, their packing into a crystal lattice, the nature of polymorphic transformations and finally how chain length, chain length mismatch and molecular symmetry influence polymorphism will be examined. The molecular interactions between TAGs are characterized by five main elements as shown in Figure 1-3 (A) (Sato et al., 1999; Timms, 1984):

- aliphatic (hydrocarbon) chain packing - caused by hydrocarbon chain – chain interaction as revealed in sub-cell structures
- olefinic interaction or double-bond configuration - influences packing in mixed acid TAGs
- methyl end group stacking - plays an important role in organizing different chain length structures
- glycerol group interaction - acts through dipole-dipole interaction of the glycerol groups

The main structural factors used to characterize polymorphs are the sub cell and layered structures (see Figure 1-3 (B)). The sub cell structure refers to the cross sectional packing between zig zag fatty acid chains while the layered structure arises out of the repetitive sequence of acyl chains which form a unit lamella along the hydrocarbon axis.

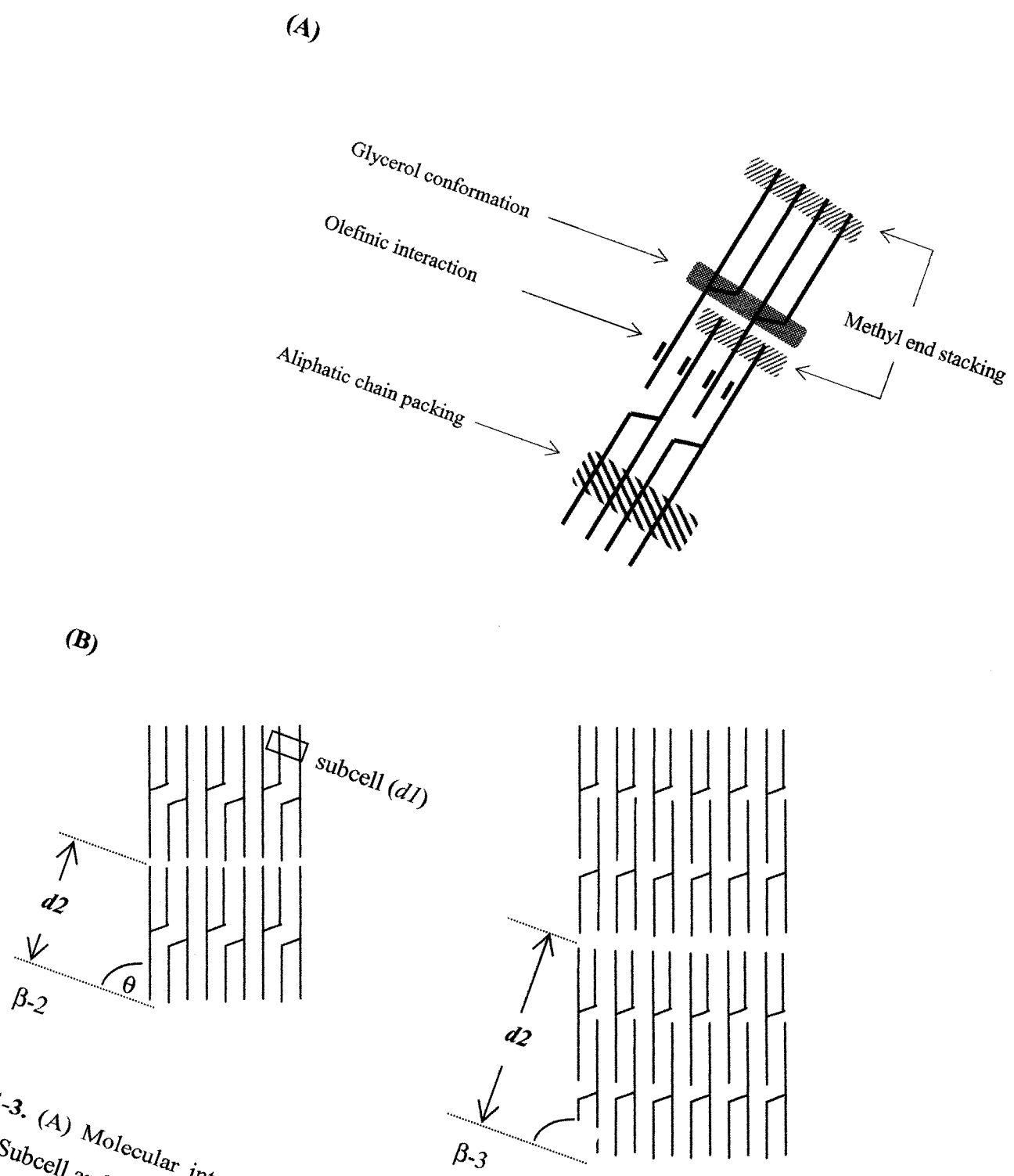


Figure 1-3. (A) Molecular interactions between TAG molecules adapted from (Sato, 1999) (B) Subcell and layered structures in crystallized TAGs

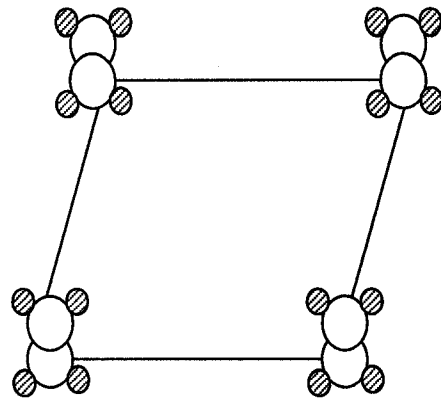
Two types of Bragg spacings are recognized when fat crystals are analyzed for polymorphism using X-ray diffractometry. Long spacings (d_2) are observed in the 2θ range of $1-15^\circ$ and short spacings (d_1) in the range of $16-25^\circ$ (Gibon et al., 1986) as shown in Figure 1-3 (B). The long spacings or layered thickness (d_2) correspond to the planes formed by the methyl end groups of the TAGs and show dependence on chain length and the angle of tilt (θ) (Figure 1-3 (B)). Short spacings (d_1) are however independent of chain length; they represent a cross sectional packing which is limited by the glycerol backbone.

Based on these short spacings resulting from the sub cell structure, three main polymorphs are identified (Figure 1-4). These are referred to as the alpha (α), beta prime (β') and beta (β) polymorphs.

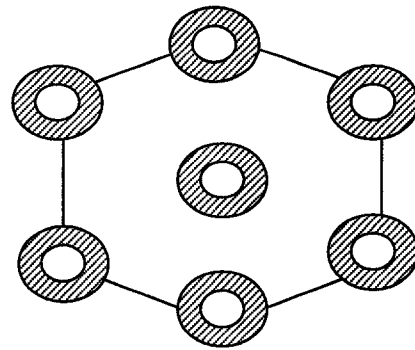
The (α) form refers to a hexagonal sub cell and demonstrates a Bragg spacing of 4.2 \AA , the (β') form refers to an orthorhombic perpendicular sub cell with two Bragg's spacings between $4.2 - 4.3 \text{ \AA}$ and $3.7 - 4.0 \text{ \AA}$, and the beta (β) form refers to a triclinic parallel sub cell with a Bragg's short spacing of 4.6 \AA eg. (Ghotra et al., 2002; Timms, 2003).

The long Bragg's spacings indicate whether the TAGs stack in a double chain length (DCL), triple chain length (TCL) structure or even a hexa (Fahey et al., 1985) or quatro (Kodali et al., 1990) chain length structure. To complete the nomenclature of naming polymorphs, layer thickness (d) is indicated by adding a number after the polymorph symbol. Numbered subscripts may also be used to distinguish between polymorphs having the same sub cell and layer thickness spacings. For example, the pure TAG SOS has three β -3 polymorphs and they are represented as β_1 -3, β_2 -3 and β_3 -3.

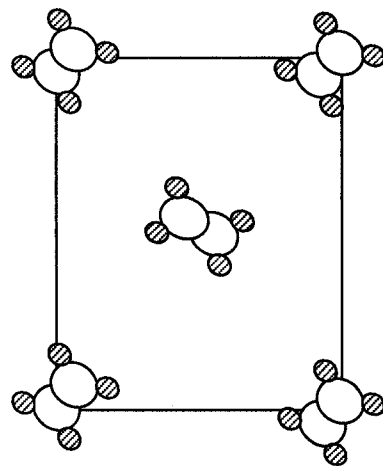
Ideally, polymorphic transformations follow Ostwald's rule, i.e. the formation of crystals with the highest free energy first and therefore the polymorphs (α , β' and β) listed in order of increasing thermodynamic stability or decreasing free energy, should follow the ($\alpha \rightarrow \beta' \rightarrow \beta$) transformation sequence. However when kinetic factors such as supercooling or supersaturation are reduced, external influences (e.g. pressure, temperature, seeding etc.) may cause the law to be broken and enable the start of nucleation of more stable forms (Sato, 2001).



β - triclinic



α - hexagonal



β' - orthorhombic

Figure 1-4. Subcell structures for the α , β' and β polymorphs (Ghotra et al., 2002)

It has been shown that fats with simple and symmetric fatty acid composition tend to exhibit all three α , β' and β polymorphs whereas, those with asymmetric mixed acid TAGs tend to pack in the β' polymorph (Hagemann, 1988). The β' polymorph is also thought to be better able to accommodate structural difference between fatty acids in a TAG molecule (Sato, 2001; Timms, 2003; van Langevelde et al., 1999b). Closer and more homogenous packing of the glycerol groups in symmetric TAGs has been attributed increased β' stability (Elisabettini et al., 1998). Furthermore it has been suggested that asymmetry puts a “break” on the crystallization process (Rousset et al., 1998) and as shown in a previous study by Rousset et al. of the individual TAGs POP, POS and SOS, the asymmetric POS had the lowest growth rate (Rousset et al., 1997). In addition to changes in the sub cell packing, TAG structure also affects the layered packing. Most often a double chain length structure is formed when the three fatty acid moieties are the same or similar while the triple chain length structure occurs when there is significant difference in chain length or degree of saturation. The triple chain length structure is better able to accommodate molecular differences as it allows greater flexibility for the odd fatty acid chain to be sorted in a different plane. The blending of fats containing different chain length structures can possibly lead to segregation during solidification or during extended storage after solidification (Sato et al., 1999).

The polymorphic form of a fat is very important to functionality. For example, the metastable β' polymorph is most functional in margarine because of its small needle like morphology which contributes to desirable rheological and textural properties. In chocolate the form V, β polymorph is desirable for optimal density, melting behaviour and uniform surface appearance. Food technologists therefore seek to achieve controlled polymorphic form and stability.

Chain length mismatch manifests its effect primarily by altering the methyl end terrace. Hypothetically, greater chain length mismatch should result in more unevenness at the terrace leaving “gaps” or “holes between stacked layers. As the system seeks optimum packing these gaps can be minimized by sorting the odd chain and packing in a triple layer structure which will allow greater chain - chain overlap and hence interaction. The effect of molecular symmetry must also be considered, since PPP which has 0 chain length mismatch also has an uneven methyl terrace due to the glycerol backbone.

It has been shown that a 4-6 °C higher melting point is observed for symmetric TAGs; this finding was attributed to entropy and crystal lattice stabilization (De Jong and Van Soest, 1978). In a more recent study, the effect of symmetry and chain length mismatch on the β' -3 polymorph for pure TAGs (van Soest et al., 1990) was investigated. Packing mode, methyl terracing, and melting points were modeled and compared with experimental values. Chain length mismatches of 2-4 carbons atoms were found to have a common and favorable methyl end arrangements while those with 6 and 0 (symmetrical) demonstrated a less favorable arrangement.

1.4. Phase Behaviour Studies of Fats: A Literature Review

The majority of lipid phase behaviour studies involve pure TAG systems and the effects of variable chain length, position and geometric isomerism of the double bond.

Not surprisingly the main TAGs contained in cocoa butter have been extensively studied. Cocoa butter is of immense economic importance and control of the $\beta' \rightarrow \beta$ transformation is especially important to the chocolate industry, since unwanted transitions may cause fat bloom, a white appearance on the surface of chocolate.

One of the earliest reviews on the phase behaviour of pure TAG systems was compiled by Rossel (Rossel, 1967). He classified the investigated systems into four categories: simple mono acid TAGs, mixed TAGs, ternary mixture of TAGs and systems with partial glycerides. In this review the phase behaviour of pure TAGs will be discussed followed by binary mixtures.

1.4.1. Pure Triglyceride Studies

The polymorphism of 13 single acid TAGs containing acyl chains between 16 to 22 carbons in length (n) and varying degrees of unsaturation was investigated using DSC (Hagemann et al., 1972). Usually the single β' form is attributed to these TAGs, however two intermediate polymorphs were identified between the least stable α and most stable β forms for most samples. Another study involving 25 single acid TAGs with structure OOO (O=isomers of oleic acid) with double bonds ranging from $\Delta 4$ - $\Delta 17$ using DSC was also performed (Hagemann et al., 1975).

The TAGs with *cis* bonds in odd positions ($\Delta 7$ - $\Delta 13$) exhibited three intermediate β' polymorphs while those with *cis* bonds in even positions, lacked β' polymorphs, with the exception of *cis* $\Delta 4$. Among the *trans* compounds, only the $\Delta 11$, $\Delta 13$ and $\Delta 14$ showed the β' polymorphs. *Cis* and *trans* $\Delta 5$ were unusual as they readily assumed a low melting α polymorph and did not transform easily to a higher melting β polymorph. Even double bond positions were associated with higher melting points and heats of fusion both of which varied non-uniformly with double bond position. Later (Hageman and Rothfus, 1983), extended the previous study (Hagemann et al., 1972) of saturated monoacid TAGs by including odd chain fatty acids ranging from 8 to 30 carbons in length and correlated the results with theoretical modeling. Shorter odd chain length TAGs ($n=9$ to 13) exhibited only one β' form and even chain length TAGs ($n=8$ to 14) exhibited three. Odd chain length $n=21$ and $n=23$ TAGs showed two β -forms. TAGs of even chain lengths greater than $n = 21$ produced two α forms. An alteration of melting point with double bond position was also observed, analogous to the alteration with chain length.

In the first systematic study investigating polymorphism in relation to changes in chain length of the *sn*-2 position of TAGs; two series were studied namely S(n)S and P(n)P (Grey and Lovengren, 1978; Lovengren and Gray, 1978). The *sn*-2 carbon chain length (n) was varied from 2- 18 including even numbers only in these two series of 1, 3 distearoyl TAGs. Different DSC cooling rates were used to observe the polymorphic changes and to determine the heats of fusion and crystallization. Polymorphs were identified based on their melting points with the α polymorph having the lowest melting point and the β polymorph the highest. Similar polymorphic behaviour was observed for SSS and PPP, S16S and P14P, S14S and P12P. Interestingly these pairs exhibiting similar polymorphic behaviour possess the same chain length mismatch, for example S16S and P14P both have a mismatch of 2 carbon atoms. It was found that the P(n)P system converted more rapidly to thermodynamically more stable polymorphs than the S(n)S series. The difference in inertial mass between the two systems may explain their relative propensity to transform, i.e. the palmitic system having a lower inertial mass than the stearic system. In addition when (n) = 8 for both series the least stable polymorph (lowest melting) was formed, which quickly transformed to a more stable polymorph.

In another systematic study, Kodali and co-workers (Kodali et al., 1984) utilized XRD and DSC techniques to study the polymorphic changes in the homologous series of optically active TAGs, PP(n) where the carbon number (n) of the *sn*-3 fatty acid chain was varied from 2-16 including even numbers only. In this study, the results were grouped into three categories based on molecular structure. The first group consists of PP (unsubstituted), PP2 and PP4 with long spacings ca. 43 Å and the β subcell. The second group consisted of PP6 and PP8 with long spacings 51-53 Å and a β' subcell and the third group contained the PP12, PP14 and PPP with long spacings of 40-41 Å and probably a β subcell. Clearly the three groups formed double, triple and double stacking structures respectively.

In a subsequent study by the same research group (Fahey et al., 1985), the series O(n)O was studied where the *sn*-2 position was substituted with even carbon saturated fatty acyl chains of 14-24 carbons in length and the *sn*-1 and *sn*-3 positions being occupied by oleic acid which is monounsaturated. One to four polymorphic forms were obtained in this study depending upon chain length.

The enthalpy of fusion and entropy were observed to increase in a linear manner with respect to increase in length of the *sn*-3 acyl chain. The stable polymorphic form for all compounds exhibited a triple layer structure, however, a metastable six layered structure was observed for O14O. It has been proposed that the unsaturated chains packed in a bilayer separated from the saturated chains, and complex polymorphic changes were attributed to adjustments in chain packing as well as transitions from the unstable three layered structure to the six layered structure.

Using synchrotron XRD and DSC the polymorphic transitions of tristearin (SSS) and tripalmitin (PPP) were monitored in situ (Kellens M., 1991a).

Both of these TAGs exhibited a tendency towards β crystallization. After achieving the α phase, recrystallization to the β phase occurred very rapidly. Time resolved synchrotron XRD data, however, did not reveal detectable amounts of β' crystals during the $\alpha \rightarrow \beta$ transformation. This could be attributed to either an extremely fast $\beta' \rightarrow \beta$ transformation rate or direct $\alpha \rightarrow \beta$ transformation. From the data obtained the latter was considered more plausible since β' and β crystallizations are kinetically competing processes and crystallization of β crystals from an α melt would be kinetically

avored. Summarized in Table 1-1, are binary and pure TAG which were studied and the methods of analysis used.

In another major pure TAG study, series of six mixed diacid TAGs consisting of elaidic acid in different positions with palmitic or stearic acids was studied (Elisabettini et al., 1998). The elaidic/palmitic TAGs (PEP, EPP, PEE) were β stable while the elaidic/stearic TAGs (SES, ESS, SEE) were β' stable. Both sets of TAGs formed double chain length structures. The interpenetration of palmito-elaidyl chains at the methyl end packing is thought to inhibit the transformation of β' polymorph to the more thermodynamically stable β polymorph. Substitution of palmitic chains with stearic chains does not seem to be a factor in stabilizing either the β' nor β polymorph since both POP and SOS are stable in the β form (Sato et al., 1989). More interestingly, the $\alpha \rightarrow \beta'$ transformation for the symmetric PEP takes place in the solid state, while the same transition is melt mediated for EPP and PEE. The symmetric arrangement of hydrocarbon chains around the glycerol moiety is thought to induce better stability of the β' crystalline lattice than the asymmetric one. The symmetric TAGs have a higher melting temperature as well as heat of fusion. See Table 1-1 for a summary of pure TAG studies.

In the homologous series of TAGs $C_n C_{n+2} C_n$ (van Langevelde et al., 1999a), where n represents the even number carbon atoms ranging from 10-16 carbon atoms, the metastable β' form crystallized and no β polymorphs were observed. The elucidation of the β' structure has eluded scientists because of the difficulties in growing crystals of sufficient size for x-ray crystallography studies and secondly the tendency of this metastable state to transform to the β polymorph. Two main single crystal studies have been carried out namely, 1, 2-palmitoyl-3-myristoyl-sn-glycerol (PPM) and 1, 3-didecanoyl-2-dodecanoyl-glycerol (CLC) for the β' structure (Sato, 2001; van Langevelde et al., 2001). These two structures however are different, in the case of CLC the TAG molecules are bent with respect to the lamellar plane at the glycerol group and in PPM the TAG molecules are bent at the methyl end packing. These two proposed structures give rise to the concept of diversity in β' structures.

Ninety eight (98%) of cocoa butter is made up of 5 TAGs: POP (19%), POS, POO (46%), SOS and SOO (33%) (Soumanou et al., 1998).

Author	System	Measurement Technique
<i>Polymorphic Occurrence and Transformation of Pure TAG</i>		
(Miura et al.,2004)	PPP, SSS, POP, SOS, POS, SOS/SOS mixtures	DSC, XRD
(Ueno et al., 2003)	PPS, LLL	DSC, SR XRD
(Higaki et al., 2001)	Pure and impure PPP	DSC, XRD
(Smith, 2000)	Different TAGs	PLM, DSC, XRD
(Sprunt et al., 2000)	SOS	FT-IR , DSC
(Boubekri et al., 1999)	SRS	FTIR, SR XRD
(Ueno et al., 1999)	SOS	
(Dibildox-Alvarado and Toro-Vazquez, 1998)	PPP in sesame oil	SR XRD
(Toro-Vazquez et al., 2000)	PPP in sesame oil	DSC, PLM, XRD
(Ueno et al.,1996)	SOS	DSC, PLM, XRD
(Rousset et al., 1998)	POP, POS, SOS	PLM, DSC
(Yano et al., 1993)	SOS, POP, POS	FTIR
(Kellens M., 1992)	PPP	PLM, DSC
(Arisima, 1989)	POS	DSC, XRD
(Kellens M., 1991)	PPP, SSS	SR XRD
(Kellens et al., 1990)	PPP	SR XRD
(Arisima, 1989)	POP, SOS	DSC, XRD
(Koyano, 1989)	POP, SOS	DSC, PLM, XRD
<i>Phase behaviour and polymorphic transformation of binary TAG mixtures</i>		
(Miura et al.,2004)	POS/SOS	DSC, XRD
(Takeuchi et al., 2000)	LLL/MMM, LLL/PPP, LLL/SSS	SR XRD
(Takeuchi et al., 2003)	SOS/SLS	DSC, SR XRD
(Rousset et al., 1998)	SOS/POS	DSC, SR XRD
(Minato et al., 1997)	POP/PPO	DSC, SR XRD
(Minato et al.,1997)	POP/OPO	DSC, SR XRD
(Minato et al., 1997)	PPP/POP	DSC, SR XRD
(Engstrom et al.,1992)	SOS/SSO	DSC, XRD
(Kellens et al.,1992)	PPP/SSS	DSC, XRD
(Koyano et al.,1992)	SOS/OSO	DSC, XRD
(Kellens et al.,1991)	PPP/SSS	DSC, SR XRD
(Cebula and Smith, 2000)	Binary TAGs	DSC
(Wesdorp, 1990)	PPP/SSS	SR XRD

Table 1-1. Shows selected pure TAGs and binary systems and the measurement technique used in the study. Adapted from (Himawan et al., 2006)

The TAGs POP, POS and SOS are similar and can be grouped in the category of TAGs, Saturated - Oleic- Saturated. The polymorphism of POP and SOS was investigated by Sato et al. 1989; six polymorphs were identified for POP (α , γ , pseudo- β'_2 , pseudo- β'_1 , β_2 and β_1) and five (α , γ , pseudo- β' , β_2 and β_1) for SOS. Notably, such TAGs display greater complexity in behaviour than single acid saturated TAGs. This study also highlighted the effect impurities may play in polymorphic transformations; the 99.2% pure POP crystallized in the δ form while the 99.9% pure POP sample did not crystallize in this polymorph. Koyano studied the polymorphism of individual POP and SOS and the kinetics of melt crystallization (Koyano et al., 1989). The study found that the α polymorph of POP crystallized easier in a double layer structure than the SOS α polymorph which was attributed to relative chain length differences. In POP, despite oleic and palmitic acids having different carbon numbers, the unsaturated double bond in oleic acid kinks the chain resulting in palmitic and oleic acids having relatively similar lengths. However in SOS, stearic acid being longer than palmitic acid would still remain relatively longer than oleic acid despite the kink in oleic acid.

Arishima 1989 crystallized single crystals of the β_2 and β_1 polymorphs of both POP and SOS from a solution of acetonitrile (Arishima, 1989). The long and short XRD spacings for the β_1 polymorph were found to be same as in the previous study (Sato et al., 1989). This study demonstrated that solvent mediated transformation was the single way to grow the β_1 polymorph since melt-cooling and melt mediated transformation did not crystallize the β_1 polymorph both in POP and SOS. Ueno et al. 1999, utilizing synchrotron x-ray radiation studied the crystallization of various polymorphs of SOS from the liquid phase (Ueno et al., 1999). Short and long synchrotron XRD spacings revealed that lamellar packing occurs more rapidly than subcell packing and that the time lag between these two packing modes is greater for the more stable polymorphs. The reason proposed to explain these findings was that the van-der-Waals forces are more effective along the normal to the long chain axis than along the long chain axis due to the rod-like shape of the SOS molecule. Reviews by Sato 1999, 2001 discuss in detail the phase behaviour of single acid TAGs with emphasis on intermolecular interactions and kinetic factors which influence the various transformations (Sato, 2001; Sato et al., 1999).

In 1984 Timms published a review on the phase behaviour of fats and their mixtures which stressed on two facets of phase behaviour, polymorphism and solid fat content (Timms, 1984). The review also described how to create and interpret iso-solid lines and stated useful assumptions which should be noted when interpreting phase diagrams of real fats. A table containing selected TAGs was listed along with stability rules for the various polymorphs which they form. Another table listing trisaturated and unsaturated TAGs found in confectionery fats was also published by (Timms, 2003).

These rules can be summarized as follows for pure TAGs represented as ABC, where A, B and C are the constituent fatty acids.

1. β' -2 polymorph is most stable and offers the best packing. This occurs when $A=B=C$ (i.e. for a mono-acid TAG), chain length mismatch is no greater than 2-4 carbons or when A, B C are trans fatty acids.
2. When fatty acids are different, two forms are stable:
 - a. β -3, allows chain sorting when $A=C$ and B is different. The odd chain B is sorted into a different lamellae.
 - b. β' -2, allows the odd fatty acid B to be packed in perpendicular plane (orthogonal) to the A/C chains
3. β' -3, this polymorph is most tolerant to packing differences as it utilizes the tolerance of the β' structure as well as triple chain length structure. For mixed saturated- unsaturated fatty acid TAGs it is usually found when the TAG is asymmetrical, i.e. SSU is β' -3 whereas SUS is β -3. Thus PPO and POO are asymmetric and OPO and POP is symmetric and β -3 stable.

1.4.2. Binary Phase Behaviour Studies

Studies on the binary phase behaviour of pure TAGs has been concentrated mainly on cocoa butter TAGs. Walker and co – worker studied several fat blends utilizing dilatometry (SFI), wide line NMR and DSC (Walker and Bosin, 1971). The authors noted the significant difference in values obtained by the three methods and stressed the need for the AOCS to implement standard methods for DSC and NMR measurements. Knoster et.al. (1972) then studied the binary phase behaviour of TAGs containing palmitic and stearic acids using microcalorimetry.

This study produced 15 phase diagrams of which 10 demonstrated eutectic behaviour. It is worthy to mention here that eutectic behaviour was demonstrated in all mixtures containing at least one asymmetric TAG and more specifically in the SSP/SPS, symmetric-asymmetric mixture.

In a 50:50 tripalmitin (PPP)/tristearin (SSS) mixture miscibility was observed in both the α and β' forms. However in the β polymorph they do not form a continuous solid as the $\beta' \rightarrow \beta$ transformation is accompanied by a split in the long spacing of the synchrotron XRD spectra. This is further confirmed by two distinct exothermic peaks in DSC. As crystallization progresses, the TAGs co-crystallize to form a continuous solid but at each drop in temperature the solid liquid equilibrium fails to be re-established, since the solid state limits the incorporation of one component into the other (Kellens M., 1991b). Comparing this binary study to that of the pure component TAGs, the major difference is greater presence of the β' polymorph in the blend. The greater stability of the β' form in blends is explained by the fact that chain length difference causes discontinuous methyl ends that, favors orthorhombic packing and sterically hinders $\beta' \rightarrow \beta$ transformation (Hageman and Rothfus, 1983; Kellens M., 1991b). In the pure systems, the β' form could have only been obtained from the melt and transformed quickly to the β polymorph. However, in the binary mixture the β' polymorph can be obtained either directly from the melt by cooling or from the crystallized α form via melt crystallization. The β' form obtained by melts crystallization of the α form is however less stable and quickly transforms to the β form. This is thought to occur because of greater order in the α melt which would facilitate faster nucleation and hence crystallization in the β form. Gibon and co-workers produced phase diagrams for binary mixtures of PPP/PSP and PPP/POP using DSC data and monitored polymorphism using dynamic XRD (Gibon et al., 1986). Monotectic interactions occurred as well as compound formation, according to the nature of the polymorphic form of the TAG. Stability of the β' polymorph depending upon how it was crystallized was analogous to (Kellens M., 1991b) study of PPP/SSS binary mixtures.

Rossel's (1967) review of phase diagrams indicated that eutectics are formed in POP/SOS and POP/SOS. Since then, tremendous amounts of work on these TAGs have been achieved using various experimental techniques.

Binary mixtures of SOS/SSO and SOS/OSO were studied and compound formation at a ration of 1:1 was reported (Engstrom, 1992; Koyano et al., 1992). Minato and co-workers study of the binary POP/PPO mixture revealed two monotectic phases, PPO/compound and compound/POP with compound formation occurring at a 1:1 ratio (Minato et al., 1997). Interestingly the compound had a double chain length structure while the pure components had a triple chain length structure. It seems that this transformation is caused by molecular interactions through oleic acid chains which are packed in the same leaflets in the double structure. Rousset and co-workes used DSC and polarized light microscopy to predict the polymorphism and solidification kinetics of the binary POS / SOS system (Rousset et al., 1998). Increasing concentration of the asymmetric POS was found to have slowed crystallization.

Other binary phase behaviour studies have looked at the interaction of mixtures of *cis* monounsaturated fatty acids found in biomembranes to better understand their physical properties and biological functions. Inoue studied the phase behaviour of oleic acid/palmitoleic acid and oleic acid/myristoleic acid binary mixtures using DSC (Inoue et al., 1992). It was found that the miscibility and compound formation were influenced by the conformational state of the ω chain (i.e. ordered γ form or disordered α form) as well as the stoichiometry of the two components. Eutectic behaviour was also observed in this study and was attributed to weaker intermolecular interactions between different molecular species than the interaction between like pairs. The results of this study suggest that interaction of molecular pairs with different Δ -chain length is energetically less favorable than that of molecular pairs with different ω - chain but the same Δ -chain length. In a subsequent study by (Inoue et al., 1993), the binary phase behaviour of palmitoleic (C:16; ω 7, Δ 9) / asclepic (C:18; ω 7, Δ 11) acid mixture was studied. The phase diagram in this study indicated eutectic behaviour as well, which demonstrates that the two components are perfectly miscible in the liquid phase but much less miscible in the solid α phase. Summarizing the two studies (Inoue 1992, 1992), *cis*-monounsaturated fatty acids differing in Δ chain length are miscible or sparingly miscible in the α phase regardless of the matching ω chain length. However different ω - chain length but same Δ chain length exhibit mutual miscibility in the solid α phase. Using DSC the solid-liquid phase behaviour of oleic acid (OA)/stearic acid (SA) and oleic (OA)/behenic acid (BA)

mixtures (Inoue et al., 2004b) demonstrated a monotectic type temperature/composition phase diagram for both systems. The two fatty acid mixtures were immiscible in the solid phase regardless of the two polymorphs of OA, i.e. α or γ . Immiscibility in the solid phase was confirmed by FT-IR which could be deconvoluted into spectra characteristic of the individual components. In the liquid phase the OA / SA mixture formed an ideal mixture while the OA / BA mixture was slightly non-ideal. Binary mixtures of oleic acid with lauric (LA), myristic (MA) and palmitic (PA) acid were also studied using DSC and FT-IR. All binary mixtures produced a non equilibrium solid phase which eventually reached an equilibrium state upon annealing at a temperature just below the melting point (Inoue et al., 2004a). In the solid phase, the fatty acid species were immiscible and phase separation took place. The non ideality in mixing behaviour increased appreciably with increasing chain length mismatch between the fatty acid species in the respective binary mixtures.

The phase behaviour of natural fats has also been studied by many researchers in order to understand how blends will interact. For example, (Humphrey and Narine, 2004a) investigated binary lipid systems composed of full hydrogenated samples of canola, cottonseed, lard, palm, soybean, and tallow blended to different concentrations with unhydrogenated soybean oil. Such mixtures would usually comprise the feedstock for industrial shortenings. The phase behaviour of other fats of importance includes cocoa butter, milk fat, lauric fats, lard and hydrogenated fats among others. Natural fats on average contain at least 10 different TAG species and display very complex behaviour. Such complexity exemplified by an early study which produced 15 phase diagrams from TAGs containing only two fatty acids (Knoster and DeBruijne, 1972), makes it impossible to construct multi-component phase diagrams of natural fats. Instead the approach is to construct a phase diagram treating each fat as a single component. Experimentally this presents a challenge particularly with DSC since the melting behaviour is complicated by the melting of the different components contributing to less resolved DSC peaks. SFC in combination with XRD is often the choice of analysis used to construct iso-solid lines (Knoster and DeBruijne, 1972; Timms, 1984).

Studying the phase behaviour of individual classes of pure TAGs and their binary mixtures is a more systematic approach which will enable the understanding of the

physical properties of complex lipid materials. It seems however that such research has been limited by the unavailability or the cost of pure TAGs. For TAGs forming a compound mixture, separation by fractionation is not an option.

1.5. Objectives

The broad objectives of the research described in this thesis are to test the hypotheses stated below as well as gain a fundamental understanding of the interaction between positional isomers of TAGs.

1. Positional isomers, particularly asymmetric TAGs will lead to eutectic formation due to disruptive packing in the solid state.
2. TAGs with increasing chain length mismatch will cause eutectic formation as a function of the degree of mismatch. A large chain length mismatch will result in “gaps “where the methyl terrace interacts.
3. The inertial mass of the TAG molecule will affect crystallization and polymorphic transformations.
4. Since TAGs crystallize in metastable states, “apparent eutectics” may be mitigated or shifted, by different crystallization rates.

From the foregoing literature review (see particularly Table 1-1), one can see that most phase behaviour studies relied primarily on DSC. Melting behaviour however, does not necessarily correlate with solid fat content or hardness due to the complexity of the structure of lipid materials. TAGs transform from liquid to solid, through different structure hierarchies as shown in Figure 1-5. All levels of structure cannot be reached using a single analytical technique. The use of different and appropriate tools is needed to understand these rather complex systems.

In addition to a fundamental understanding, the phase behaviour of positional isomers of saturated TAGs containing stearic acid is important to *trans* free products produced by the interesterification. Fully hydrogenated canola oil for example which is abundant in Canada contains over 80% stearic acid. When interesterified with tropical oils such as palm and coconut, there is a possibility of LLS, LSL, PPS, PSP, MMS or MSM being formed.

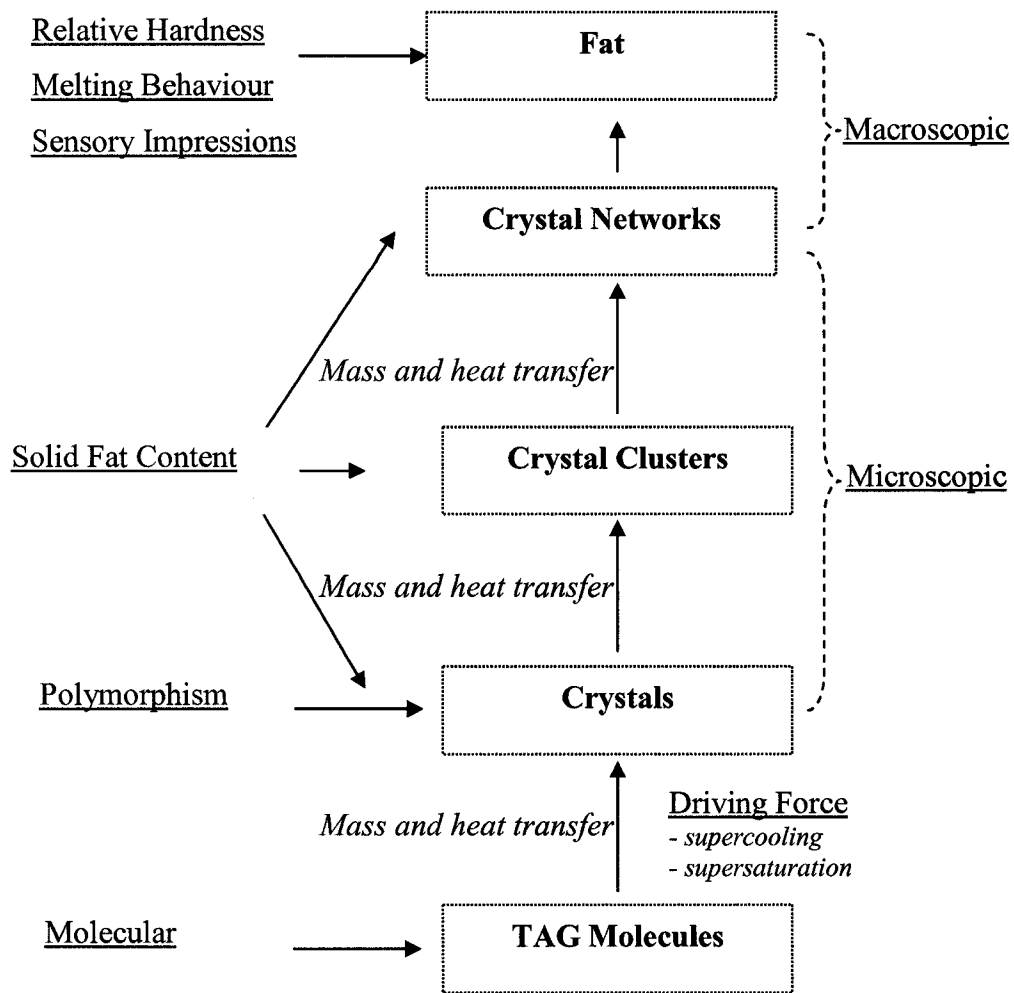


Figure 1- 5. Structural hierarchy of fat crystal network (Adapted from (Narine and Marangoni, 2004))

1.6. References

- Arisima, T., 1989. Polymorphism of POP and SOS. III. Solvent crystallization of beta-2 and beta-1 polymorphs. *Journal of American Oil Chemists' Society* 66, 1614-1617.
- Atkins, P.W., 1998. Phase Diagrams. In: *Physical Chemistry* Oxford University Press, Oxford, p 191.
- Bailey, A.E., 1951. *Industrial Oil and Fat Products*, 2 ed. Interscience Publishers Inc., New York, pp 1-125.
- Bruin, S., 1999. Phase equilibria for food product and process design. *Fluid Phase Equilibria* 158-160, 657-671.
- De Jong, S., Van Soest, T.C., 1978. Crystal structures and melting points of saturated triglycerides in the b-2 phase. *Acta Crystallographica, Section B: Structural Crystallography and Crystal Chemistry* B34, 1570-83.
- Elisabettini, P., Lognay, G., Desmedt, A., Culot, C., Itasse, N., Deffense, E., Durant, F., 1998. Synthesis and physiochemical characterization of mixed acid triglycerides that contain elaidic acid. *Journal of American Oil Chemists' Society* 75, 285-291.
- Engstrom, L., 1992. Triglyceride systems forming molecular compounds. *Journal of Fat Science and Technology* 94, 173-181.
- Fahey, D.A., Small, D.M., Kodali, D.R., Atkinson, D., Redgrave, T.G., 1985. Structure and polymorphism of 1,2-dioleoyl-3-acyl-sn-glycerols. Three- and six- layered structures. *Biochemistry* 24, 3757-3764.
- Ghotra, B.S., Dyal, S.D., Narine, S.S., 2002. Lipid shortenings: A review. *Food Research International* 35, 1015-1048.
- Gibon, V., Durant, F., Deroanne, C., 1986. Polymorphism and intersolubility of some palmitic, stearic, and oleic triglycerides: PPP, PSP, and POP. *Journal of American Oil Chemists' Society* 63, 1047-1055.

- Grey, M.S., Lovengren, N.V., 1978. Polymorphism of saturated triglycerides: 11. 1,3-dipalmito triglycerides. *Journal of American Oil Chemists' Society* 55, 601-606.
- Hageman, J.W., Rothfus, J.A., 1983. Polymorphism and transformation energetics of standard monoacid triglycerides from differential scanning calorimetry and theoretical modeling. *Journal of American Oil Chemists' Society* 68, 1123-1131.
- Hagemann, J.W., 1988. Thermal behavior and polymorphism of acylglycerides. *Surfactant Science Series* 31, 9-95.
- Hagemann, J.W., Tallent, W.H., Barve, J.A., Ismail, I.A., Gunstone, F.D., 1975. Polymorphism in single -acid triglycerides of positional and geometric isomers of octadecanoic acid. *Journal of American Oil Chemists' Society* 52, 204-207.
- Hagemann, J.W., Tallent, W.H., Kolbe, K.E., 1972. Differential scanning calorimetry of single acid triglycerides: Effect of chain length and unsaturation. *Journal of American Oil Chemists' Society* 49, 118.
- Hildebrand, J.H., 1929. Solubility XII Regular solutions. *Journal of the American Chemical Society* 51, 66-80.
- Himawan, C., Starov, V.M., Stapley, A.G.F., 2006. Thermodynamic and kinetic aspects of fat crystallization. *Advances in Colloid and Interfacial Science* 122, 3-33.
- Humphrey, K.L., Moquin, P.H.L., Narine, S.S., 2003. Phase behavior of a binary lipid shortening system: From molecules to rheology. *Journal of American Oil Chemists' Society* 80, 1175-1182.
- Humphrey, K.L., Narine, S.S., 2004a. A comparison of lipid shortening functionality as a function of molecular ensemble and shear: Crystallization and melting. *Food Research International* 37, 11-27.
- Humphrey, K.L., Narine, S.S., 2004b. Lipid phase behavior. In: *Fat Crystal Networks* Marcel Dekker, New York, pp 83-114.

- Inoue, T., Motoda, I., Hiramatsu, N., Suzuki, M., Sato, K., 2004a. Phase behaviour of binary mixture of palmitoleic acid(cis-9-hexadecanoic acid) and asclepic acid (cis-11-octadecanoic acid). *Chemistry and Physics of Lipids* 66, 209-214.
- Inoue, T., Motoda, I., Hiramatsu, N., Suzuki, M., Sato, K., 1992. Phase behavior of binary mixtures of cis-monounsaturated fatty acids with different w-chain length. *Chemistry and Physics of Lipids* 63, 243-50.
- Inoue, T., Motoda, I., Hiramatsu, N., Suzuki, M., Sato, K., 1993. Phase behavior of binary mixture of palmitoleic acid (cis-9-hexadecenoic acid) and asclepic acid (cis-11-octadecenoic acid). *Chemistry and Physics of Lipids* 66, 209-14.
- Inoue, T., Motoda, I., Hisatsugu, Y., Yamamoto, R., Suzuki, M., 2004b. Solid-liquid phase behaviour of binary fatty acid mixtures 1. Oleic acid/stearic acid and oleic acid/behenic acid mixtures. *Chemistry and Physics of Lipids* 127, 143-152.
- IUPAC, 1978. The nomenclature of lipids. (Recommendations 1976). *Chemistry and Physics of Lipids* 21, 159-73.
- Kellens M., M.W., Gehrke R., Reynaers H., 1991a. Synchrotron radiation investigations of polymorphic transitions of saturated monoacid triglycerides. Part 1: Tripalmitin and tristearin. *Chemistry and Physics of Lipids* 58, 131-144.
- Kellens M., M.W., Gehrke R., Reynaers H., 1991b. Synchrotron radiation investigations of the polymorphic transitions in saturated monoacid triglycerides. Part2: Polymorphism study of a 50:50 mixture of tripalmitin and tristearin during crystallization and melting. *Chem. Phys. Lipids* 58, 145-158.
- Knoster, M., DeBruijne, P., 1972. The solid-liquid equilibrium of binary mixtures of triglycerides with palmitic and stearic chains. *Chemistry and Physics of Lipids* 9, 309-319.
- Kodali, D.R., Atkinson, D., Redgrave, T.D., 1984. Synthesis and polymorphism of 1,2-dipalmitoyl-3-acyl-sn-glycerols. *Journal of American Oil Chemists' Society* 61, 1078-1084.

- Kodali, D.R., Fahey, D.A., Small, D.M., 1990. Structure and Polymorphism of Saturated Monoacid 1,2-Diacyl-sn-Glycerols. *Biochemistry* 29, 10771-10779.
- Koyano, T., Hachiya, I., Arishima, T., Sato, K., Sagi, N., 1989. Polymorphism of POP and SOS. II. Kinetics of melt crystallization. *Journal of American Oil Chemists' Society* 66, 675-679.
- Koyano, T., Hachiya, I., Sato, K., 1992. Phase behavior of mixed systems of SOS and OSO. *Journal of Physical Chemistry* 96, 10514-10520.
- List, G., Mounts, T.L., Orthoefer, F., Neff, W., 1995. Margarine and shortening oils by interesterification of liquid and trisaturated triglycerides. *Journal of American Oil Chemists' Society* 72, 379-382.
- Lovegren, N.V., Gray, M.S., 1978. Polymorphism of saturated triglycerides: 1. 1,3-distearo triglycerides. *Journal of American Oil Chemists' Society* 55, 310-316.
- Mensink, R., Katan, M., 1993. Trans monounsaturated fatty acids in nutrition and their impact on serum lipoprotein levels in man. *Progress in Lipid Research* 32, 111-122.
- Minato, A., Ueno, S., Smith K., Amemiya, Y., Sato, K., 1997. Thermodynamic and kinetic study on phase behaviour of binary mixtures of POP and PPO forming molecular compound systems. *Journal of Physical Chemistry B* 101, 3498 - 3505.
- Moore, W.J., 1983. States of Matter. In: *Basic Physical Chemistry* Prentice-Hall, Englewood Cliffs, New Jersey, pp 27.
- Narine, S.S., Marangoni, A.G., 2004. The Nature of Fractality in Fat Crystal Networks. In: *Fat Crystal Networks* Marcel Dekker, New York, pp 236-240.
- Nor Aini, I., Razali, I., Noor Lida, H.M.D., Miskandar, M.S., Radzuan, J., 2002. Blending of palm oil and palm products with other oils and fats for food applications. *Oil Palm Bulletin* 45, 6-15.

- O' Brien, R.D., 2004. Fats and oils: formulating and processing for applications, 2nd ed. CRC Press Boca Raton, Florida, pp 127-250.
- Padley, F.B., Podmore, J., 1985. The Role of Fats in Human Nutrition John Wiley & Sons Inc, New York, p 210.
- Rodrigues, J.N., Gioioelli, L.A., 2003. Chemical interesterification of milkfat and milkfat-corn oil blends. Food Research International 36, 149-159.
- Rossel, J.B., 1967. Phase diagrams of triglyceride systems. Advances in Lipid Research 5, 353-408.
- Rousset, P., Rappaz, M., Minner, E., 1997. Solidification kinetics of cocoa butter and of its main components, the triacylglycerols POP, POS and SOS. Solidification Processing 1997, Proceedings of the Decennial International Conference on Solidification Processing, 4th, Sheffield, UK, July 7-10, 1997, 586-590.
- Rousset, P., Rappaz, M., Minner, E., 1998. Polymorphism and solidification kinetics of the binary system POS-SOS. Journal of the American Oil Chemists' Society 75, 857-864.
- Rozenaal, A., 1992. Interesterification of fats and oils. INFORM 3, 1232-1237.
- Sato, K., 1999. Solidification and phase transformation behaviour of food fats- a review. Fett/Lipid 101, 467-474.
- Sato, K., 2001. Crystallization behaviour of fats and lipids- a review. Chemical and Engineering Science 56, 2255-2265.
- Sato, K., Arishima, T., Wang, Z.H., Ojima, K., Sagi, N., Mori, H., 1989. Polymorphism of POP and SOS. 1. Occurrence and polymorphic transformation. Journal of American Oil Chemists' Society 66, 664-674.
- Sato, K., Ueno, S., Yanko, J., 1999. Molecular interactions and kinetic properties of fats. Progress in Lipid Research 38, 91-116.

- Soumanou, M.M., Bornscheuer, U., Schmid, T., Schmid, U., Rolf, D., 1998. Synthesis of structured triglycerides by lipase catalysis *Fett/Lipid* 100, 156-160.
- Sreenivasan, B., 1978. Interesterification of Fats. *Journal of American Oil Chemists' Society* 55, 796-805.
- Timms, R., 2003. Physical Chemistry. In: *The Confectionary Fats Handbook: Properties, Production, and Application*. The Oily Press, Bridgewater, pp. 9-63.
- Timms, R.E., 1984. Phase behaviour of fats and their mixtures. *Progress in Lipid Research* 23, 1-38.
- Ueno, S., Minato, A., Yano, J., Sato, K., 1999. Synchrotron radiation X-ray study of polymorphic crystallization of SOS from liquid phases. *Journal of Crystal Growth and Design* 198/199, 1326-1329.
- van Langevelde, A., Peschar, R., Schenk, H., 2001. Structure of beta-trimyristin and beta-tristearin from high-resolution x-ray powder diffraction data. *Acta Crystallographica, Section B: Structural Science* B57, 372-377.
- van Langevelde, A., van Malssen, K., Hollander, F., Peschar, R., Schenk, H., 1999a. Structure of mono-acid even-numbered beta-triacylglycerols. *Acta Crystallographica, Section B: Structural Science* B55, 114-122.
- van Langevelde, A., van Malssen, K., Sonneveld, E., Peschar, R., Schenk, H., 1999b. Crystal packing of a homologous series beta prime-stable triacylglycerols. *Journal of American Oil Chemists' Society* 76, 603-609.
- van Soest, T.C., de Jong, S., Roijers, E.C., 1990. Crystal structures and melting points of saturated triacylglycerols in the beta-3 phase. *Journal of American Oil Chemists' Society* 67, 415-423.
- Walker, R.C., Bosin, W.A., 1971. Comparison of SFI, DSC and NMR Methods for determining solid-liquid ratios in fats. *Journal of American Oil Chemists' Society* 48, 50-53.

2. The binary phase behavior of 1, 3 – dilauroyl-2-stearoyl-*sn*-glycerol and 1, 2 – dilauroyl-3-stearoyl-*sn*-glycerol

2.1. Introduction

Transesterified fats that originate from natural sources, such as coconut oil and vegetable oils, can be a convenient source of low of *zero-trans* fats and have recently become important in the manufacturing of food products such as chocolate, margarine, and frostings, just to name a few (de Roos et al., 2003; List et al., 1995). Triacylglycerols (TAGs) are the predominant component in these fats and oils (O' Brien, 2004). A TAG molecule consists of three fatty acid moieties esterified to a glycerol backbone. The distribution of fatty acids on the glycerol backbone *i.e.* the number of carbons in the fatty acid chain and its position on the glycerol is uniquely dictated by the organism from which the TAG molecule is extracted (Sreenivasan, 1978).

The positional distribution of fatty acids on the glycerol backbone is of great fundamental and industrial importance. Mixed acid TAGs can result in a chain-length mismatch between the different fatty acids in the molecule and has been shown to strongly influence the phase behavior and the physical properties of fats (Humphrey and Narine, 2004; Rossel, 1967; Timms, 1984).

This thesis details a study of model fat systems made of binary mixture of TAG isomers constituted of two different A and B fatty acids having the symmetric BAB and asymmetric BBA structures.

The symmetric BAB TAGs are reported to have different properties (such as a higher melting point) than their asymmetrical BBA counterparts (van Soest et al., 1990). The presence of symmetric/asymmetric species within the same sample can result in significant effects on texture, melting and polymorphic forms.

The different TAGs chosen for this study all contain stearic acid (A = S) and another different fatty acid (B= Lauric, L, Myristic, M and Palmitic, acids).

A version of this chapter has been submitted for publication to Chemistry and Physics of Lipids, May 2007.

Stearic acid is present at elevated concentration in hydrogenated fats because double bonds are removed from the 18:1, 18:2 and 18:3 unsaturated fatty acids during hydrogenation (Bockisch, 1998). Fully hydrogenated canola oil, for example, contains about 86% stearic acid (Firestone, 1999). The fatty acids have been chosen to conduct a survey of the effect of chain-length mismatch on the polymorphism, phase behavior, and rheological properties of the symmetric/asymmetric binary systems. These systems are relevant to identifying the industrial implications for the processing of lipid samples containing positional isomers due to interesterification and more generally to understanding the phase behavior of complex fats and oils.

In this first study, we report on the polymorphism, crystallization, melting and rheological properties of the 1, 3 – dilauroyl-2-stearoyl-*sn*-glycerol/1, 2 – dilauroyl-3-stearoyl-*sn*-glycerol (LSL/LLS) binary system. The chain length mismatch for these TAGS is relatively high and equal to six. Fully hydrogenated coconut oil (FHCO) contains 50.3% lauric acid and 15.5% stearic acid (Firestone, 1999), the first and third most abundant fatty acids in FHCO, respectively. Given the abundance of these fatty acids, the chance of having the positional isomers LLS and LSL in samples of FHCO which have been interesterified with canola oil is very high, as demonstrated by Pham and coworkers (Pham et al., 1998) in their regiospecific analysis of TAGs extracted from coconut oil. This highlights the industrial importance of this system.

The samples were processed at two extreme crystallization rates, namely 0.1 °C/min and 3.0 °C/min, in order to understand the influence of crystallization conditions on the above named properties.

2.2. Materials and Methods

2.2.1. Sample Preparation

The pure LSL and LLS TAGs were synthesized according to known procedures (Bentley and McCrae, 1970). Purity of all samples exceeded 97.0% as determined by gas chromatography fitted with a mass spectrometer detector. The purified TAGs were melted at 90°C, held for 5 minutes and stirred using a mechanical stirrer.

Homogenous mixtures of LSL molar fraction, x_{LSL} of 0.1, 0.2, 0.4, 0.5, 0.6 and 0.8 were prepared by mixing the purified samples with a mechanical stirrer for 5 minutes.

2.2.2. Thermal Processing

A Linkam LS 350 (Linkam Scientific Instruments, Tadworth, Surrey, United Kingdom) temperature chamber was used to process samples for x-ray diffractometry, microscopy and relative hardness measurements. For differential scanning calorimetry analysis, the samples were processed by the instrument itself. All samples were subjected to the same thermal profile. They were heated to 90°C and held for 5 minutes to erase crystal memory, cooled at a constant rate (of 0.1 °C/min or 3.0 °C/min) and held isothermally at 15 °C for 1 hour. Samples in the differential scanning calorimeter were melted immediately after the isothermal holding period at a constant heating rate of 5.0 °C/min to 90 °C. All measured temperatures are reported to a certainty of ± 0.5 °C.

2.2.3. X-ray Diffraction (XRD)

A Bruker AXS X-ray diffractometer equipped with a filtered Cu-K α radiation source ($\lambda = 0.1542$ nm) and a 2D detector was used to obtain XRD patterns as previously outlined for lipid systems (Humphrey et al., 2003). The procedure was automated and controlled by Bruker AXS's "General Area Detector Diffraction System" (GADDS V 4.1.08) software. Frames were processed using the GADDS software and the resulting spectra were analyzed with Bruker AXS's "Topas V 2.1" software.

2.2.4. Differential Scanning Calorimetry (DSC)

The samples were fully melted and approximately 10 - 15.0 ± 0.1 mg was placed in an aluminum DSC pan. Samples were run using a TA- Q100 Series Modulated DSC (TA, Instruments, New Castle, DE.) operated in the standard mode. Data analysis was performed using the TA Universal Analysis software coupled with methods developed by our group (Bouzidi et al., 2005).

2.2.5. Solid Fat Content (SFC)

The use of nuclear magnetic resonance (NMR) technique in the detection of solid fat contents makes use of the large differences in spin-lattice relaxation rates between the solid component and the liquid phase. In an NMR experiment, the nuclear

spins of the sample align with the static magnetic field. When a calibrated pulse of radio frequency is passed through the sample, the nuclear spins effectively tip into the plane transverse to the static magnetic field and as the nuclear spins return to alignment they give off a detectable RF signal. The rate of this signal decay is known as spin-lattice or T1 relaxation. The T1 relaxation rates observed for solids compared to liquids can be orders of magnitude higher and thus allow for sufficient differentiation between the two states of matter (Hamilton and Bhati, 1987). For the purposes of this study, a Bruker Minispec mq 20 spectrometer (Milton, Ontario, Canada) was used. .

Thermal processing inside the NMR probe was controlled and maintained by a series of external water baths connected to the NMR probe as described by (Narine and Humphrey, 2004). Samples were heated to 90 °C, held for 5 minutes and then cooled to 67 °C outside of the spectrometer. At this point the sample was immediately transferred to the NMR probe, and data acquisition was started; collecting %SFC data at 10 s intervals throughout the entire cooling process. A constant cooling rate was maintained until the final holding temperature (15 °C) was achieved.

2.2.6. Relative Hardness

Hardness was measured in open DSC pans containing equal amounts (~ 50 mg) of sample. Tempered samples were rapidly transferred for testing to an Autotune CAL 9300 (CAL Controls Ltd., Herts U.K.) temperature controlled chamber fitted to a TA.XT plus texture analyzer (Stable Microsystems, Surrey U.K.). They were then penetrated at a constant speed of 0.5 mm/s to a depth of 1.5 mm. The texture analyzer was fitted with a 1.0 kg load cell and standard needle (cone 8° 55') commonly used for testing waxes (ASTM-Designation: D 1321-65). Penetration and data acquisition were controlled by the Texture Exponent 32 (Version 2.0.0.7 www.SaxSoft.com) software provided with the TA.XT. Hardness measurements were taken immediately after the samples were held isothermally for one hour. Forces versus displacement graphs were plotted and the maximum force detected was chosen as a measure of the relative hardness.

2.2.7. Microscopy

A Leica DMRX polarized light microscope (Leica Microsystems, Wetzlar, Germany) fitted with a Hamamatsu (C4742-95) digital camera was used for image capture. Micrographs were taken after the sample was held for 1 hour at 15 °C.

2.3. Results and Discussion

2.3.1. XRD Results

Figure 2-1 shows XRD spectra of the different LSL/LLS mixtures obtained at a cooling rate of 0.1 °C/min. At the bottom is the spectrum of pure LLS and the subsequent spectra above correspond to progressively increasing LSL molar fraction mixtures. The spectrum at the top of Figure 2-1 corresponds to pure LSL. For discussion purposes, the 2θ range is divided into 2 regions: the small angle region where $2\theta \leq 18^\circ$ (long spacing region) and the wide angle region with $18^\circ \leq 2\theta \leq 30^\circ$ (short spacing region).

In the long spacing region, four distinct peaks are present in all the XRD spectra. The peaks observed for the pure LLS and LSL samples are labeled in Figure 2-1. These four peaks are grouped into two series, P comprised of peaks P_1 and P_2 (with d -spacing values of d_1 and d_2 , respectively) and P' comprised of peaks P'_1 and P'_2 (with d -spacing values of d'_1 and d'_2 , respectively).

The ratios of d -spacing for the two series (*i.e.* $d_1 : d_2$ and $d'_1 : d'_2$) were both found to be $1:1/2$ which is characteristic of a lamellar periodicity (Fontell, 1974). Furthermore, the angle of tilt, θ , of the lamellar repeat unit can be determined from the parallel spacing, d_1 , and perpendicular spacing, d'_1 using the relation $\tan(\theta) = \frac{d_1}{d'_1}$ (see Figure 2-2 (A)). The angles of tilt were identical for all bilayers in all samples ($\theta = 52 \pm 2^\circ$). Figure 2-2 (B) shows d_1 , d'_1 , d_2 and d'_2 long spacing as a function of LSL mole fraction, x_{LSL} . As can be seen, all long spacing values remain unchanged for all molar fractions.

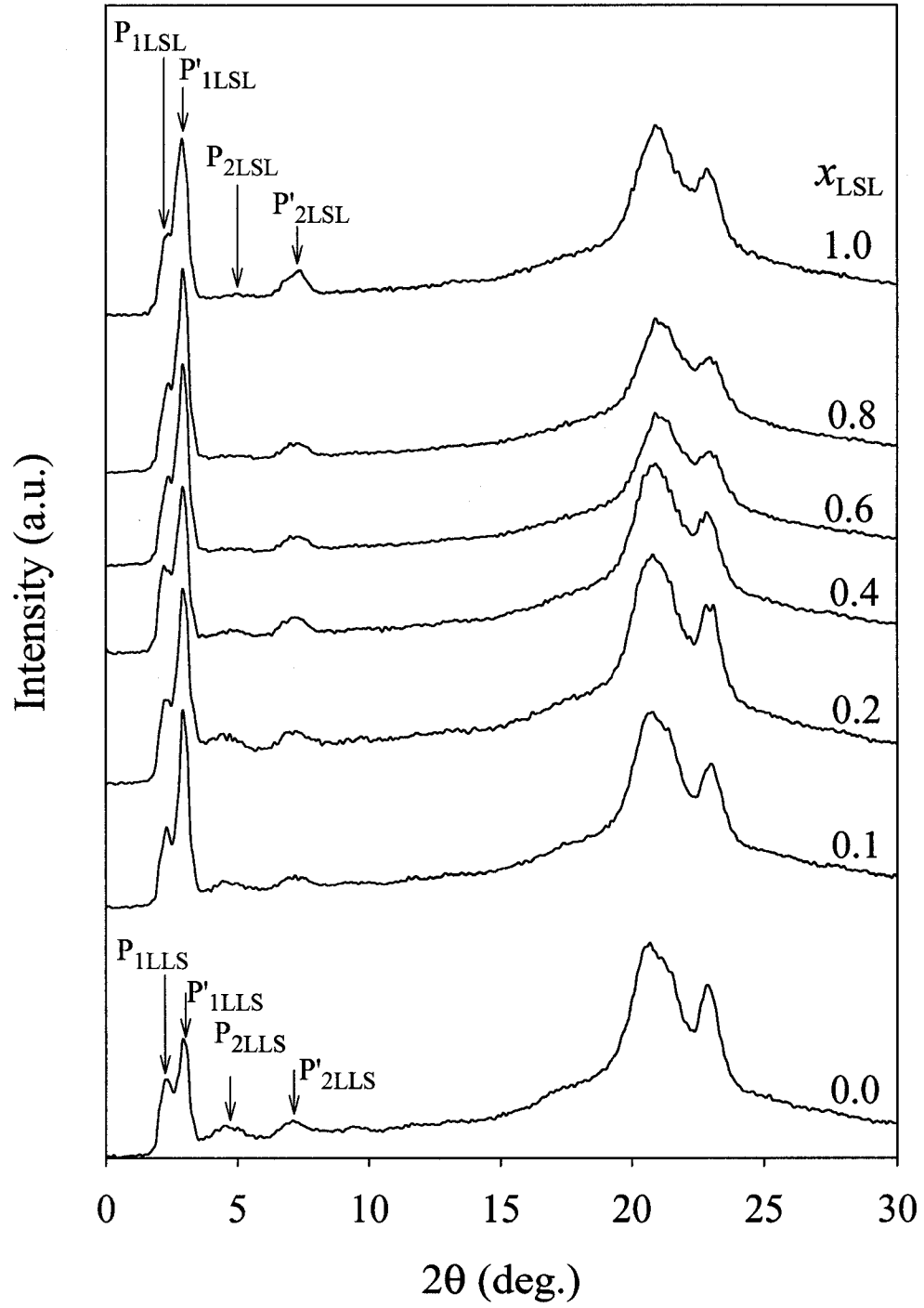


Figure 2-1. XRD spectra of LSL/LLS mixtures crystallized at 0.1°C/min.

From the long spacing values for the pure TAGs the length of the corresponding bilayers (L) can be determined by $L = \frac{d_1}{\cos(\theta)}$. This results in an L value of $47.9 \pm 1.5 \text{ \AA}$ and $47.5 \pm 1.3 \text{ \AA}$ for LSL and LLS, respectively.

Shown in Figure 2-2 (A) we propose two double layer packing modes for (i) the pure, symmetric, LSL and (ii) pure, asymmetric, LLS samples. The bilayer lengths obtained from our packing models agrees very well with bilayer lengths obtained from XRD, assuming the distance between two sp^3 carbon atoms is 1.54 \AA and a tetrahedral bond angle of 109.5° (Harrison, 1980).

In the short spacing range, the XRD spectra of the two pure TAGs have similar shapes with two well resolved peaks, each originating from the same family of plane. The short d -spacing are shown in Figure 2-2(C). As can be seen, the XRD spectra exhibit a strong lattice spacing line at 4.25 \AA (line $d_{1\beta'}$) coupled with another strong line at 3.90 \AA ($d_{2\beta'}$), indicating the presence of a β' polymorph (deMan, 1992; Timms, 1984).

The results of the XRD measurements carried out for the mixtures, processed at the $0.1 \text{ }^\circ\text{C}/\text{min}$ cooling rate, can be explained by two separate situations. In the first case, the components of the mixture are immiscible in the solid, and thus the XRD spectra observed for the mixtures would simply be a superposition of the XRD spectra that would arise from pure LSL and LLS. Since the XRD spectra for the two pure TAGs are nearly identical the resulting superposition of these two spectra would be indistinguishable from either spectrum of the pure TAGs.

The second scenario is reasoned based on the fact that the pure symmetric and pure asymmetric TAGs have nearly identical unit cell parameters. If the two components are miscible in the solid, it is plausible that the resulting solid mixture would result in a crystal with nearly the same unit cell parameters as the two pure TAG samples. Such a mixture would also result in an XRD spectrum that is very similar to the spectra of the two pure TAGs. Given the XRD data alone we can not make a clear conclusion about the miscibility or immiscibility of the solid for the binary mixtures. This point will be clarified and further elaborated upon in the discussion of the phase diagram for these mixtures.

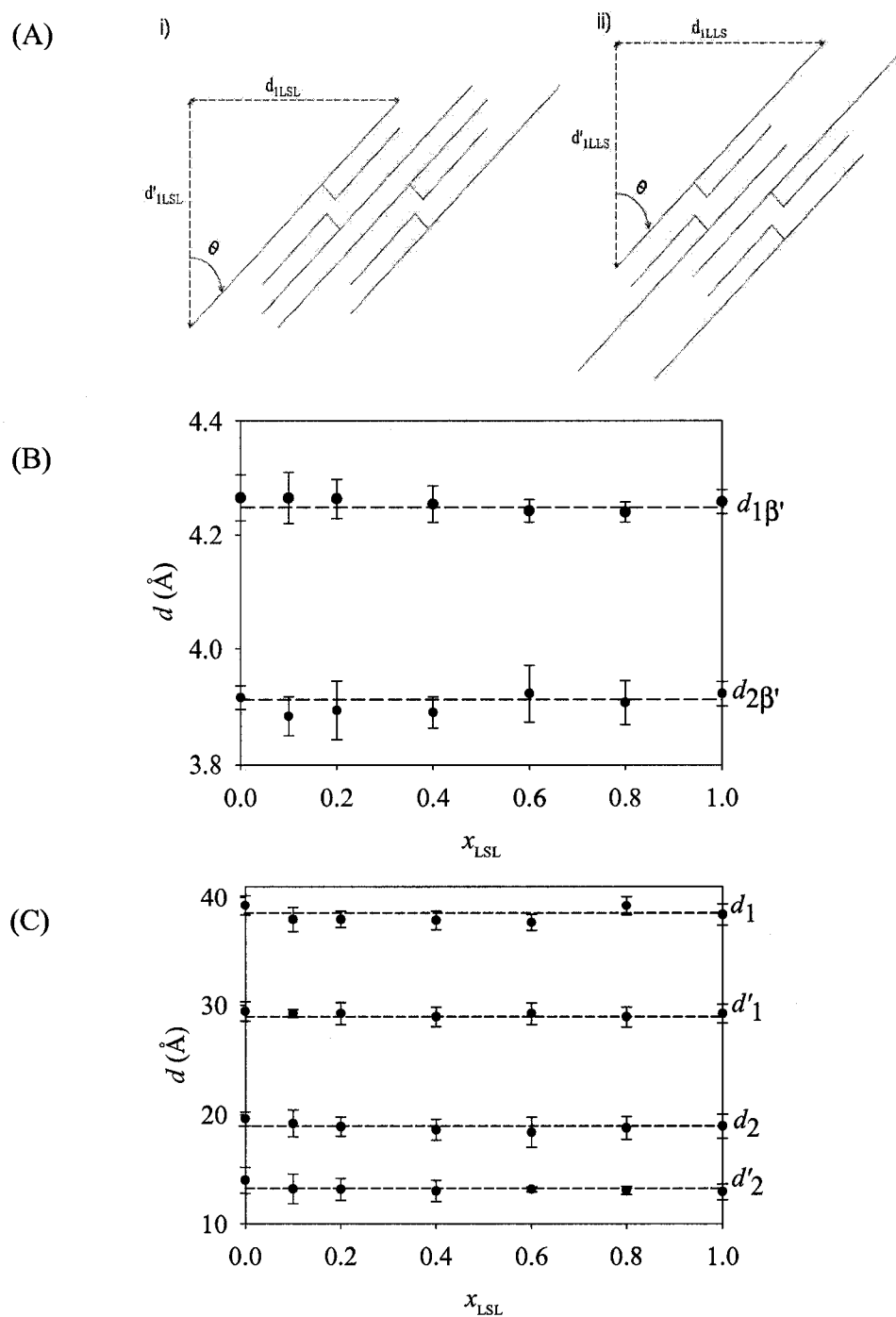


Figure 2-2. (A) Stacking mode of LSL/LLS mixtures. d_1 and d'_1 represent the parallel and perpendicular lamellar periodicities and θ is the angle of tilt, (B) Variation of d_1 , d'_1 , d_2 and d'_2 long spacing vs. LSL molar fraction, (C) Variation of $d_{1\beta}$ and $d_{2\beta}$ short spacing vs. LSL molar fraction. Error bars are standard deviations, $n=3$.

At the 3.0°C/min cooling rate, similar XRD spectra were observed for all samples and correspond to both of the peak series already observed in Figure 2-1. This suggests that cooling rate did not impact the final polymorphic form of the TAGs. As such, the XRD spectra and analysis for the 3.0 °C/min cooling rate is not shown. From the experimental XRD spectra obtained at both cooling rates, it is clear that the crystals formed at all mole fractions have the same orthorhombic sub cells.

2.3.2. DSC Results

2.3.2.1. Crystallization Behavior

Crystallization thermograms were acquired at both 0.1 and 3.0°C/min. For the 0.1°C/min cooling rate, and for all compositions except for $x_{\text{LSL}} = 0.6$, complex crystallization behavior is observed. The crystallization event demonstrated non resolved but identifiable peaks with prominent maxima (Figure 2-3 (A)) underlining the complexity of the crystallization process for such mixtures.

When the cooling rate was increased to 3.0°C/min, the thermograms lost some of their prominent features with each sample showing one large peak whose maximum was shifted towards the low temperature side (Figure 2-3 (B)). This shift of peak maxima with increasing cooling rate is well documented (Smith et al., 2005; Tan and Man, 2002). The formation of a unique polymorph (β' as determined by XRD) at the end of the cooling process for both rates indicates that the “successive” peaks were representative of successive phases transformations or/and successive crystallization events. Time-resolved XRD measurements, usually accomplished by a synchrotron facility, would be necessary to fully characterize these peaks.

The main peak maximum vs. x_{LSL} demonstrated eutectic behavior with a well defined eutectic point close to $x_{\text{LSL}} = 0.1$ for the 0.1 °C/min cooling rate (Figure 2-3 (C)). The enthalpy of crystallization increased linearly as a function of increasing LSL composition as shown in Figure 2-3 (D). Note that the enthalpy curve of crystallization for samples cooled at 0.1 °C/min is higher and almost parallel to the curve for samples cooled at 3.0 °C/min. Clearly, the crystals formed at 0.1 °C/min were better packed with much stronger molecular interactions than the crystals formed at 3.0 °C/min.

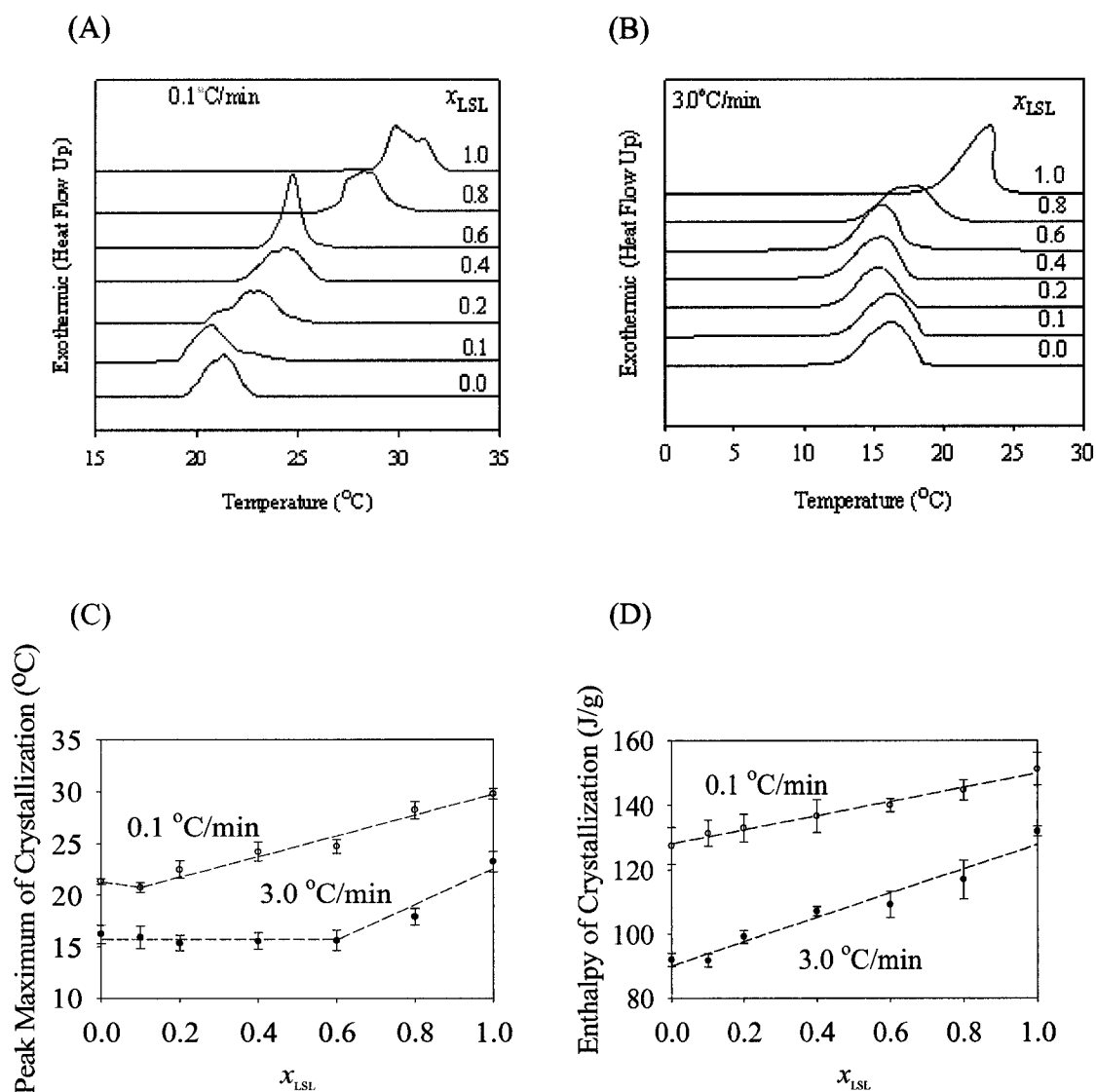


Figure 2-3. (A) Crystallization curves of LSL/LLS binary mixtures vs. LSL molar fraction at 0.1 °C/min, (B) Crystallization curves of LSL/LLS binary mixtures vs. LSL molar fraction at 3.0 °C/min, (C) Peak maximum of crystallization vs. of LSL molar fraction at 0.1 and 3.0 °C/min, (D) Enthalpy of crystallization vs. LSL molar fraction at 0.1 and 3.0 °C/min. Error bars are standard deviations, $n=3$.

The steady increase of the enthalpy with the increase of LSL content at both rates, suggests that the addition of LSL helped to increase homogeneity and density of packing. The almost parallel nature of the curves points to the similar influence of cooling rate on the packing density of each mixture.

2.3.2.2. Melting Behavior

Melting thermograms were acquired at a constant melting rate of 5.0 °C/min for samples crystallized at both 0.1 and 3.0°C/min. For the 0.1 °C/min crystallization cooling rate, single peaks were observed for all compositions (Figure 2-4 (A)). When the crystallization cooling rate was increased 30 times to 3.0 °C/min, much more complex melting behavior is observed particularly for the $x_{LSL} = 0.0$ and 0.1 compositions (see Figure 2-4 (B)), and to a lesser extent for the $x_{LSL} = 0.2$ sample. Purified LLS has three melting peaks (endotherms) separated by two crystallization peaks (exotherms) and $x_{LSL} = 0.1$ has two melting peaks separated by a single crystallization peak.

This kind of melting behavior can be attributed to melt mediated transformations where a polymorph melts, re-crystallizes to a thermodynamically more stable polymorph and finally melt without further transformation (Sato, 1999).

From the exothermic ridge observed prior to the observed phase transition for the $x_{LSL} = 0.0$, 0.1 and 0.2 samples, it can be inferred that the sample is progressing through a more ordered state before moving through the phase transition. The thermal characteristics of the different peaks shown in Figure 2-4 (B) are as follows; P_1 (m.p = 21.2 ± 0.2 °C, $\Delta H_m = 10.3 \pm 0.8$ J/g), P_2 (m.p = 33.5 ± 0.5 °C, $\Delta H_m = 70.5 \pm 0.5$ J/g) and P_3 (m.p = 44.9 ± 0.2 °C, $\Delta H_m = 72.8 \pm 0.3$ J/g) which indicates increasing thermodynamic stability. In the case of the $x_{LSL} = 0.1$ sample, two melting peaks are seen at (m.p. = 20.1 ± 0.2 °C, $\Delta H_m = 1.3 \pm 0.5$ J/g) and (m.p. = 34.6 ± 0.2 °C, $\Delta H_m = 128.5 \pm 0.5$ J/g). For the $x_{LSL} = 0.2$ sample and above, single melting peaks were observed.

There is a close overlay of peak maximum points at both rates. The only deviations from this trend were seen for the samples with multiple melting peaks discussed above. The higher peak maximum of melting for the symmetric TAG suggests a higher degree of intermolecular interactions within the lamellar unit (van Soest et al.,

1990). This would support the XRD data, *i.e.* a common β' polymorph was formed for all compositions at both rates.

For samples cooled at 3.0 °C/min, it is clear from the XRD results that after crystallization, only one polymorph is present, the β' polymorph (deMan, 1992; Timms, 2003).

When the DSC melting curve was obtained, after being held isothermally for 1 hour at 15°C, the multiple peaks that were observed are attributed to phase transformations during the heating. As such, these phase transformations could not be observed by XRD without an *in situ* experimental technique that is currently unavailable to us.

The enthalpy of melting was evaluated for the melting part of the thermal events from the inflexion point following the exotherm considered as the starting point of the endotherm. The values were therefore to some extent overestimated particularly for the 3.0 °C/min melting curves. The enthalpy of the melt increased regularly as a function of increasing LSL composition as shown in Figure 2-4 (C). Note that the enthalpy of the $x_{LSL} = 0.0$ and $x_{LSL} = 0.1$ samples are not reported because accurate measurements of the enthalpy of the melt for individual peaks were not possible. The enthalpy curves for melt almost mirror those for crystallization. Clearly, the crystals formed at the 0.1 °C/min cooling rate are much more thermodynamically stable than those formed at 3.0 °C/min. This difference in thermodynamic stability must be motivated by increased molecular mobility at the 0.1 °C/min cooling rate, leading to preferred packing modes being available for these samples.

2.3.2.3. Phase Diagram of the LLS/LSL Binary System

The LLS /LSL binary phase diagram (0.1 °C/min) is shown in Figure 2-5 (A) and was constructed from the melting thermograms shown in Figure 2-4 (A). The peak maximum of melting temperature was used to represent the liquidus line and the start of melting temperature of the said peaks was used to represent the solidus line.

These temperatures were plotted as a function of x_{LSL} in the mixture, after correction for the transition widths of the pure components (Inoue et al., 1993).

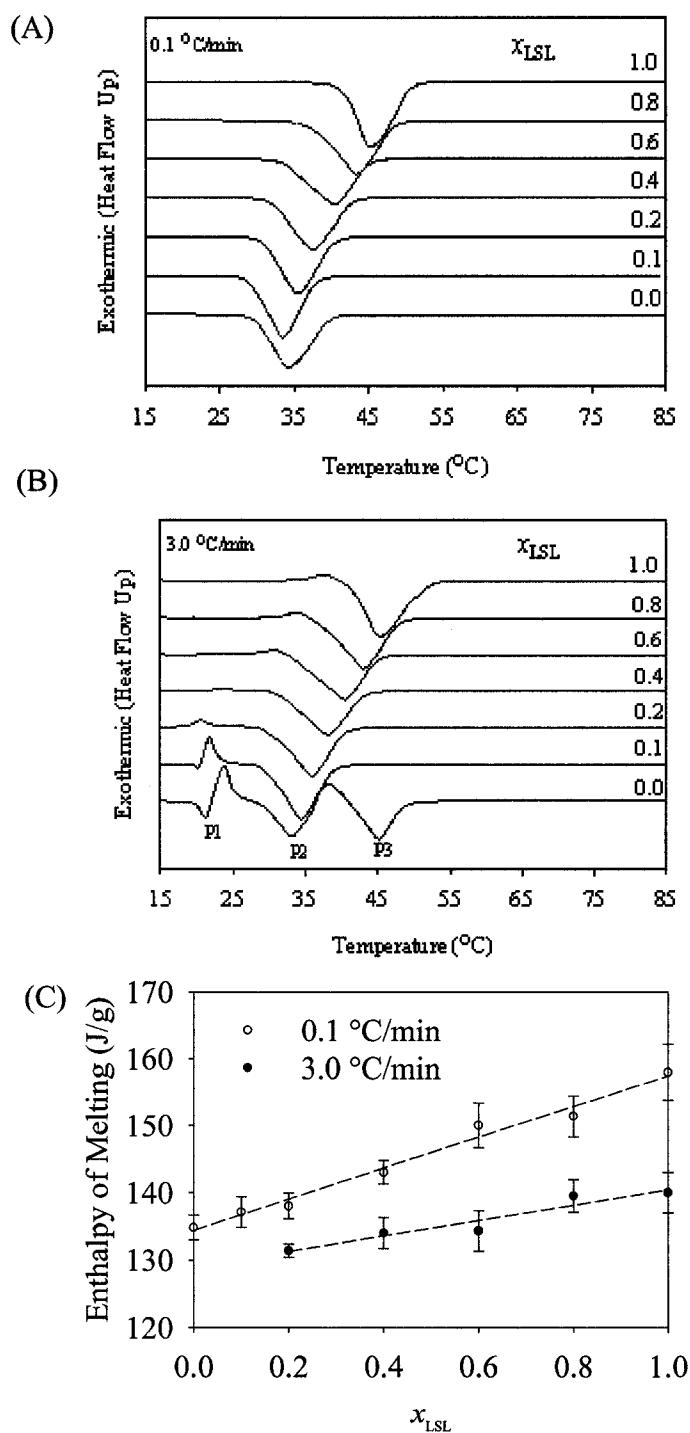


Figure 2-4. (A) Melting curves of LSL/LLS binary mixtures vs. LSL molar fraction at 0.1 °C/min (B) Melting curves of LSL/LLS binary mixtures vs. LSL molar fraction at 3.0 °C/min (C) Enthalpy of melting vs. LSL molar fraction at 0.1 and 3.0 °C/min. Error bars are standard deviations, n= 3.

The diagram exhibits a typical eutectic-type phase boundary with a eutectic composition close to $x_{LSL} = 0.10$ and a eutectic temperature of 34 °C. The nearly horizontal solidus line (Figure 2-5 (B)) in the range of $0 < x_{LSL} < 0.9$ indicates that demixing of the two TAGs (or phase separation) occurs in the solid phase. A eutectic behavior of the LLS/LSL mixture is similar to what has been observed for other common binary mixtures of TAGs such as PPS / SSS (Knoster and DeBruijne, 1972; Rossel, 1967).

A thermodynamic model based on the Hildebrand equation (Hildebrand, 1929) and used to simulate the phase boundary in the *Temperature–molar fraction* phase diagram of a binary mixture is shown in Equations 1 and 2 (Hildebrand, 1929; Inoue et al., 1993; Lee, 1977). This model assumes a binary mixture of components A and B, which are completely immiscible in the solid phase and behave ideally in solution. Given these assumptions, the equilibrium liquidus line of the binary mixture is given by either of the following two equations depending on the composition range.

$$\ln x_A = -\frac{\Delta H_A}{R} \left(\frac{1}{T} - \frac{1}{T_A} \right) \quad (1)$$

$$\ln x_B = -\frac{\Delta H_B}{R} \left(\frac{1}{T} - \frac{1}{T_B} \right) \quad (2)$$

where R is the gas constant, x_A represents the mole fraction of A, ΔH_A and T_A are the molar heat of fusion and the melting point of component A. Similarly, x_B , ΔH_B and T_B are the parameters of component B. In our case, A and B components correspond to pure LLS and LSL samples, respectively.

Equation 1 models the liquidus in the $x_E \leq x_A \leq 1$ range and equation 2 models it in the $0 \leq x_A \leq x_E$ range. The liquidus line was calculated from Equations (1) and (2) using $\Delta H_A = 97.3 \text{ kJmol}^{-1}$, $T_A = 34.2 \text{ °C}$ and $\Delta H_B = 318.8 \text{ kJmol}^{-1}$, $T_B = 45.7 \text{ °C}$ as determined from the melting DSC curves of the purified LLS and LSL samples. In Figure 2-5 (A) the solid line represents the result of the fit. As can be seen, the model predicts the eutectic point, but deviates somewhat from the experimental liquidus line especially for the points in the region around x_E . This indicates that the mixing of LLS and LSL in the liquid phase deviates from ideality.

The deviation from an ideal behavior can be characterized by a non-ideality parameter, ρ , which is the energy difference between (A–B) pair and the average of (A–A) pair and (B–B) pair and is given by:

$$\rho = z \left(u_{AB} - \frac{u_{AA} + u_{BB}}{2} \right) \quad (3)$$

where z is the first coordination number and u_{AA} , u_{BB} and u_{AB} are the interaction energies for A–A, B–B, and A–B pairs, respectively. For ideal mixing, ρ is zero. Positive ρ reflects a tendency of like molecules to cluster, which beyond some critical value, ρ_c , leads to a phase separation. A negative ρ reflects a tendency for order, which in this case means the formation of AB pairs is energetically more favorable compared with AA or BB pair formation. This is the so-called Bragg-Williams approximation (Bragg, 1934), and is adequate for mixtures of components with similar molecular structure and molar volume (Moore, 1972).

This approximation attributes the origin of the non-ideality of mixing to the enthalpy term of the free energy of mixing; therefore the entropy term is the same as in the ideal mixing case. It attributes the origin of the non-ideality of mixing to the enthalpy term of the free energy of mixing, therefore, the entropy term is the same as in the ideal mixing case (Moore, 1972). Since LLS and LSL do not differ in their molecular structure and molecular volume, the Bragg-Williams approximation is appropriate for the description of the non-ideality of mixing in the liquid phase for the LLS/LSL mixture.

According to this approximation, the liquidus line in the composition range between $x_E \leq x_A \leq 1$ is given by:

$$\ln x_A + \frac{\rho(1-x_A)^2}{RT} = -\frac{\Delta H_A}{R} \left(\frac{1}{T} - \frac{1}{T_A} \right) \quad (4)$$

and in the composition range $0 \leq x_A \leq x_E$ is given by:

$$\ln x_B + \frac{\rho(1-x_B)^2}{RT} = -\frac{\Delta H_B}{R} \left(\frac{1}{T} - \frac{1}{T_B} \right) \quad (5)$$

The liquidus line for the LLS/LSL binary system was calculated using Equations 4 and 5, in which ρ was treated as an adjustable parameter. The fit (dashed line in Figure 2-5 (A)) to the experimental data was assessed by visual inspection. A small

negative value of ρ (-1.0 kJ mol^{-1}) was obtained, which suggests that in the liquid phase, the formation of a LLS-LSL pair is energetically favorable compared with that of a LLS – LLS and that of a LSL – LSL.

When we assume non-ideal mixing in both liquid and solid phases, application of the Bragg-Williams approximation is accomplished via the following expressions originally derived by Lee and co-workers (Lee, 1977):

$$\ln \frac{x_{LSL}^L}{x_{LSL}^S} + \frac{\rho_L(1-x_{LSL}^L)^2 - \rho_S(1-x_{LSL}^S)^2}{RT} = -\frac{\Delta H_{LSL}}{R} \left(\frac{1}{T} - \frac{1}{T_{LSL}} \right) \quad (6)$$

$$\ln \frac{1-x_{LSL}^L}{1-x_{LSL}^S} + \frac{\rho_L(x_{LSL}^L)^2 - \rho_S(x_{LSL}^S)^2}{RT} = -\frac{\Delta H_{LLS}}{R} \left(\frac{1}{T} - \frac{1}{T_{LLS}} \right) \quad (7)$$

where superscript L and S refer to the liquid and solid phases, respectively.

The liquidus line $x_A^L = x_A^L(T)$ and the solidus line $x_A^S = x_A^S(T)$ can be obtained by solving the simultaneous equations 6 and 7. The parameters ρ_L and ρ_S were optimized and the fitting of the calculated curve to the experimental points was judged by visual inspection. The calculated curves are represented in Figure 2-5 (B). The best fit was achieved using $\rho_L = -1.2 \text{ kJmol}^{-1}$ and $\rho_S = +3.9 \text{ kJmol}^{-1}$. The experimental liquidus and solidus lines have been most faithfully reproduced by this model.

The experimental phase diagram of LLS/LSL system is well described by the introduction of a negative value of ρ_L in the latter two models. This suggests that in the liquid phase, the LLS – LSL interaction is more attractive compared to LLS – LLS and LSL – LSL pair interactions. On the other hand, the large positive value for ρ_S strongly indicates there is a phase separation in the solid state. This point can help further explain the XRD results, as previously suggested. Based on the DSC results, the observed XRD spectra of the intermediate mixtures are likely the result of a superposition of diffractions from the two separate components (LSL and LLS) in the solid state.

Temperature-molar fraction phase diagram was also constructed for the LLS-LSL binary system processed at $3.0 \text{ }^\circ\text{C/min}$ (Figure 2-6). The peak maximum of melting was used to represent the liquidus line. One will notice that there is no solidus line present.

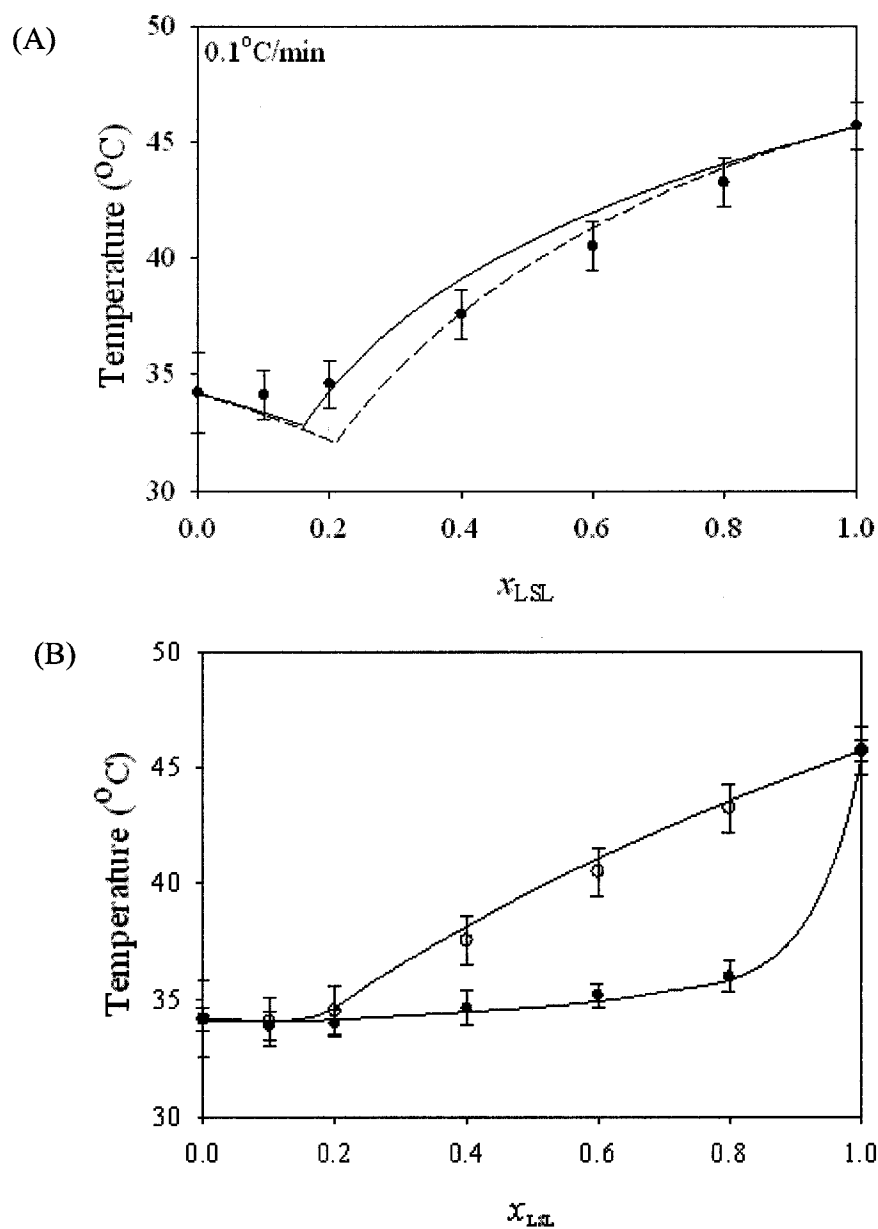


Figure 2-5. Phase diagram of the LSL/LLS binary system constructed using DSC data obtained for the samples crystallized at 0.1 °C/min. (A) Fit of the liquidus line considering an ideal solution, using equations 1 and 2 (solid line) and considering non-ideality of mixing, using equations 4 and 5 (dashed line). (B) Simultaneous fit of the liquidus and solidus lines (solid lines) considering non-ideality of mixing, using equations 6 and 7. Error bars are standard deviations, $n=3$.

Due to the extreme processing conditions (*i.e.* 3.0 °C/min) during crystallization, the system was too far from equilibrium during the crystallization process to allow for an accurate measurement of the solidus line. As can be seen in Figure 2-6, there is a clear eutectic present around $x_{\text{LSL}} = 0.2$. The shift in the eutectic is not surprising, again due to the fact that crystallization occurred far from equilibrium.

Upon fitting Equations 1 and 2 or the Bragg-Williams model (Equations 4 and 5) to the data for the liquidus line, deviations between experiment and the thermodynamic models pointed to the enthalpy of the melt (ΔH) being underestimated by the DSC; evidenced by the fact the both models predict an eutectic around $x_{\text{LSL}} = 0.2$ (Figure 2-5).

Accurate measurements of the enthalpy of the melt for individual peaks were particularly difficult for this system, most notably for the $x_{\text{LSL}} = 0.0, 0.1$ and 0.2 samples. The exothermic ordering peak following the phase transformations, previously discussed, overlaps with the successive phase transformation and final melting peak.

This overlap causes the exothermic and endothermic DSC peaks to become convoluted. Any attempt to estimate the enthalpy of the melt without deconvoluting the two peaks, as done for this study, will surely result in an under estimation of the melting enthalpy. As a result the enthalpy values used in the thermodynamic models give rise to a predicted eutectic at a higher mole fraction, $x_{\text{LSL}} = 0.2$ in this case. Given this caveat, the Bragg-Williams model does result in a negative value of ρ , which indicates that in solution the formation of LLS-LSL pairs is more favorable.

It should also be pointed out that phase diagrams constructed from DSC crystallization data, for the 3°C/min cooling rate, demonstrated the same phase behavior.

2.3.2.4. Inter-polymorphic Transformations

The identification of the polymorphs for each melting peak can only be unambiguously identified using a time resolved synchrotron x-ray diffraction technique (MacNaughtan et al., 2006). The XRD data presented earlier represents the polymorphs present prior to melting by DSC.

It indicated that for all samples at both 0.1 and 3.0 °C/min cooling rates, the LLS-LLS and LSL-LSL bilayers packed in the β' form. As can be seen in Figure 2-4 (B), an exotherm preceded the main melting peak for all mixtures cooled at 3 °C/min, an

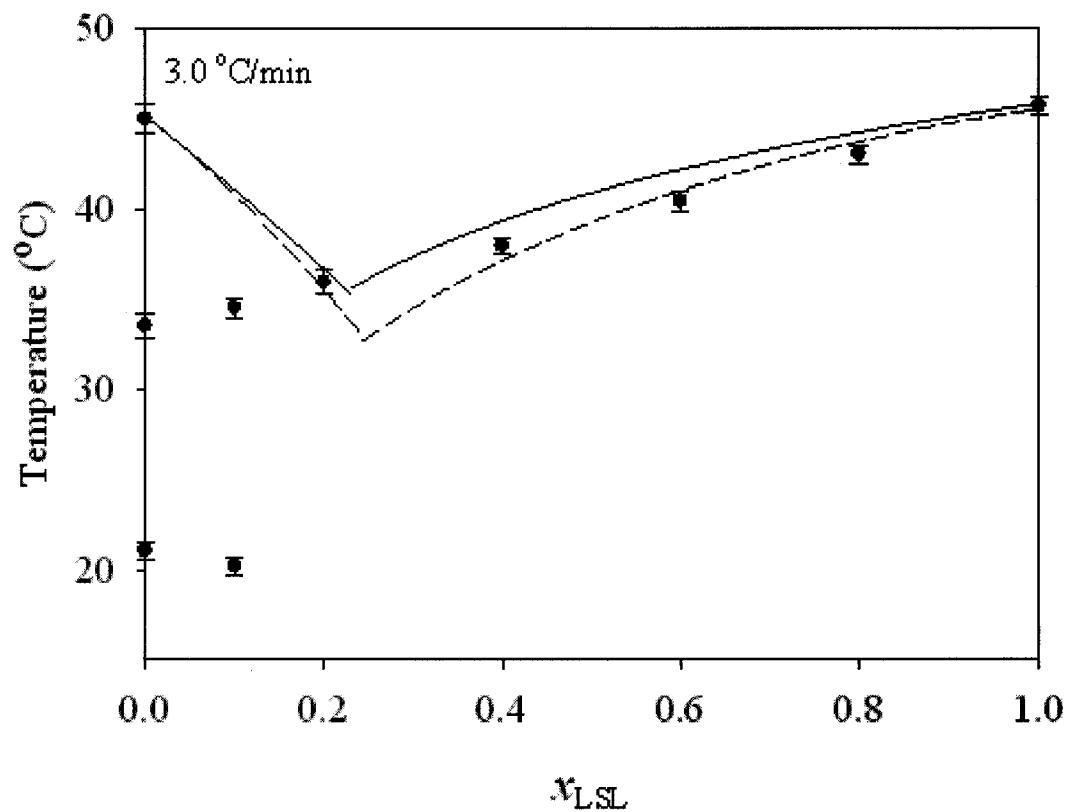


Figure 2-6. Phase diagram of the LSL/LLS binary system constructed using DSC data obtained for the samples crystallized at 3.0 °C/min. Experimental (symbols) and calculated liquidus line considering an ideal solution, using equations 1 and 2 (solid line) and considering non-ideality of mixing, using equations 4 and 5 (dashed line). Error bars are standard deviations, $n=3$.

indication that maximum order has not been achieved with this cooling rate. A temperature increase induced ordering before melting. Interestingly, for the mixtures with $x_{\text{LSL}} \leq 0.2$, the enthalpy associated with the exotherms started with relatively large values and decreased with increasing LSL content while for mixtures with $x_{\text{LSL}} > 0.2$, it was relatively small and increased with increasing LSL content. This may suggest that LSL-LSL bilayers template progressively the long range order of the LLS-LLS bilayers up to or just beyond the eutectic concentration, where no ordering was induced. After the eutectic concentration, the long range order of the extra LSL-LSL started to increase with increasing temperature before melting, the highest increase being for the pure LSL sample.

It can also be seen from the thermograms in Figure 2-4 (B), as the composition of LSL is increased, the first polymorph, P_1 , is diminished and disappeared after $x_{\text{LSL}} = 0.2$. This suggests that as the mole fraction of LSL is increased, a critical concentration of LSL is reached that completely disrupts the formation of the P_1 polymorph, which correlates well with the observation of a eutectic at around $x_{\text{LSL}} = 0.2$ for the 3.0 °C/min processing condition.

It is interesting to note that the crystallization enthalpy curves converge slightly with increasing x_{LSL} which would indicate that LSL-LSL domains required more energy to grow, when subjected to higher heating rates. This would suggest that the LSL-LSL domains were more stable at the equilibrium state than the LLS-LLS domains. The melting enthalpy curves (Figure 2-4 (C)) diverge slightly with increasing x_{LSL} which would indicate the increasing contribution of the LSL-LSL domains to the endotherm when subjected to slower heating rates. This would suggest that the LSL-LSL domains are more stable at the equilibrium state than the LLS-LLS domains.

2.3.2.5. Determination of Energy of Activation for Nucleation

The energy of activation for nucleation was estimated using an approach developed by Marangoni and co-workers (Marangoni et al., 2006a; Marangoni et al., 2006b). In this model, the normalized nucleation rate ($\frac{J}{J_{\text{max}}}$) of a fat system is related to a supercooling-time exposure parameter β , by:

$$\frac{J}{J_{\max}} = e^{-k\sqrt{\beta}} \quad (8)$$

This function is often used to model diffusion processes which take place with constant probability per unit time.

$\frac{J}{J_{\max}}$ can also be related to the cooling rate (ϕ) by:

$$\frac{J}{J_{\max}} = e^{-\frac{X}{\sqrt{\phi}}} \quad (9)$$

Where k is a constant and $\beta = \frac{1}{2} \frac{(\Delta T_{CM})^2}{\phi}$ with $\Delta T_{CM} = T_M - T_{C-start}$ being the difference between the melting (T_M) and start ($T_{C-start}$) temperatures. $T_{C-start}$ corresponds to the point where the signal deviates from the baseline. The different cooling rates (ϕ) used were 0.1, 0.5, 1.0, 1.5 and 3.0°C/min. X is a factor defined as $Q_m = Z \cdot X$ (J/g) where Q_m is the energy of activation for nucleation and $Z = \frac{C_p \sqrt{2}}{k}$ with C_p the specific heat of the solid state.

This model was justified using statistical considerations for the nucleation process. Using microscopy measurements results, Marangoni recently showed that the nucleation events take place with a constant probability per unit supercooling-time exposure (β) (Marangoni et al., 2006a). The parameter β was directly linked to the supercooling and to the induction time under nonisothermal conditions.

C_p was determined for each TAG sample from heat capacity measurements using modulated DSC. The nucleation rate was estimated from the inverse of the induction time of nucleation (t_s) (Marangoni et al., 2006a). The nucleation rate defined by $J = \frac{\phi}{\Delta T_{CM}}$ was determined from DSC measurements.

Variation and fit of the normalized nucleation rate $\frac{J}{J_{\max}}$ vs $\sqrt{\beta}$ and its variation and fit as a function of $\frac{1}{\sqrt{\phi}}$ for each sample were plotted. From the fit of these plots, k

and X were determined respectively. An example of each plot and the fit for the $x_{LSL} = 0.2$ molar composition is shown in Figure 2-7 (A) and (B). All exponential fits to experimental data were excellent. Table 2-1 lists the results (k , Z , X , and Q_m) of these fits.

The values of the energy of activation for the nucleation process in the LSL/LLS system are close to those reported by MacNaughtan for the SSS/PPP system (MacNaughtan et al., 2006). The energy of activation for nucleation varies linearly with increasing LSL molar fraction between 0.1_{LSL} and 1.0_{LSL} (Figure 2-7 (C)).

It is interesting to note that the energy of activation for nucleation is closely related to the phase behavior of the LSL/LLS binary system and mirrors the evolution of phase diagram where a eutectic has been found at molar fraction close to 0.1_{LSL} (see Figure 2-6).

2.3.3. Solid Fat Content (SFC)

The SFC (%) versus time curves, obtained at $0.1^\circ\text{C}/\text{min}$ crystallization rate, are shown in Figure 2-8 (A) and those obtained at $3.0^\circ\text{C}/\text{min}$ crystallization rate, are shown in Figure 2-8 (B). Two main segments of growth are observed; the first segment representing compositions between 0 – 25 SFC (%), and the second for compositions between 25 – 85 SFC (%), after which the SFC plateaus.

The segments described above were fitted to a modified form of the Avrami model that takes into consideration the variances within the growth curve. Table 2-2 shows the Avrami constant (A) and exponent (n) for the $0.1^\circ\text{C}/\text{min}$ crystallization rate. In the first segment of growth, the A values are almost the same $\sim 5.5 \times 10^{-8}$ and the $n \sim 2$.

In this model, the crystallization of a lipid system is regarded as a succession of p different crystallization events, occurring in steps with different incubation times τ_i . Each step i ($i = 1, 2, \dots, p$) is characterized by a constant growth rate G_i and is described by the Avrami equation:

$$F_i(t) = F_{i\infty}(1 - \exp[-A_i(t - t_i)n_i]) \quad (10)$$

where, $F_i(t)$ is the absolute crystallinity at time t , $F_{i\infty}$ is the crystallinity at some time when either the growth rate or the nucleation conditions change, t_i is the induction time

x_{LSL}	k ($K^{-1/2}s^{-1/2}$)	Z ($Jg^{-1}K^{-1/2}s^{1/2}$)	X	Q_m^* (kJ/mol)
0.0	0.09 ± 0.03	31.8 ± 1.1	0.22 ± 0.04	5.0 ± 1.2
0.1	0.10 ± 0.02	28.0 ± 1.2	0.23 ± 0.02	4.6 ± 0.6
0.2	0.07 ± 0.01	37.4 ± 1.1	0.21 ± 0.05	5.7 ± 1.2
0.4	0.06 ± 0.02	44.3 ± 1.1	0.25 ± 0.03	8.0 ± 1.2
0.6	0.05 ± 0.03	59.0 ± 1.2	0.26 ± 0.02	11.3 ± 1.4
0.8	0.04 ± 0.02	63.0 ± 1.1	0.29 ± 0.02	13.1 ± 1.2
1.0	0.04 ± 0.01	73.8 ± 1.3	0.31 ± 0.02	16.7 ± 1.6

*Molar energy of activation was calculated as $Q = Z \cdot X \cdot MW$. The average molecular weight used for LSL and LLS was 722 g/mol

Table 2-1. Exponential constants (k , Z and X) and energy of activation for nucleation (Q_m) for LSL/LLS.

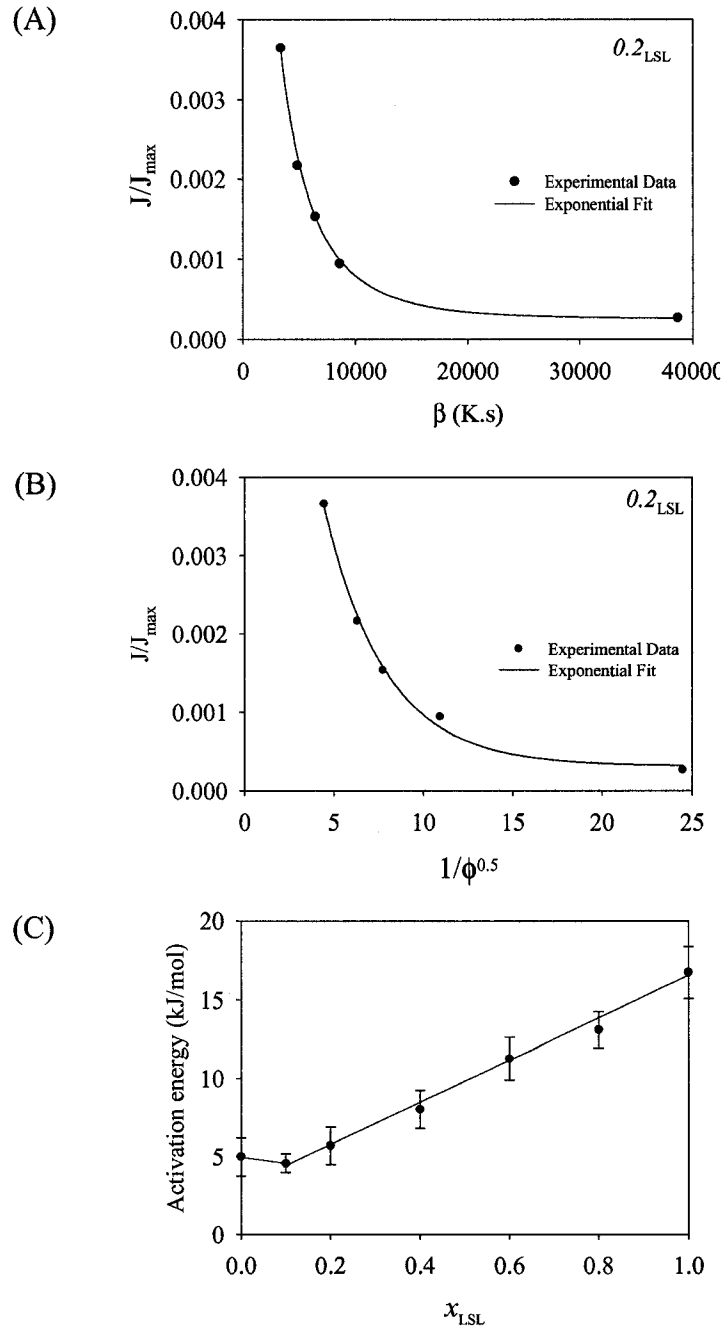


Figure 2-7. (A) Normalized nucleation rate $\frac{J}{J_{max}}$ vs. the supercooling exposure time (β) fitted to an exponential (solid line). (B) Normalized nucleation rate $\frac{J}{J_{max}}$ vs. the inverse square root of cooling rate fitted to an exponential (solid line). (C) Activation energy of nucleation vs. LSL molar composition. The solid line is a linear fit. Error bars are standard deviations, $n=3$

for crystallization of the sample, and A_i and n_i are the Avrami constant and exponent applicable to the nucleation, growth, and dimensionality of the crystallizing lipid over that segment of time.

The total absolute crystallinity is the sum of p individual absolute crystallinities (*i.e.* segments in the SFC (%) vs. time plot), as shown in Equation 11 (Narine et al., 2006).

$$F(t) = \sum_{i=1}^p F(t) \quad (11)$$

The number of crystallization segments and values of incubation times have been determined empirically using $\ln[-\ln(1-F)]$ versus $\ln(t)$ plots of experimentally determined SFC versus time data. No fitting was done for the plateau region as the SFC (%) changes are small and the system is close to being at solid – liquid equilibrium. Results are presented in Tables 2-2 and 2-3.

Table 2-2 shows the Avrami constant (A) and exponent (n) for the 0.1 °C/min crystallization rate. In the first segment of growth, the A values are almost the same $\sim 5.5 \times 10^{-8}$ and the $n \sim 2$. The Avrami constant, A , is dependent upon the nucleation rate and the growth constants, suggesting a similar nucleation rate for all samples. The exponent n is a function of the number of dimensions in which growth takes place and it reflects details about the nucleation and growth mechanism. When $n = 2$ for example, this represents a high nucleation rate with plate like growth (Sharples, 1966). In the second segment of growth, the A values were found to be larger, which corresponds to an increased rate of crystallization. The resulting n values were all approximately one.

Around the eutectic compositions, $x_{LSL} = 0.1$ and 0.2 , one can clearly see deviations from a pure one segment behavior in the plots of SFC (%) as a functions of time (Figure 2-8). These deviations represent different growth processes occurring during the crystallization as described by (Avrami, 1939). Interestingly, these deviations from pure one segment behavior are greatest around the eutectic point and subside as the concentration of LSL is increased beyond $x_{LSL} = 0.4$.

Upon close inspection of the SFC (%) versus time curves for the $x_{LSL} = 0.1$ and 0.2 samples, it appears that there are in fact three unique segments. However, due to the sampling frequency of the experiment the three distinct segments can not be discriminated in the fits to the Avrami model. Despite these limitations, it is apparent

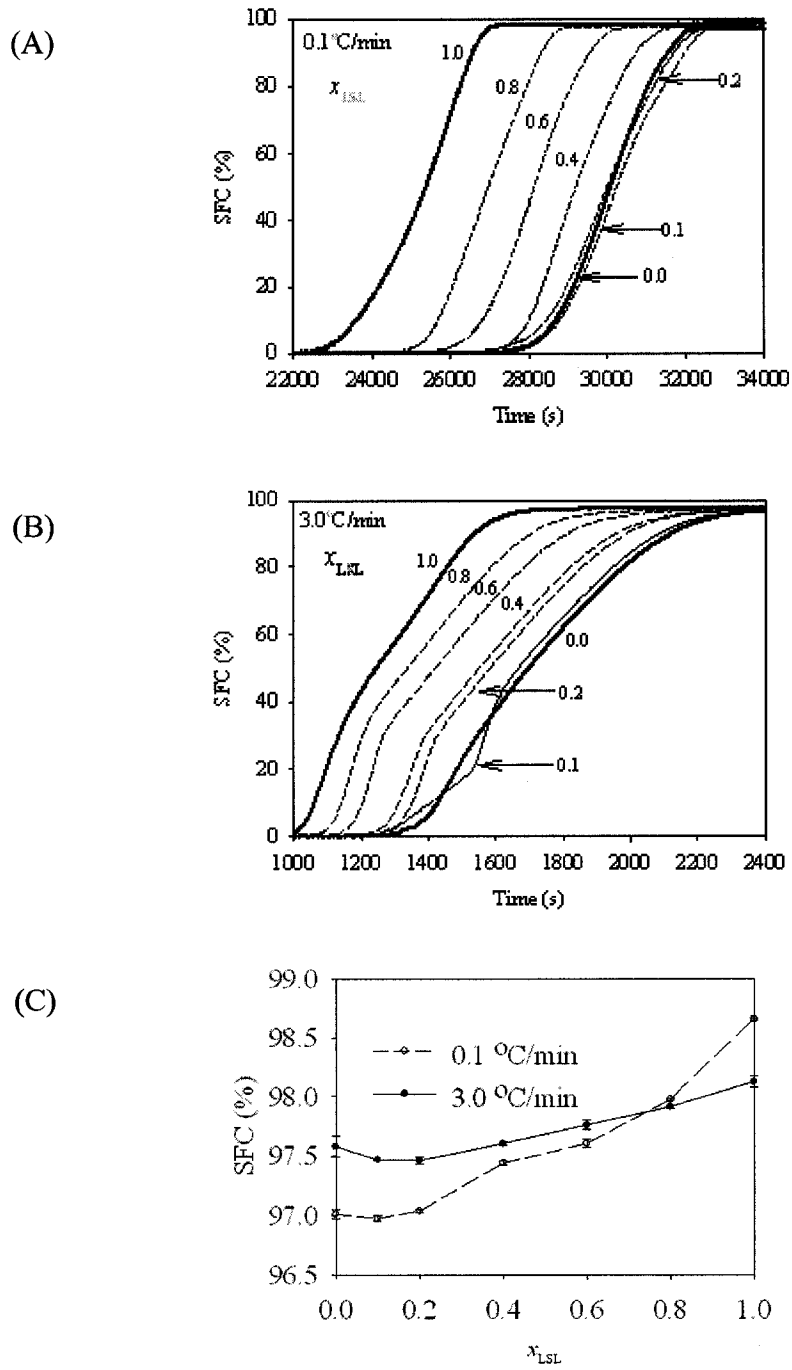


Figure 2-8. (A) SFC (%) vs. time plots for pure and binary mixtures of LSL and LLS crystallized at 0.1 °C/min, (B) SFC (%) vs. time plots for pure and binary mixtures of LSL and LLS crystallized at 3.0 °C/min, (C) Final (%) SFC vs. LSL molar composition at 0.1 and 3.0 °C/min.

Sample	Segment 1		Segment 2	
	A (1×10^{-8}) (s^{-1})	n	A (1×10^{-6}) (s^{-1})	n
0.0	5.50 ± 1.70	1.7 ± 0.1	172.9 ± 11.5	1.1 ± 0.1
0.1	5.59 ± 0.19	1.8 ± 0.2	200.6 ± 41.0	1.1 ± 0.2
0.2	4.30 ± 2.69	1.8 ± 0.1	164.1 ± 45.8	1.0 ± 0.2
0.4	5.50 ± 1.39	1.8 ± 0.1	192.6 ± 60.3	1.0 ± 0.1
0.6	5.60 ± 1.56	1.9 ± 0.2	163.4 ± 17.7	1.2 ± 0.3
0.8	5.90 ± 1.58	1.9 ± 0.2	125.3 ± 16.4	1.3 ± 0.1
1.0	6.50 ± 2.90	1.8 ± 0.3	195.5 ± 10.4	1.3 ± 0.1

Table 2-2. Avrami constant (A) and exponent (n) determined using the modified form of the Avrami equation for pure and binary mixtures of LSL and LLS crystallized at 0.1 °C/min.

Sample	Segment 1		Segment 2		Segment 3	
	A (1×10^{-6}) (s^{-1})	n	A (1×10^{-6}) (s^{-1})	n	A (1×10^{-6}) (s^{-1})	n
0.0	1.5 ± 0.3	2.1 ± 0.1	82.2 ± 2.2	1.1 ± 0.1		
0.1	1.0 ± 0.2	2.3 ± 0.1	79.4 ± 4.7	1.1 ± 0.1	128 ± 15	1.3 ± 0.1
0.2	1.2 ± 0.1	2.5 ± 0.2	89.3 ± 10.2	1.1 ± 0.2		
0.4	1.7 ± 1.6	2.1 ± 0.2	72.8 ± 9.3	1.1 ± 0.1		
0.6	1.8 ± 0.1	2.1 ± 0.2	78.8 ± 6.5	1.1 ± 0.1		
0.8	1.8 ± 0.1	2.0 ± 0.3	76.4 ± 4.7	1.2 ± 0.2		
1.0	1.8 ± 0.6	1.6 ± 0.1	94.7 ± 9.3	1.2 ± 0.1		

Table 2-3. Avrami constant (A) and exponent (n) determined using the modified form of the Avrami equation for pure and binary mixtures of LSL and LLS crystallized at 3.0 °C/min.

that the same inter-crystalline interactions of the binary mixture that gave rise to the eutectic behavior observed by DSC is causing an effect on the SFC (%).

At the 3.0 °C/min cooling rate, the SFC (%) versus time curves clearly exhibit more than one segment for all molar compositions, (see Figure 2-8 (B)). All samples display similar profiles except the $x_{LSL} = 0.0$ and 0.1 molar compositions, which is consistent with the observed eutectic from the phase diagram shown in Figure 2-5. Table 2-3 shows the Avrami constant (A) and exponent (n) for the 3.0 °C/min crystallization rate. The initial growth segments of all samples are similar ($A \sim 1 \times 10^{-6}$ s), which is two orders of magnitude greater than the corresponding segment at 0.1 °C/min ($A \sim 1 \times 10^{-8}$ s). This is not surprising as a faster crystallization rate provides a greater driving force for crystallization (Campos et al., 2002; Toro-Vazquez et al., 2000). The n values resulting from the Avrami fits for the first segment of the 3.0°C/min processed samples were similar, with all values approximately 2. In the second segment, the A values increased and the n values all ranged around 1.

Within the first segment of growth, the $x_{LSL} = 0.1$ mole fraction had two sub segments as follows; $A_1 \sim 1.0 \times 10^{-6}$ s, $n_1 = 1.3$ and $A_2 = 127.8 \times 10^{-6}$ s, $n_2 = 2.3$.

In the second SFC segment of growth for this sample the A and n values were comparable to those of the other samples. Clearly this sample undergoes an additional mode and rate of growth before achieving the plateau region. In this particular case, the third segment was sufficiently differentiated in the overall curve that the Avrami analysis was able to predict any values of meaning.

Final SFC's at this rate shows a similar depression at the $x_{LSL} = 0.1$ followed by an almost linear increase to $x_{LSL} = 1.0$. This depression of final SFC agrees with DSC which shows a lower melting polymorph for this sample (P_1 - Figure 2-2 (A)).

The unique polymorphic behavior seen in DSC was induced via melting; however this sample's crystallization behavior was also unique as observed by its SFC evolution.

2.3.4. Relative Hardness

Relative hardness measurements based on constant speed and fixed depth penetrometry measurements for 0.1 and 3.0 °C/min cooling rates are shown Figure 2-9.

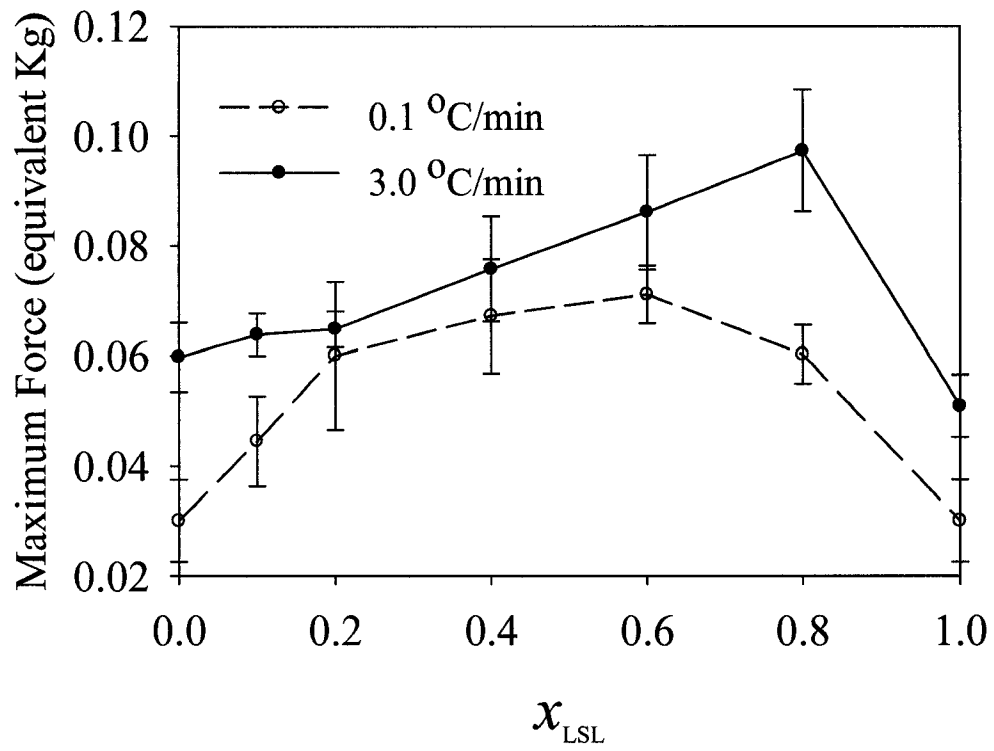


Figure 2-9. Relative hardness vs. LSL molar composition at 0.1 and 3.0 °C/min Error bars are standard deviations, n= 10

The pure samples have lower relative hardness than any mixture. At 0.1 °C/min, relative hardness increased with increasing LSL composition up to the $x_{\text{LSL}} = 0.6$ molar composition and then decreased to pure LSL. Similarly, this trend was observed at 3.0 °C/min; however the peak hardness was shifted to the $x_{\text{LSL}} = 0.8$ molar composition.

The observed trends in the hardness measurements do not directly correlate with the XRD results, peak maximum of melting and final SFC (%). However, this lack of correlation is not surprising as hardness is a macroscopic rheological property and is dependent upon inter-crystalline interactions. Conversely, XRD DSC, and SFC are more microscopic in nature, providing information on intra-crystalline interactions.

Increased hardness can result from post crystallization events such as sintering effects which take place during the plateau period of SFC evolution. Such changes can result in the strengthening of interactions between crystals which results in increased hardness. Such changes would reflect very little changes in SFC as the system is closer to a solid – liquid equilibrium state.

2.3.5. Microscopy

Micrographs (100X) for the 3.0 °C/min cooling rate are shown in Figure 2-10. The $x_{\text{LSL}} = 0.0$ and 0.2 samples have the same morphology i.e. distinct Maltese crosses which are indicative of spherulitic growth. Between these two compositions, the $x_{\text{LSL}} = 0.1$ sample displayed a very different morphology, i.e. it is more granular and lacks Maltese crosses. The $x_{\text{LSL}} = 0.4$ and 0.6 samples were similar and have numerous small granular crystallites with no Maltese crosses.

The $x_{\text{LSL}} = 0.8$ sample then deviated by having long interlocking crystallites. The pure LSL sample shared a similar morphology with $x_{\text{LSL}} = 0.8$ sample but appeared much more homogenous.

Micrographs (100X) for the 0.1 °C/min crystallization rate are shown in Figure 2-11. Larger crystallites were observed at the slower cooling rate (0.1 °C/min) (~ 25 times larger) for most compositions. A slower cooling rate would meet the thermodynamic conditions for fewer species to crystallize at a given time and as such fewer nuclei with a larger critical size will be formed.

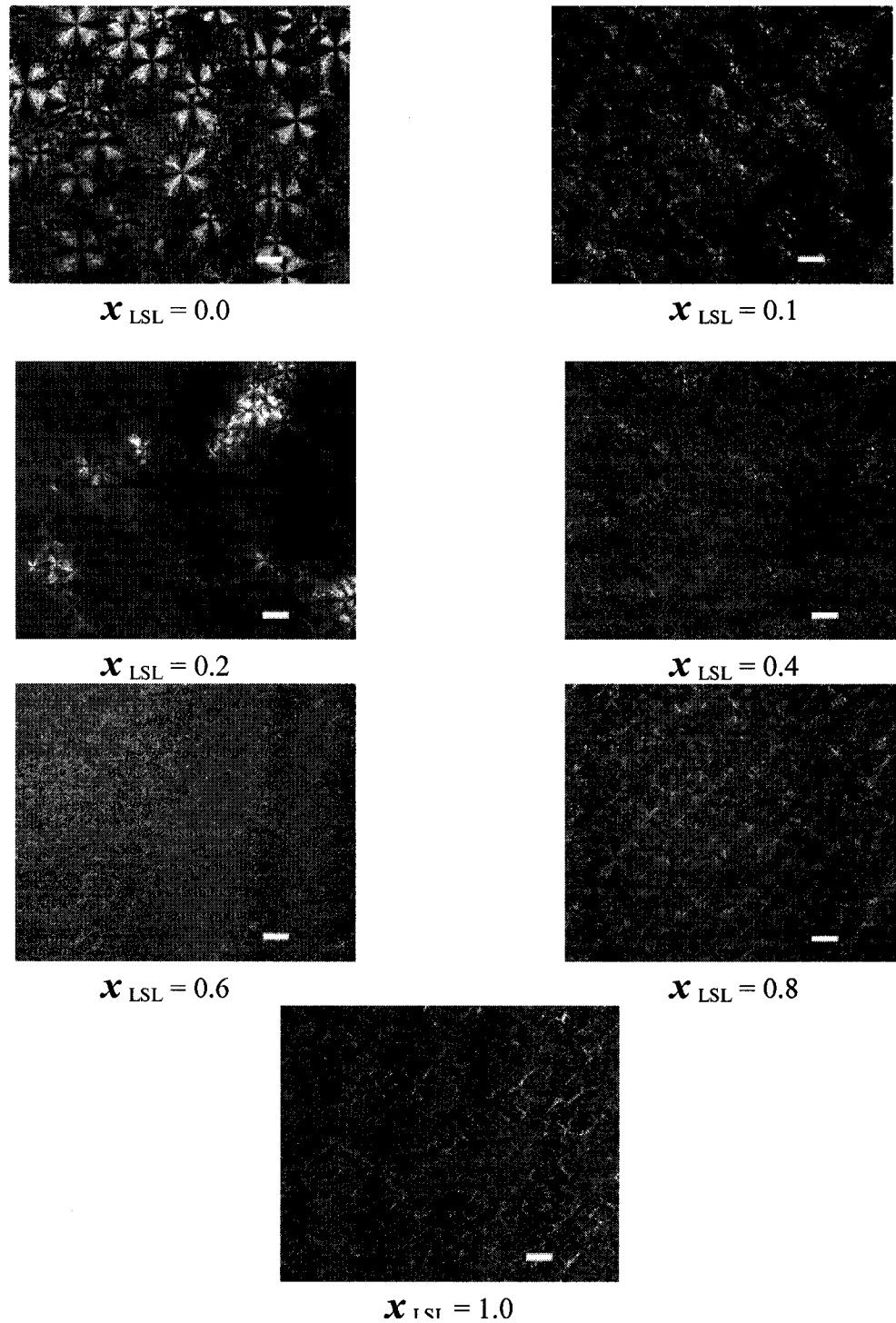


Figure 2-10. Microstructure of pure and binary mixtures of LSL and LLS crystallized at 3.0 °C/min. Magnification = 100 x. Bar =1 μm

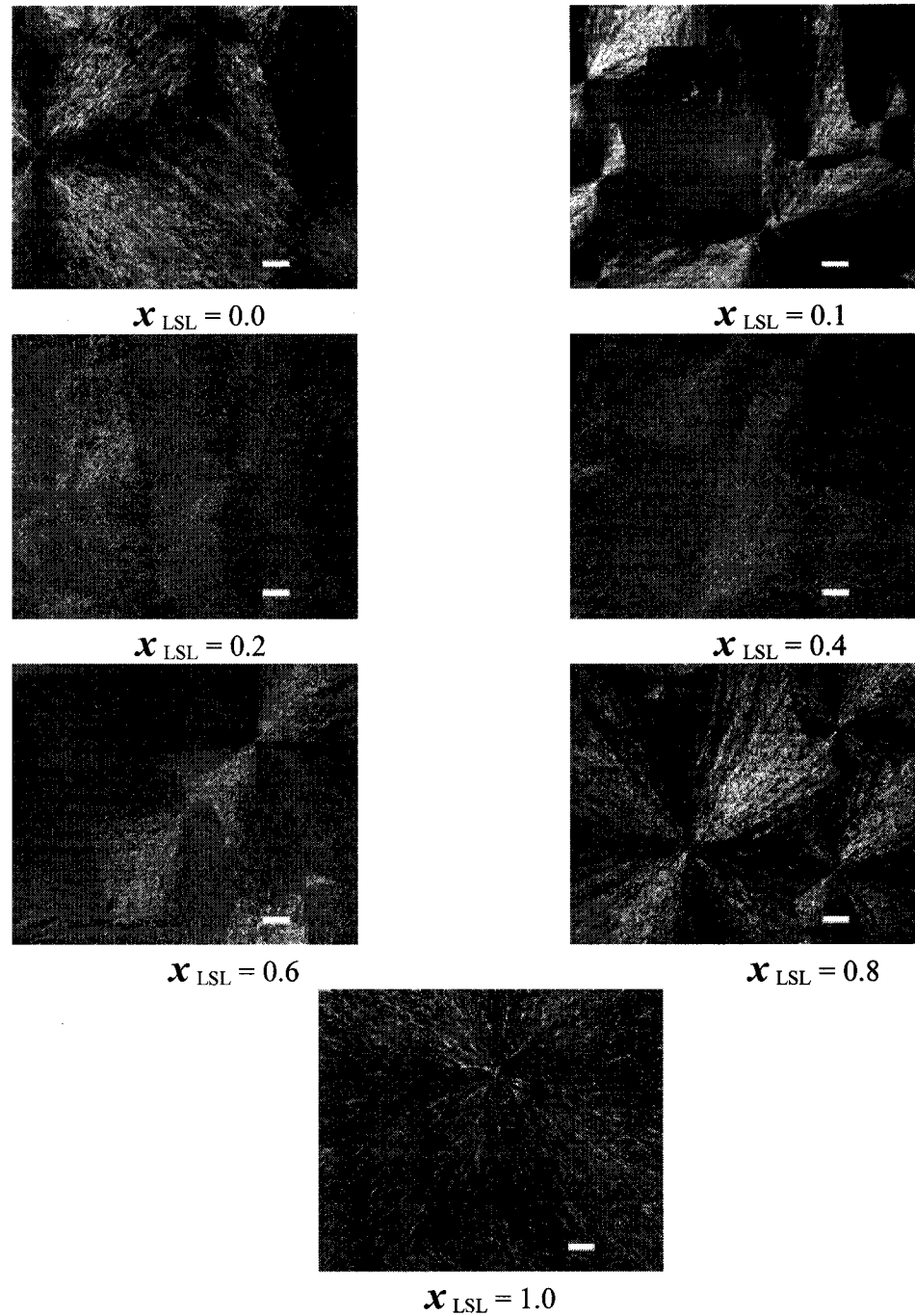


Figure 2-11. Microstructure of pure and binary mixtures of LSL and LLS crystallized at 0.1 °C/min. Magnification = 100 x. Bar =1 μm

All the samples showed a spherulitic growth and displayed large well defined crystallites with distinct Maltese crosses. In some instances a single crystallite covers the entire surface area of a microscope slide coverslip. The microstructures of $x_{\text{LSL}} = 0.2, 0.4$ and 0.6 samples were similar, with crystallites more granular in nature. The $x_{\text{LSL}} = 0.8$ sample has a similar morphology to $x_{\text{LSL}} = 0.0$ sample with sharp and prominent boundaries. The pure LSL sample displays a very large spherulitic grain without the Maltese cross showing.

2.4. Conclusion

The phase behavior of the LLS and LSL binary mixtures was determined using an array of techniques ranging from atomic level detail to macroscopic properties. The XRD spectra of the pure LLS and LSL samples indicate a β' polymorph as the final crystalline structure. From the XRD data the primitive cell could be identified as well as the bilayer length and angle of tilt. Such information not only allowed for identification of the polymorphic type, but provided sufficient detail to develop a packing model for the two pure components. For the binary mixtures, the same β' polymorph was identified as the final crystalline form. The DSC results obtained for the 0.1 °C/min cooling rate revealed a well defined eutectic around $x_{\text{LSL}} = 0.2$. Thermodynamic models of both the solidus and liquidus lines provided insight as to the nature of the phase behavior of this system. Particularly, the use of the Bragg-Williams model strongly indicates that LLS and LSL prefer to interact with one another over self interaction in solution.

These findings provide key insight into the interpretation of the XRD, as it can be inferred from the DSC data that the XRD spectra for the mixtures are merely a superposition of XRD spectra originating from domains of pure LLS and domains of pure LSL.

For the 3.0 °C/min cooling rate the DSC results were more complex. Thermodynamic models of the binary mixture, under these processing conditions, again show a eutectic. However, as the system was far from equilibrium during the crystallization process, the eutectic has shifted to around $x_{\text{LSL}} = 0.1$. Due to the overlap of endothermic and exothermic peaks in the lower LSL mole fraction samples, the thermodynamic models were not able to correctly predict this eutectic. The observation

of the solidus line could not be made, again due to the fact that the system was far from equilibrium during the crystallization process.

The SFC results clearly reveal the eutectic behavior observed by DSC for both crystallization rates. The presence of multiple segments, particularly around the eutectic, demonstrates there is a critical concentration of the LSL component that suppresses or disrupts the crystallization process. The SFC data for the samples crystallized at 3.0 °C/min exhibits an exaggerated disruption in the crystallization process at the eutectic, which is again attributed to the fact that under these processing conditions the system was far from equilibrium during the crystallization process. This same effect was observed for the 0.1 °C/min cooling rate, but was much more subtle. The results of the Avrami fitting clearly show the presence of multiple segments, indicating at least two growth modes for all crystallization rates. A third segment was found at the eutectic point, $x_{LSL} = 0.1$, for the 3.0 °C/min cooling rate.

The results of the relative hardness experiments demonstrated a progressive increase in hardness of the mixtures up to a molar composition of $x_{LSL} = 0.6$ and 0.8 for the 0.1 °C/min and 3.0 °C/min cooling rates, respectively. No direct correlations with XRD, DSC, or SFC results were observed.

The microscopy results demonstrated a spherulitic growth. Microstructure evolution was observed for both cooling rates, arriving at slightly different morphologies.

In conclusion, the phase behavior of the LSL/LLS binary system has been studied using XRD, DSC, SFC, relative hardness and microscopy. While each technique, individually, provides specific information about the molecular structure or the macroscopic morphology, the global consideration of all experimental data has led to more complete understanding of the binary phase behavior of this mixture. With this information further studies of more realistic fat models, such as ternary and quaternary mixtures, can be contemplated.

2.5. References

- Avrami, M., 1939. Kinetics of Phase Change. I. General Theory. *Journal of Chemical Physics* 7, 1103-1112.
- Bockisch, M., 1998. *Fats and Oils Handbook* AOCS Press, Champaign, Illinois, p 838.
- Bragg, W.L., Williams, E. J, 1934. The effect of thermal agitation on atomic arrangement in alloys. *Proceedings of the Royal Society of London* 145, 699-730.
- Campos, R., Narine, S.S., Marangoni, A.G., 2002. Effect of cooling rate on the structure and mechanical properties of milk fat and lard. *Food Research International* 35, 971-981.
- de Roos, N.M., Schouten, E.G., Katan, M.B., 2003. Trans fatty acids, HDL-cholesterol, and cardiovascular disease. Effects of dietary changes on vascular reactivity. *European Journal of Medical Research* 8, 355-357.
- deMan, J.M., 1992. X-ray diffraction spectroscopy in the study of fat polymorphism. *Food Research International* 25, 471-6.
- Firestone, D., 1999. *Physical and Chemical Characteristics of Oils, Fats and Waxes* AOCS Press, Champaign Illinois, pp 97-58.
- Fontell, K., 1974. X-ray diffraction by liquid crystals. In: Gray, G.W., Winsor, P.A. (Eds.), *Liquid Crystals and Plastic Crystals: Physico-chemical properties and methods of investigation*. Wiley, & Sons Inc., New York, pp. 103-152.
- Hamilton, R.J., Bhati, A., 1987. Lipid Analysis. In: *Recent Advances in Chemistry and Technology of Fats and Oils* Elsevier Applied Science, London, p 186.
- Harrison, W.A., 1980. Electronic structure and the properties of solids : the physics of the chemical bond. W. H. Freeman and Company, San Francisco, p 476.
- Hildebrand, J.H., 1929. Solubility XII Regular solutions. *Journal of the American Chemical Society* 51, 66-80.
- Humphrey, K.L., Narine, S.S., 2004. Lipid phase behavior. In: *Fat Crystal Networks* Marcel Dekker, New York, pp 83-114.

- Inoue, T., Motoda, I., Hiramatsu, N., Suzuki, M., Sato, K., 1993. Phase behavior of binary mixture of palmitoleic acid (cis-9-hexadecenoic acid) and asclepic acid (cis-11-octadecenoic acid). *Chemistry and Physics of Lipids* 66, 209-14.
- Knoster, M., DeBruijne, P., 1972. The solid-liquid equilibrium of binary mixtures of triglycerides with palmitic and stearic chains. *Chemistry and Physics of Lipids* 9, 309-319.
- Lee, A.G., 1977. Lipid phase transitions and phase diagrams. II. Mixtures involving lipids. *Biochimica et Biophysica Acta, Reviews on Biomembranes* 472, 285-344.
- List, G., Mounts, T.L., Orthoefer, F., Neff, W., 1995. Margarine and shortening oils by interesterification of liquid and trisaturated triglycerides. *Journal of American Oil Chemists' Society* 72, 379-382.
- MacNaughtan, W., Farhat, I.A., Himawan, C., Starov, V.M., Stapley, A.G.F., 2006. A differential scanning calorimetry study of the crystallization kinetics of tristearin-tripalmitin mixtures. *Journal of American Oil Chemists' Society* 83, 1-9.
- Marangoni, A.G., Aurand, T.C., Martini, S., Ollivon, M., 2006a. A probabilistic approach to model the nonisothermal nucleation of triacylglycerol melts. *Crystal Growth & Design* 6, 1199-1205.
- Marangoni, A.G., Tang, D.M., Singh, A.P., 2006b. Non-isothermal nucleation of triacylglycerol melts. *Chemical Physics Letters* 419, 259-264.
- Moore, W.J., 1972. *Physical Chemistry*, Englewood Cliffs, New Jersey, pp 229-278.
- Narine, S.S., Humphrey, K.L., Bouzidi, L., 2006. Modification of the avrami model for application to the kinetics of the melt crystallization of lipids. *Journal of American Oil Chemists' Society* 83, 913-921.
- O' Brien, R.D., 2004. *Fats and oils: formulating and processing for applications*, 2nd ed. CRC Press Boca Raton, Florida, pp 127-250.
- Pham, L.J., Casa, E.P., Gregaorio, M.A., Kwon, D.Y., 1998. Triacylglycerols and Regiospecific Fatty Acid Analyses of Phillipine Seed Oils. *Journal of American Oil Chemists' Society* 75, 807-811.

- Rossel, J.B., 1967. Phase diagrams of triglyceride systems. *Advances in Lipid Research* 5, 353-408.
- Sato, K., 1999. Solidification and phase transformation behaviour of food fats- a review. *Fett/Lipid* 101, 467-474.
- Sharples, A., 1966. Overall Kinetics of Crystallization Introduction to Polymer Crystallization. Edward Arnold, London, pp. 44-59.
- Smith, K.W., Cain, F.W., Talbot, G., 2005. Kinetic Analysis of Nonisothermal Differential Scanning Calorimetry of 1,3-Dipalmitoyl-2-oleoylglycerol. *Journal of Agricultural and Food Chemistry* 53, 3031-3040.
- Sreenivasan, B., 1978. Interesterification of Fats. *Journal of American Oil Chemists' Society* 55, 796-805.
- Tan, C.P., Man, Y.B.C., 2002. Differential scanning calorimetric analysis of palm oil, palm oil based products and coconut oil: effects of scanning rate variation. *Food Chemistry* 76, 89-102.
- Timms, R., 2003. Physical Chemistry. In: *The Confectionary Fats Handbook: Properties, Production, and Application* The Oily Press, Bridgewater, pp. 9-63.
- Timms, R.E., 1984. Phase behaviour of fats and their mixtures. *Progress in Lipid Research* 23, 1-38.
- Toro-Vazquez, J.F., Briceno-Montelongo, M., Dibildox-Alvarado, E., Charo-Alonso, M., Reyes-Hernandez, J., 2000. Crystallization kinetics of palm stearin in blends with sesame seed oil. *Journal of American Oil Chemists' Society* 77, 297-310.
- van Soest, T.C., de Jong, S., Roijers, E.C., 1990. Crystal structures and melting points of saturated triacylglycerols in the beta-3 phase. *Journal of American Oil Chemists' Society* 67, 415-423.

3. The binary phase behavior of 1, 3 – dimyristoyl-2-stearoyl-*sn*-glycerol and 1, 2 – dimyristoyl-3-stearoyl-*sn*-glycerol

3.1. Introduction

This second study, in a series of three similar studies conducted in this thesis, focuses on polymorphism, crystallization, melting and rheological properties of the MSM/MMS binary system. The industrial importance of this system is justified by the fact that TAGs containing myristic and stearic acids are likely to be particularly present in low *trans* margarine and shortening formulations utilizing fully hydrogenated fats interesterified with palm, palm kernel or coconut oils. Fully hydrogenated coconut and palm kernel oils contain 15 – 17% of myristic acid, milk fat 8 – 12% and nutmeg oil 77% (Bockisch, 1998).

Samples were processed at two extreme crystallization rates, namely 0.1 °C/min and 3.0 °C/min, in order to investigate the influence of cooling rate on the above named properties.

3.2. Materials and Methods

The pure MSM and MMS TAGs were synthesized according to known procedures (Bentley and McCrae, 1970). Purity of all samples exceeded 97.0% as determined by gas chromatography fitted with a mass spectrometer detector. MSM and MMS samples were prepared and processed in a manner identical to LSL/LLS samples detailed in Chapter 2.

A version of this chapter has been submitted for publication to Chemistry and Physics of Lipids, May 2007.

3.3. Results and Discussion

3.3.1 XRD Results

Figure 3-1 shows the XRD spectra obtained at a cooling rate of 0.1 °C/min. The lower most spectrum represents pure MMS (0.0 x_{MSM}). The stacked spectra above the pure MMS spectrum are for samples of increasing molar concentrations of MSM up to $x_{\text{MSM}} = 1.0$, which is the uppermost spectrum. The spectra were divided into two regions, both of which give information relating to the packing of the TAG molecules. These ranges are $2\theta \leq 18^\circ$ (long spacing region) and $18^\circ \leq 2\theta \leq 30^\circ$ (short spacing region).

Long spacings observed are indicative of the lamellar packing mode of the fatty acid chains within the TAG. In this region, four distinct peaks were resolved. These four peaks were further grouped into two series namely, the P series (P_1 and P_2) and P' series (P'_1 and P'_2). A corresponding notation was used to denote the d-spacings; P (d_1 , and d_2) and P' (d_1' and d_2').

Figure 3-2 (A) shows d_1 , d_1' , d_2 and d_2' long spacing as a function of MSM mole fraction, x_{MSM} . As can be seen, all long spacing values remain unchanged for all molar fractions. The ratio of the d-spacings of the two main series of peaks (i.e. d_1 : d_2 and d_1' : d_2') was found to be 2:1 which is characteristic of lamellar periodicity. Furthermore, the angle of tilt, θ of the lamellar repeat unit can be determined from the parallel spacing, d_1 , and perpendicular spacing, d_1' , by the relation $\tan(\theta) = \frac{d_1}{d_1'}$.

The angles of tilt were identical for all lamellar units in all samples ($\theta = 53 \pm 2^\circ$). Using the relation $L = \frac{d_1'}{\cos(\theta)}$, the length of the lamellar units were found to be $L = 52.15 \pm 1.5$ for pure MMS and $L = 52.15 \pm 2.0$ for pure MSM. Shown in Figure 3-2 (B) are proposed double chain length (DCL) or bilayer packing modes for (i) the pure, symmetric, MSM and (ii) pure, asymmetric, MMS samples. The bilayer lengths obtained from the proposed packing models agrees very well with bilayer lengths obtained from XRD, assuming the distance between two sp^3 carbon atoms is 1.54 Å and a tetrahedral bond angle of 109.5° (Harrison, 1980).

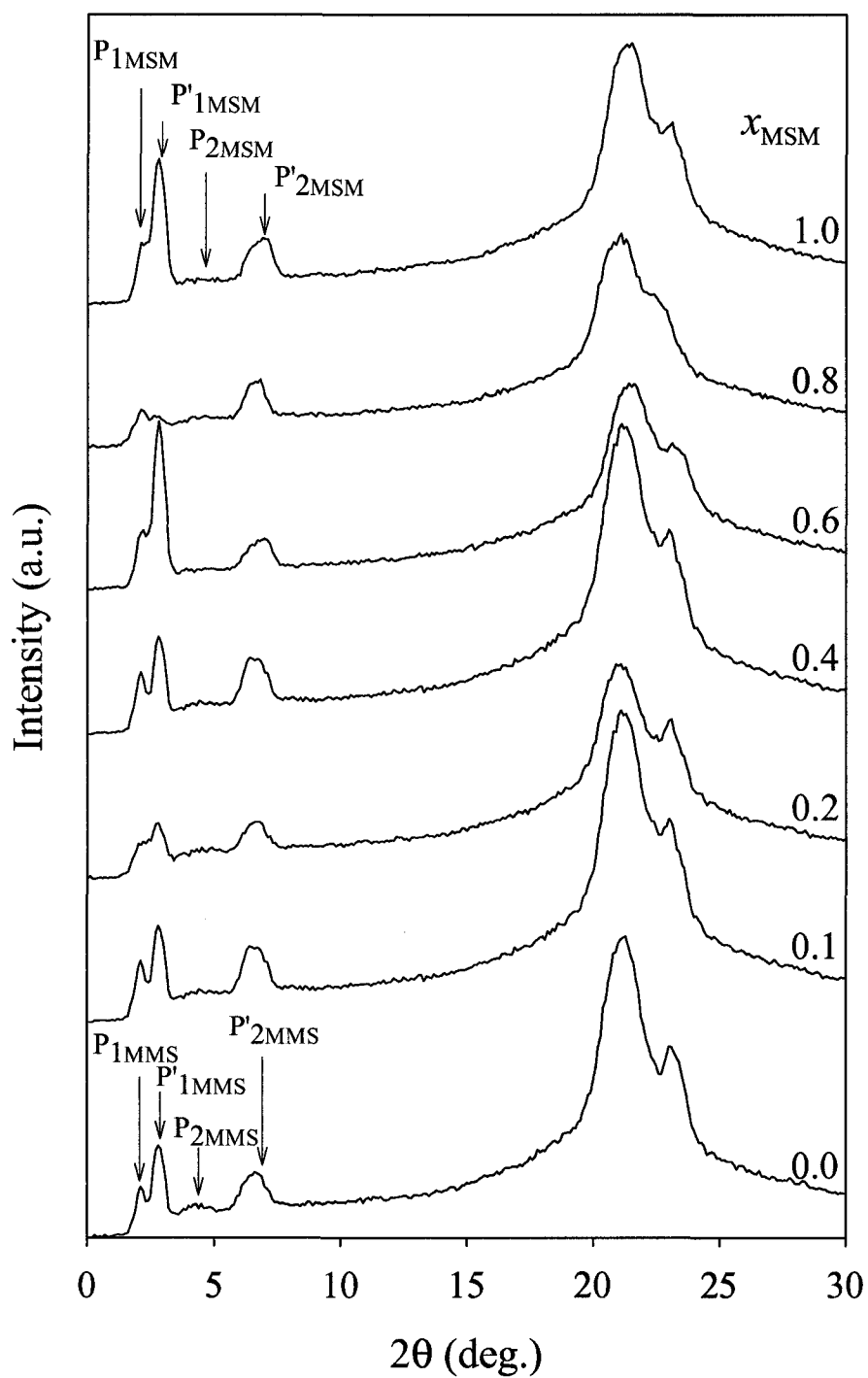


Figure 3-1. XRD spectra of MSM/MMS mixture crystallized at 0.1°C/min.

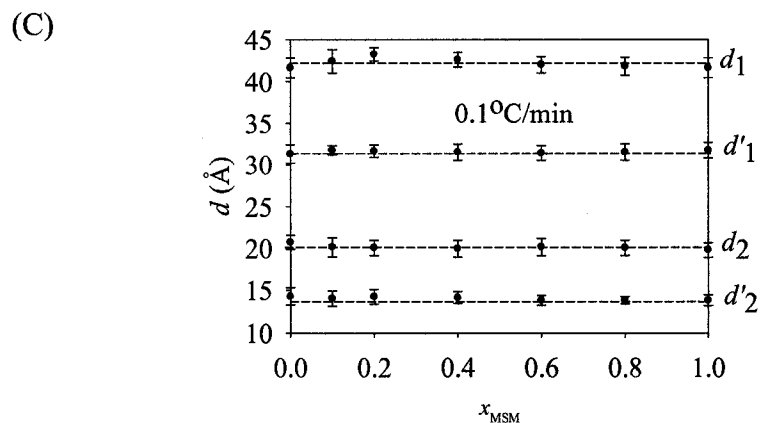
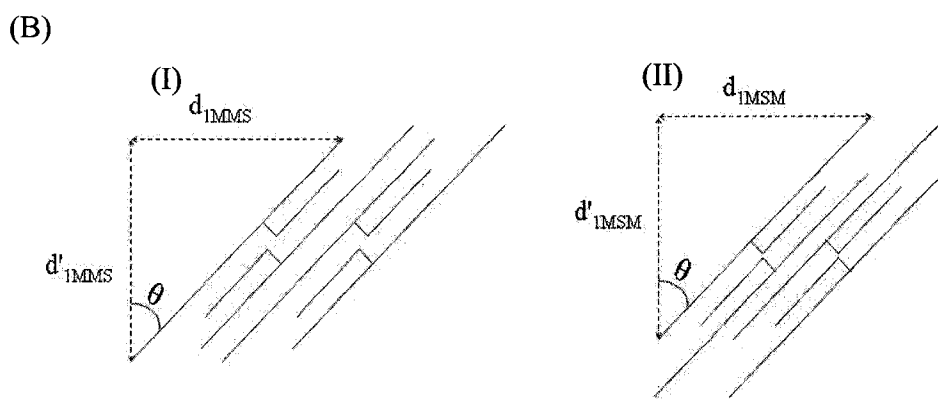
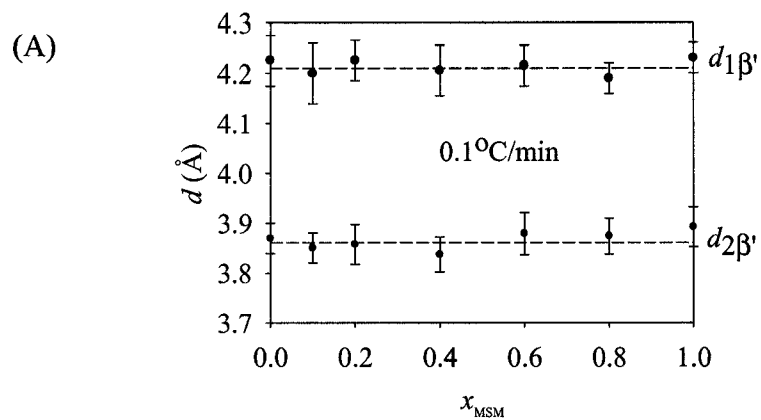


Figure 3-2. (A) Stacking mode of MSM/MMS mixtures, d_1 and d'_1 represent the parallel and perpendicular lamellar periodicities and θ is the angle of tilt, (B) Variation of d_1 , d'_1 , d_2 and d'_2 long spacing vs. the MSM molar fraction, (C) Variation of $d_{1\beta'}$ and $d_{2\beta'}$ short spacing vs. MSM molar fraction. Error bars are standard deviations, $n=3$.

The short spacings give information about the sub cell packing of the TAG molecules. In this region, the XRD spectra of the two pure TAGs have similar shapes with two well resolved peaks, each originating from the same family of plane. The short d -spacing are shown in Figure 3-2 (C). Two possible explanations can be offered for the similarity seen in all the XRD spectra obtained at the 0.1 °C/min. First scenario is the XRD spectra of the mixtures are a superposition of the XRD spectra of pure MMS and MSM. This situation would result if the two TAGs are immiscible in the solid phase. Second, the mixtures are in the same space groups as the pure MMS and MSM.

Since both MMS and MSM have similar unit cell parameters the spectra of the binary mixtures would also be similar if the two TAGs were miscible in the solid. Given the XRD data alone, neither explanation can be validated. This point will be further elaborated on in the discussion of the DSC results.

When cooled 30 times faster, the XRD peaks observed in both regions mentioned above are different. Only two peaks (P_1 and P_2) are resolved in the long spacing region and only one peak (P) is resolved in the small spacing region (Figure 3-3). They possess a similar shape and profile for samples with MSM composition lower than 0.8 and significantly different for the 0.8_{MSM} and 1.0_{MSM} molar compositions. The peaks were of similar width, but broadened significantly upon reaching the 0.8_{MSM} molar compositions. For example, the full width at half maximum (FWHM) of both the main short and long spacing region peaks observed for pure MSM were almost double of those of the pure MMS sample. For these molar compositions, the large line width could suggest the presence of convoluted peaks indicative of the presence of more than one polymorphic form and/or increased inhomogeneities and less dense crystalline packing. Despite strong suspicion that the broad peaks are made up of more than one line, we were not able, using several profile functions, to satisfactorily fit them to more than one line. This broadening introduced significant uncertainty in the analysis and attribution of the peaks.

Evolution of the long spacing values as function of MSM composition is shown in Figure 3-4 (A). The samples of up to the 0.6_{MSM} composition presented a long spacing d_1 with a constant value of 39.1 ± 1.0 Å and d_2 of 14.0 ± 0.1 Å suggesting that the

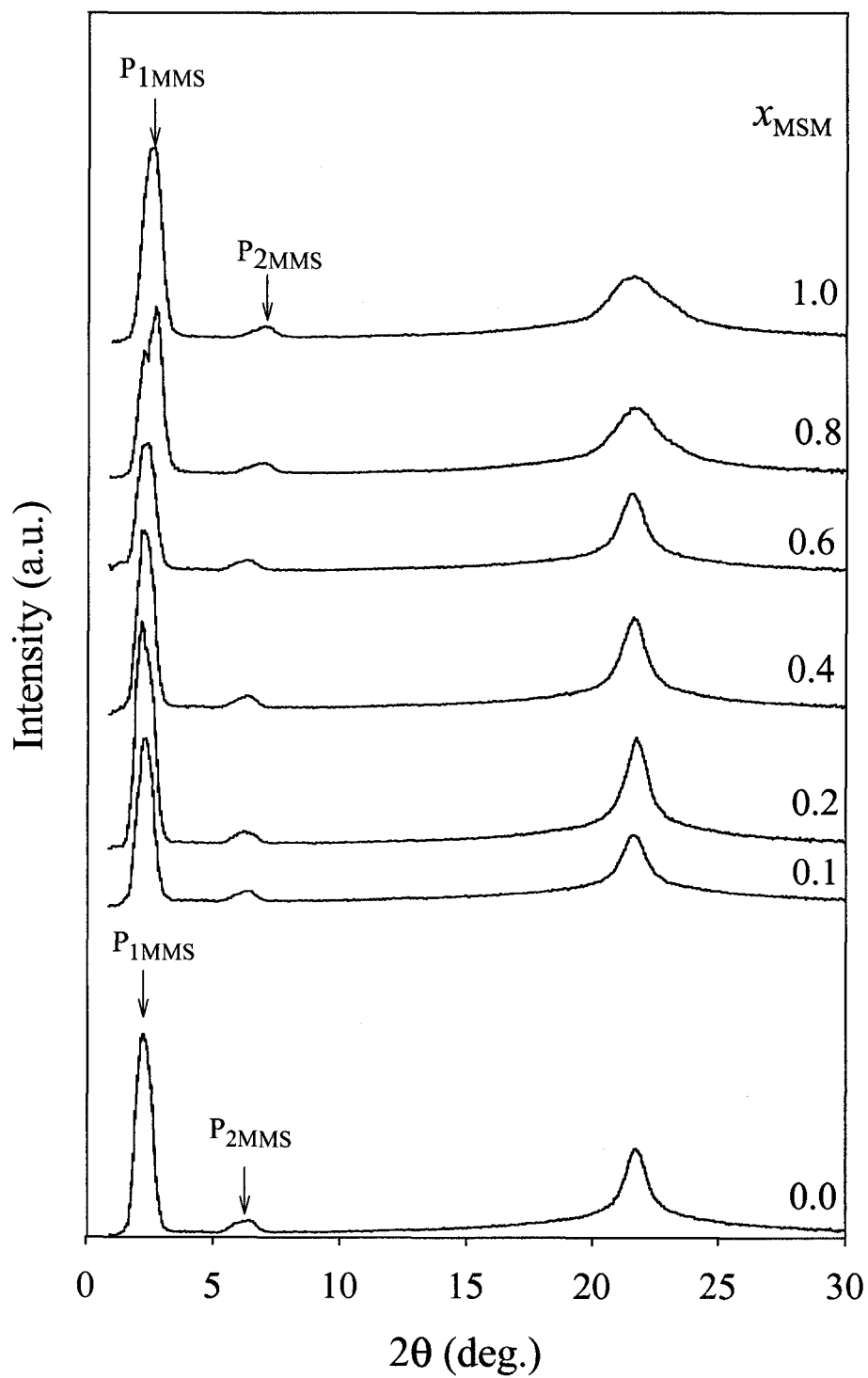


Figure 3-3. XRD spectra of MSM/MMS mixtures crystallized at 3.0 °C/min

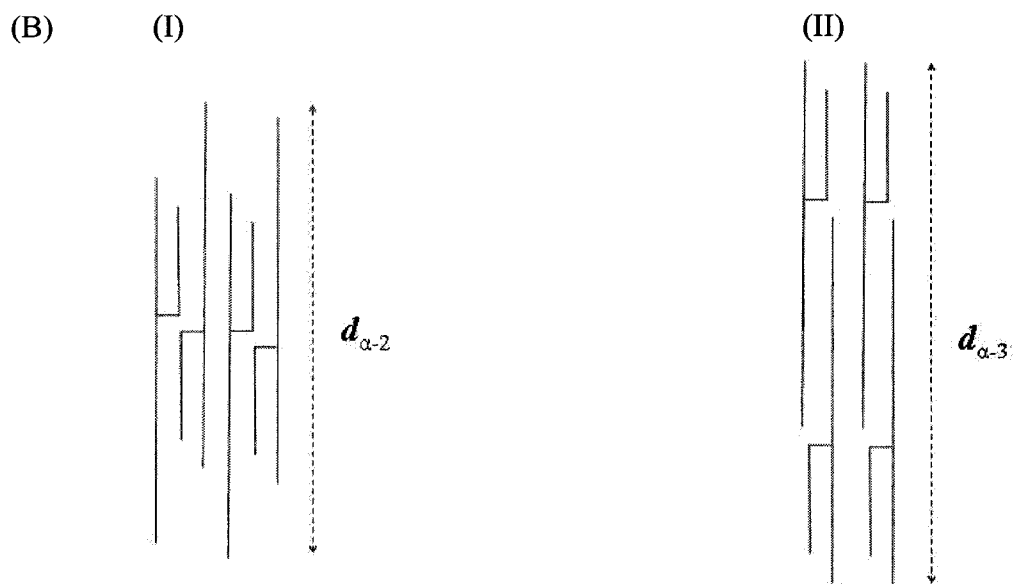
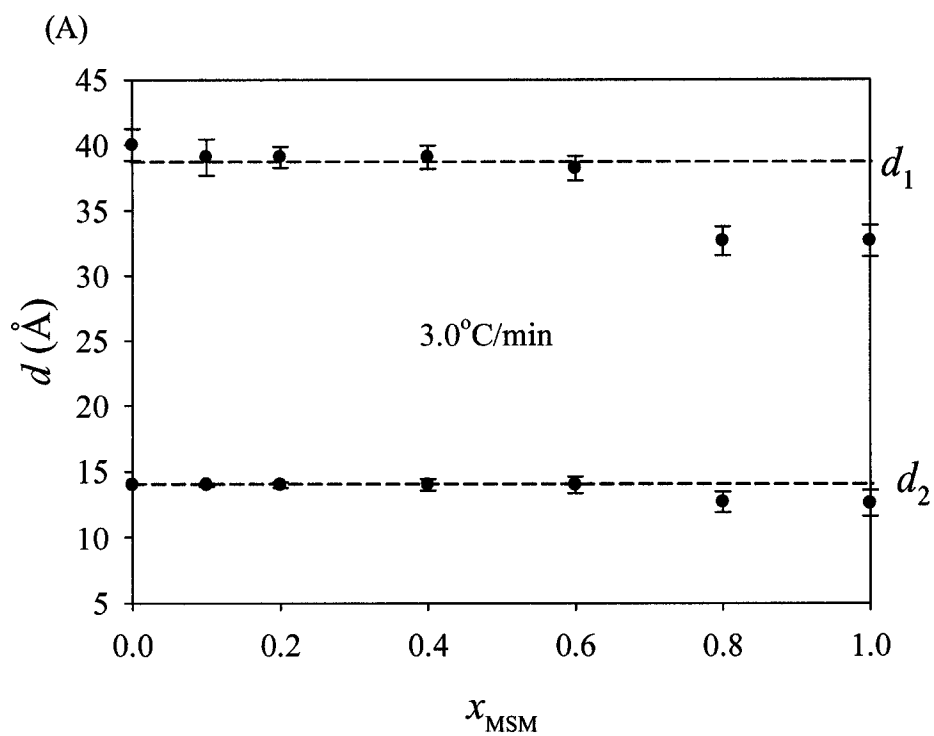


Figure 3-4. (A) Variation of long spacing as a function of the MSM molar fraction, (B) Stacking mode of MSM/MMS mixtures. Error bars are standard deviations, $n=3$.

addition of MSM does not affect lamellar packing up to the 0.6_{MSM} composition. For 0.8_{MSM} and 1.0_{MSM} mixtures, d_1 decreased to $33.0 \pm 1.0 \text{ \AA}$ and d_2 decreased to $13.0 \pm 1.0 \text{ \AA}$.

All peaks in the short spacing region have been fitted to a single line centered at the same position ($2\theta = 21.7 \pm 0.1^\circ$) corresponding to a d-spacing of $4.1 \pm 0.1 \text{ \AA}$ characteristic of an α subcell.

However, the coexistence of a β' polymorph with the α polymorph is not completely excluded in the case of the 0.8_{MSM} and pure MSM samples. DSC as well as SFC results hint to the occurrence of such a possibility as will be discussed later.

The α polymorph consists of loosely packed vertical chains (Timms, 2003). A lack of tilt should result in larger long spacing values relative to those of the β' polymorph made of the same molecules. With the α polymorph, a double chain length structure or/and a triple chain length structure could arise (these structures are shown in Figure 3-4 (B)). A simple calculation based on the MSM and MMS chain length with no tilt yields a maximum lamellar periodicity of $L \sim 57 \text{ \AA}$ for a double chain structure, and a minimum lamellar periodicity of $L \sim 72 \text{ \AA}$ for a triple chain structure. The large L values, however, would result in very small values of diffraction angle 2θ that cannot be resolved by our XRD instrument. The long spacing peaks obtained would certainly be harmonics of such fundamental peaks. Despite the absence of the fundamental peak, a packing model can be conjectured for the α polymorph.

3.3.2. DSC Results

3.3.2.1. Crystallization Behavior

Crystallization thermograms obtained at 0.1 and 3.0 °C/min are shown in Figure 3-5 (A) and (B) respectively. At 0.1 °C/min rate crystallization, multiple shoulder peaks are observed. Such peak shapes are indicative of the complexity of the crystallization process. The crystallization curves of the 0.8_{MSM} and pure MSM samples are much broader than the others. Crystallization of lipids is usually quite complex, and the overall process is likely to involve multiple chemical steps as well as multiple transport steps. Different kinetic processes can be rate limiting at different stages of a transformation.

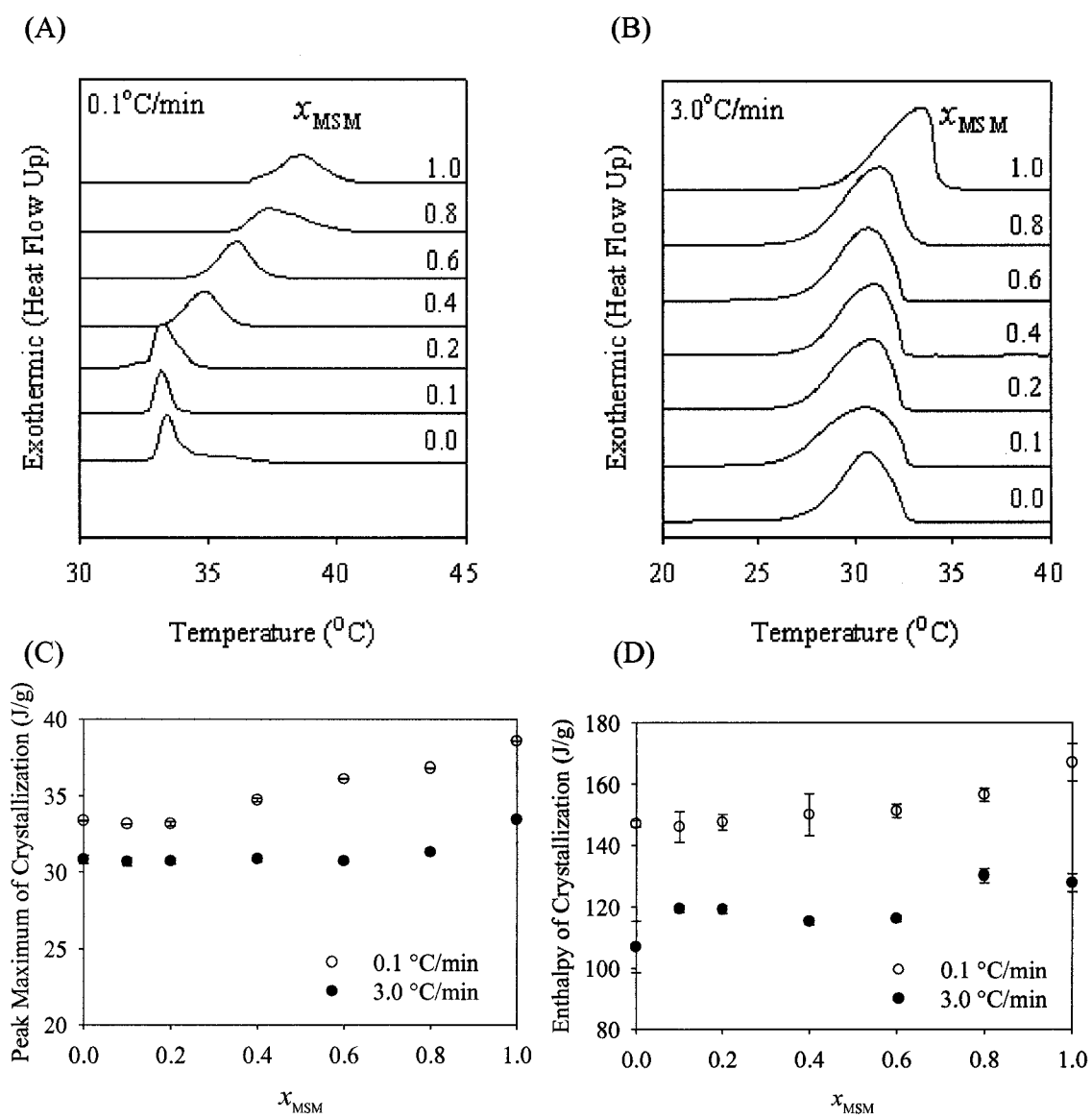


Figure 3-5. (A) Crystallization curves of MSM/MMS binary mixtures vs. MSM molar fraction at 0.1 $^{\circ}\text{C}/\text{min}$, (B) Crystallization curves of MSM/MMS binary mixtures vs. MSM molar fraction at 3.0 $^{\circ}\text{C}/\text{min}$, (C) Peak maximum of crystallization vs. of MSM molar fraction at 0.1 and 3.0 $^{\circ}\text{C}/\text{min}$, (D) Enthalpy of crystallization vs. MSM molar fraction at 0.1 and 3.0 $^{\circ}\text{C}/\text{min}$. Error bars are standard deviations, $n=3$.

Note that this interpolymorphic transformation can only be unambiguously evidenced by using time resolved synchrotron x – ray diffraction. When crystallization is carried out at the cooling rate of 3.0 °C/min, the peaks broaden, smooth and shift to lower temperatures and at the end of the crystallization process only the α polymorph was formed. At faster cooling rate less time is spent at temperatures just above the crystallization temperature and as such less lamellar organization is allowed to take place. The broadening of the crystallization peaks at a faster cooling rate is essentially due to a lower molecular packing of the crystallized ensembles at any given time.

The peak maxima of crystallization vs. x_{MSM} was larger for all samples at the 0.1 °C/min cooling rate compared to those at 3.0 °C/min cooling rate (Figure 3-5 (C)) as mentioned above. At 0.1 °C/min, peak maxima showed a eutectic behavior with a eutectic concentration of about 0.2 x_{MSM} . At 3.0 °C/min, however, the peak maxima were almost constant between 0 to 0.6 x_{MSM} followed by an increase in the maxima for higher concentrations. This suggests that at the slower cooling rate the effect of increasing MSM composition is seen at much lower compositions.

Clearly, the crystals formed at 0.1 °C/min were better packed with much stronger molecular interactions than the crystals formed at 3.0 °C/min.

Figure 3-5 (D) shows the enthalpy of crystallization as a function of x_{MSM} at 0.1 °C/min and 0.3 °C/min cooling rates. Higher crystallization enthalpies were obtained for the 0.1 °C/min cooling rate which is expected as molecular packing of the α polymorph is looser than the β' polymorph. The enthalpy of crystallization of pure MMS was lower than that of pure MSM at both cooling rates indicating that symmetric TAG pack more closely than the asymmetric TAG in both the β' and the α forms.

The effect of the addition of symmetric TAG on the enthalpy is only significant for the 0.8 and the 1.0 x_{MSM} samples which presented evidently higher crystallization enthalpies than the other samples. One can see that for all mixtures up to the 0.6 x_{MSM} , crystallization enthalpies were almost constant at both cooling rates which indicates that cooling rate does influences similarly the packing density of these mixtures.

3.3.2.2. Melting Behavior

Melting thermograms were acquired at a constant melting rate of 5.0 °C/min for samples crystallized at both 0.1 and 3.0 °C/min, Figure 3-6 (A) and (B) respectively. For the 0.1 °C/min, melting DSC showed interpolymorphic transformation for the 0.0 and 0.1 $_{\text{MSM}}$ molar compositions. The two peaks which were observed were a direct indication that a less stable polymorph (i.e. β' as evidenced by XRD) transforms via melt mediated crystallization to a thermodynamically more stable polymorph (β' or β) which finally melts. For molar composition greater than 0.2 $_{\text{MSM}}$ only a single melting peak preceded by a small exothermic shoulder is observed. This would indicate that the symmetric MSM has a greater tendency to form a more ordered β' phase shown by XRD results. This is a sign of a better chain – chain interaction and alignment of the glycerol moiety of the MSM which as in other symmetric TAGs is thought to contribute to their resistance to melt mediated transformation (Elisabettoni et al., 1998; Kellens et al., 1991).

At 3.0 °C/min however, the remelting of the α form proceeded through marked recrystallization mediated by melt into a thermodynamically more stable form (β' as discussed below) for compositions up to 0.6 $_{\text{MSM}}$. The melt mediated process was better resolved for the MMS rich phase as is evidenced by sharper endotherms and exotherms. The melting curves of the 0.8 and 1.0 $_{\text{MSM}}$ samples displayed an evident exotherm before a large melting peak. This may explain the broadening of the XRD peaks observed for these two samples.

It is possible that in mixtures where MSM predominates, a more complex phase is nucleated. The possibility of the coexistence of a predominant α form and a relatively disordered β' form is not to be excluded. The small exotherm would represent the rearrangement of the TAG molecules in the more densely packed form that melts at higher temperature. The curves of peak maximum of melting versus MSM composition for the cooling rates overlay closely (Figure 3-6 (C)) denoting the similar nature (polymorphic type) of the melted phase which is obviously the β' form. The main peak at the high temperature side shows a steady monotectic increase, while the lower melting peak, where it appeared, was almost constant.

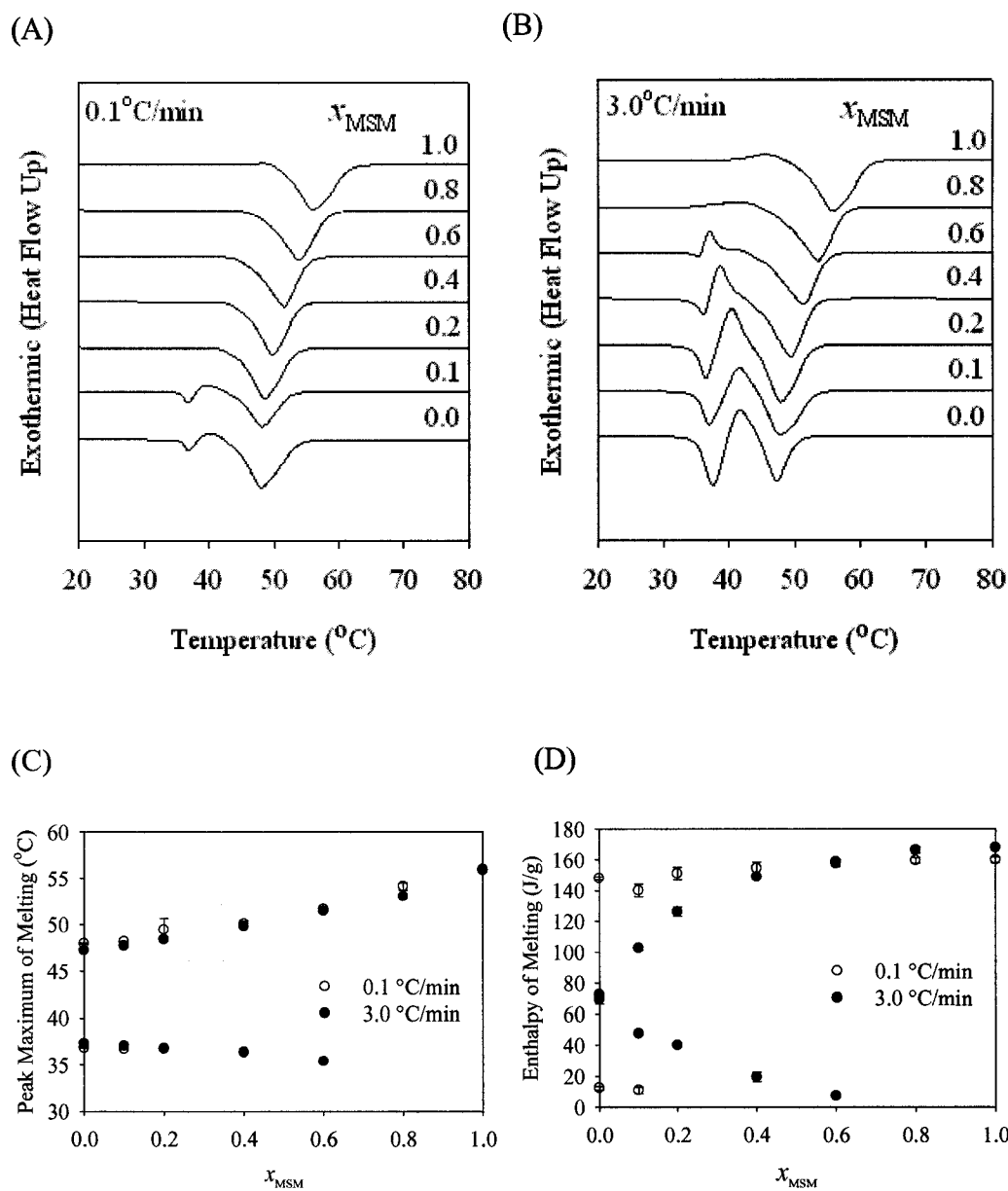


Figure 3-6. (A) Melting curves of MSM/MMS binary mixtures vs. MSM molar fraction at 0.1 °C/min, (B) Melting curves of MSM/MMS binary mixtures vs. MSM molar fraction at 3.0 °C/min, (C) Enthalpy of melting vs. of MSM molar fraction at 0.1 and 3.0 °C/min, (D) Enthalpy of melting vs. MSM molar fraction at 0.1 and 3.0 °C/min. Error bars are standard deviations, $n=3$.

Based on XRD results, the lower melting peak would safely be assigned to the α form and the higher melting peak to the β' .

The trends in melting enthalpy for the melting peaks at both rates are shown in Figure 3-6 (D). One can see that while the high melting enthalpy steadily increases (melting enthalpy of β'), the low melting enthalpy decreases (melting enthalpy of α). Regardless of the behaviors shown by the individual peaks, the total enthalpy is almost the same for all mixtures. This suggests that compounds with similar overall packing densities and molar volumes were melted. Furthermore, the cooling rate does not seem to influence very significantly the overall enthalpy of melting as the difference is about 10 J/g.

3.3.2.3. Phase Diagram of the MSM/MMS Binary System

The MMS/MSM binary phase diagram (0.1 °C/min) shown in Figure 3-7 was constructed from the melting thermograms shown in Figure 3-6. The peak maximum of melting temperature was used to represent the liquidus line and the ends of melting temperature of the said peaks were used to represent the solidus line. The phase diagram displayed a typical monotectic behavior.

The Hilderbrand model (Inoue et al., 1993; Lee, 1977) detailed in Chapter 2 (Section 2.3.2.3.) was used to simulate the phase boundary in the *Temperature–molar fraction* phase diagram. When assuming that components MMS and MSM are completely immiscible in the solid phase and behave ideally in solution, the model did not fit the experimental points. Furthermore the model predicted the formation of a eutectic point which didn't experimentally show for this system. The Bragg – Williams approximation (Moore, 1972), was applied to this system to take into account the deviation from an ideal behavior as detailed in Chapter 2. In this approximation, the non-ideality parameter, ρ , was determined which is the energy difference between (A–B) pair and the average of (A–A) pair and (B–B) pair. For ideal mixing, ρ is zero. Positive ρ reflects a tendency of like molecules to cluster, which beyond some critical value, ρ_c , leads to a phase separation. A negative ρ reflects a tendency for order, which in this case means the formation of AB pairs is energetically more favorable compared with AA or BB pair formation (Lee, 1977).

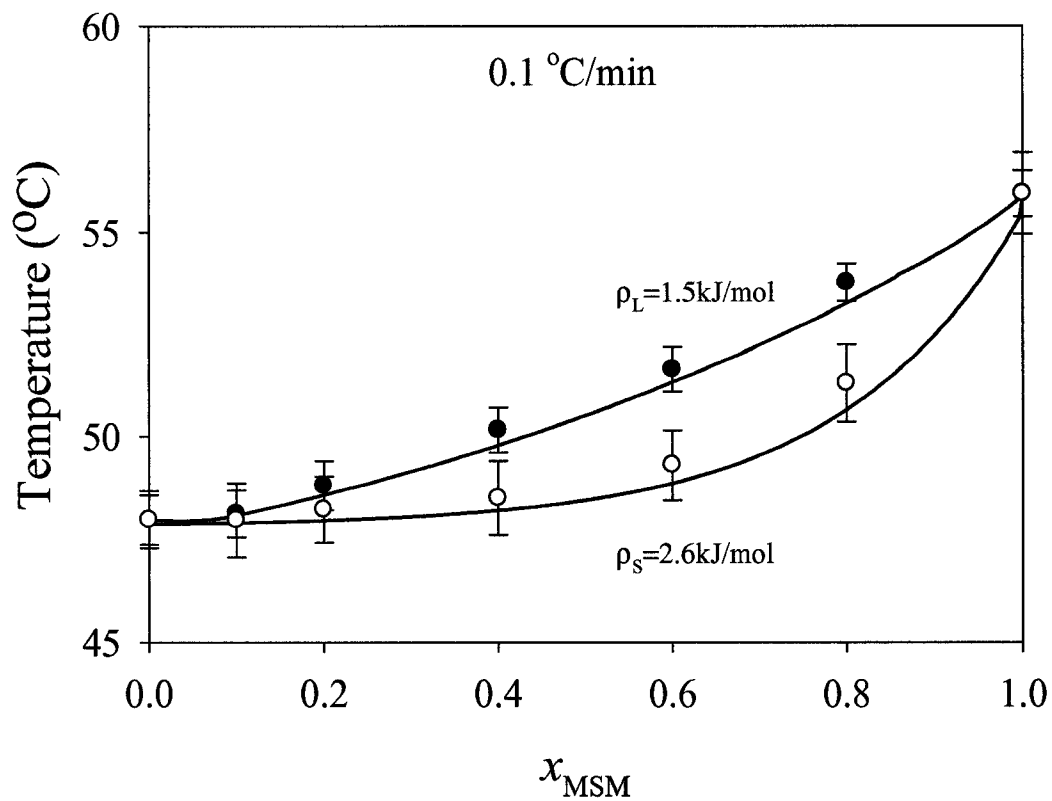


Figure 3-7. Phase diagram of the MSM/MMS binary system constructed using DSC data obtained for the samples crystallized at $0.1 \text{ }^\circ\text{C/min}$. Simultaneous fit of the liquidus and solidus lines (solid lines) considering nonideality of mixing, using equations 6 and 7. Error bars are standard deviations, $n=3$.

The liquidus line $x_A^L = x_A^L(T)$ and the solidus line $x_A^S = x_A^S(T)$ have been obtained by solving the simultaneous equations 2 and 3 (Chapter 2). The parameters ρ_L and ρ_S were optimized and the fitting of the calculated curve to the experimental points was judged by visual inspection. The calculated curves for the 0.1 °C/min rate are represented in Figure 3-7. The best fit was achieved using $\rho_L = +1.5 \text{ kJmol}^{-1}$ and $\rho_S = +2.6 \text{ kJmol}^{-1}$. The monotectic behavior of the phase diagram has been clearly reproduced by the fit.

The introduction of positive values for both ρ_L and ρ_S suggests that in both the solid and liquid phases, the MSM–MMS attraction is less favored than the MSM–MSM and MMS–MMS attractions. In this system the solidus line is almost horizontal between 0.0 to 0.6 $_{\text{MSM}}$, indicating the occurrence of phase separation. The positive value of ρ_S is large enough to explain such phase separation.

The phase diagram constructed for the 3.0 °C/min cooling rate was similar to the phase diagram constructed for the 0.1 °C/min cooling rate and thus is not shown. This similarity is consistent with the close overlay of points seen for the peak maximum of melting vs. MSM composition.

The ambiguity in the attribution using XRD results of definite molecular stacking can be overcome in light of the thermodynamic results. We can safely state that the resulting polymorphs (β' in the case of 0.1 °C/min and α in the case of 3.0 °C/min cooling rates) were predominantly constituted of MSM–MSM and MMS–MMS bilayers.

3.3.2.4. Determination of Energy of Activation for Nucleation

Activation energies of nucleation were calculated as outlined in Chapter 2. Variation and fit of the normalized nucleation rate $\frac{J}{J_{\text{max}}}$ vs $\sqrt{\beta}$ and its variation and fit as a function of $\frac{1}{\sqrt{\phi}}$ for each sample were plotted (Figure 3-8). From the fit of these plots, k and X were determined respectively. All exponential fits to experimental data were excellent. Table 3-1 lists the results (k , Z , X , and Q_m) of these fits.

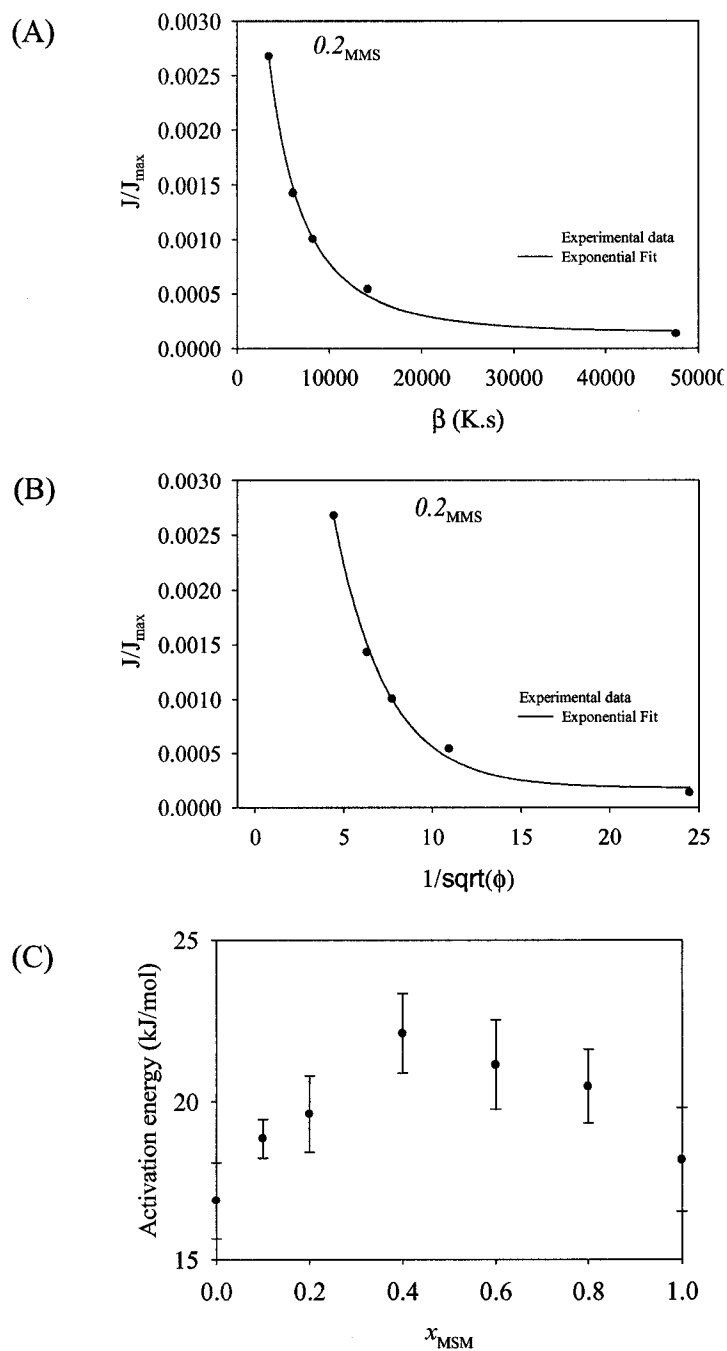


Figure 3-8. (A) Normalized nucleation rate $\frac{J}{J_{max}}$ vs. the supercooling exposure time (β) fitted to an exponential (solid line). (B) Normalized nucleation rate $\frac{J}{J_{max}}$ vs. the inverse square root of cooling rate fitted to an exponential (solid line). (C) Activation energy of nucleation vs. MSM molar composition.

x_{MSM}	k ($K^{-1/2}s^{-1/2}$)	Z ($Jg^{-1}K^{-1/2}s^{1/2}$)	X	Q_m^* (kJ/mol)
0.0	0.04 ± 0.03	65.9 ± 1.1	0.35 ± 0.04	16.9 ± 1.6
0.1	0.04 ± 0.02	71.8 ± 1.2	0.36 ± 0.02	18.8 ± 0.6
0.2	0.04 ± 0.01	74.8 ± 1.1	0.36 ± 0.05	19.6 ± 1.2
0.4	0.03 ± 0.02	83.2 ± 1.1	0.37 ± 0.03	22.2 ± 1.2
0.6	0.03 ± 0.03	83.2 ± 1.2	0.35 ± 0.02	21.1 ± 1.3
0.8	0.03 ± 0.02	84.0 ± 1.1	0.34 ± 0.02	20.5 ± 1.8
1.0	0.04 ± 0.01	80.8 ± 1.3	0.31 ± 0.02	18.2 ± 1.6

*Molar energy of activation was calculated as $Q = Z \cdot X \cdot MW$. The average molecular weight used for MSM and MMS was 780 g/mol

Table 3-1. Exponential constants (k, Z and X) and energy of activation for nucleation (Q_m) for MSM/MMS.

The values of the energy of activation for the nucleation process in the MSM/MMS system are close to those reported for the SSS/PPP system (MacNaughtan et al., 2006). The energy of activation (see Figure 3-8) for nucleation is significantly the same for the pure samples and increases almost symmetrically towards the 0.5_{MSM} sample. There is obviously a greater tendency for “ease of” nucleation in samples where one species predominate and as one evaluates samples with more equal composition, nucleation is complicated by steric factors. The concept of a free energy barrier can be assigned for nucleation and growth events. It should be noted however, that activation energies calculated by methods such as those used in this publication are obtained from experiments such as non isothermal DSC and other techniques (Vyazovkin and Wight, 1997) which do not provide complete isolation of individual crystallization events. Therefore, the calculated activation energy Q_m is a global value which incorporates the activation energies of multiple events. As a result, it is possible that our interpretation of activation energies in this argument is due to multiple crystallization and nucleation events in each sample. However, the argument of “ease of” nucleation is not modified if that is indeed the case.

3.3.3. Solid Fat Content (SFC)

The SFC (%) versus time curves, obtained at 0.1°C/min crystallization rate, is shown in Figure 3-9 (A) and those obtained at 3.0 °C/min crystallization rate, is shown in Figure 3-9 (B). An obvious main break was observed in all the curves indicating the occurrence of a second step of growth corresponding to a different reaction process. They represent (steps of growth) occurring during the crystallization which can individually be described by the Avrami model (Avrami, 1939). A closer inspection of the SFC (%) curves, particularly for the 0.0 and 0.1_{MSM} molar compositions, would reveal more details, however due to the sampling frequency of the experiment only two distinct segments can be discriminated.

The SFC (%) segments representing the steps of crystallization were fitted to a modified form of the Avrami model that takes into consideration the variances within the growth curve as detailed in Chapter 2.

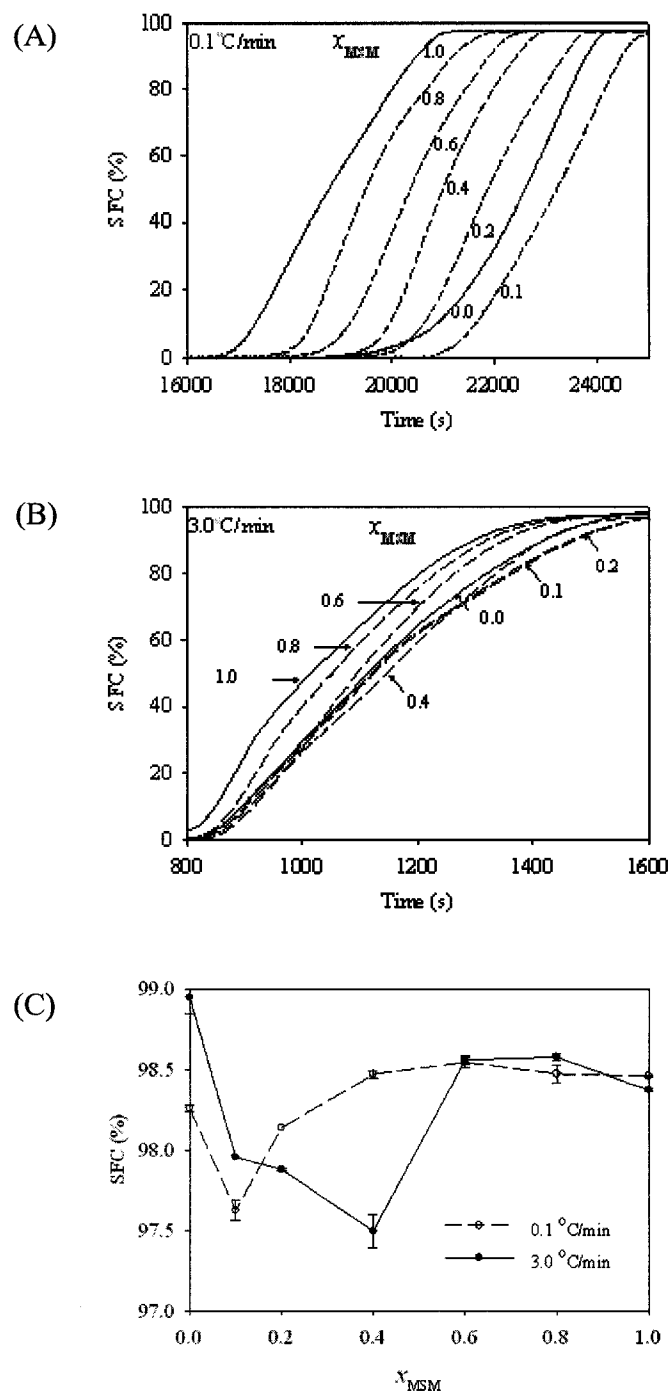


Figure 3-9. (A) SFC (%) vs. time plots for pure and binary mixtures of MSM and MMS at 0.1 °C/min, (B) SFC (%) vs. time plots for pure and binary mixtures of MSM and MMS at 3.0 °C/min, (C) Final (%) SFC vs. MSM molar composition at 0.1 and 3.0 °C/min. Error bars are standard deviations, n=3.

Table 3-2 shows the Avrami constant (A) and exponent (n) for the 0.1 °C/min crystallization rate. In the first segment of growth (Figure 3-9 (A)), the A values are almost the same $A \sim 3.8 \times 10^{-9}$ and $n \sim 2$ for all samples except 0.0 and 0.1 _{MSM} for which $n \sim 1$. The Avrami constant, A, is dependent upon the nucleation rate and the growth constants, suggesting a similar nucleation rate for all samples. The exponent n is a function of the number of dimensions in which growth takes place and it reflects details about the nucleation and growth mechanism. When $n = 2$ for example, this represents a high nucleation rate with plate-like growth (Sharples, 1966). In the second segment of growth, the A values were found to be an order of magnitude larger ($\sim 1 \times 10^{-5}$), which corresponds to an increased rate of crystallization. The n value was approximately 1 for this segment.

When the sample crystallized at 3.0 °C/min cooling rate, the SFC (%) versus time curves exhibited more than one segment for all molar compositions, (see Figure 3-9 (B)). All samples display similar profiles with differing slopes. Even if the curves of the 0.0 to 0.6 _{MSM} molar compositions intersect at several points, the overall shape is the same for all mixtures. It is therefore not surprising that the Avrami analysis provided similar results for all the mixtures. Table 3-3 shows the Avrami constant (A) and exponent (n) for the 3.0 °C/min crystallization rate. The initial growth segments of all samples are similar ($A \sim 1 \times 10^{-5}$), which is four orders of magnitude greater than the corresponding segment at 0.1 °C/min ($A \sim 1 \times 10^{-9}$). This is not surprising as a faster crystallization rate provides a greater driving force for crystallization (Campos et al., 2002; Toro-Vazquez et al., 2000). The n values resulting from the Avrami fits for the first segment of the 3.0°C/min processed samples were similar, with all values being approximately 1.5. In the second segment, the A values increased ($A \sim 1 \times 10^{-3}$) and the n values all ranged around 1.

The final SFC (%) for both crystallization rates shows values which are below the final SFC (%) of pure MMS and MSM (Figure 3-9 (C)). When crystallizing at 0.1 °C/min rate, the asymmetric TAG, MMS achieved almost the same SFC than the symmetrical MSM. However, a strong depression occurred for the 0.1 _{MSM} sample followed by a weaker depression at 0.2 _{MSM}.

Sample	Segment 1		Segment 2	
	A (1×10^{-9})	n	A (1×10^{-5})	n
0.0	3.63 ± 1.70	1.0 ± 0.1	1.92 ± 2.72	1.1 ± 0.1
0.1	3.63 ± 1.71	1.3 ± 0.2	2.02 ± 1.34	1.1 ± 0.2
0.2	4.65 ± 1.00	2.0 ± 0.31	17.64 ± 1.66	1.0 ± 0.2
0.4	4.50 ± 1.57	2.2 ± 0.1	32.20 ± 2.24	1.0 ± 0.1
0.6	3.10 ± 1.45	2.1 ± 0.1	30.20 ± 1.66	1.1 ± 0.2
0.8	3.60 ± 1.71	2.4 ± 0.1	24.37 ± 1.34	1.1 ± 0.1
1.0	3.63 ± 1.81	1.7 ± 0.3	6.44 ± 1.10	1.1 ± 0.1

Table 3-2. Avrami constant (A) and exponent (n) determined for pure and binary mixtures of MSM/MMS using the modified form of the Avrami for samples crystallized at 0.1 °C/min.

Sample	Segment 1		Segment 2	
	A (1×10^{-9})	n	A (1×10^{-3})	n
0.0	1.25 ± 1.76	1.3 ± 0.1	1.11 ± 2.2	1.1 ± 0.1
0.1	1.64 ± 0.71	1.3 ± 0.1	1.78 ± 4.7	1.1 ± 0.1
0.2	2.17 ± 0.51	1.2 ± 0.2	2.45 ± 10.2	1.1 ± 0.2
0.4	2.76 ± 0.16	1.3 ± 0.2	2.27 ± 9.3	1.1 ± 0.1
0.6	2.57 ± 0.18	1.3 ± 0.2	1.86 ± 6.5	1.1 ± 0.1
0.8	2.71 ± 0.57	1.7 ± 0.3	1.54 ± 4.7	1.2 ± 0.2
1.0	2.50 ± 0.56	1.7 ± 0.1	1.45 ± 9.3	1.2 ± 0.1

Table 3-3. Avrami constant (A) and exponent (n) determined for pure and binary mixtures of MSM/MMS using the modified form of the Avrami equation for samples crystallized at 3.0 °C/min.

The asymmetric TAG, MMS, achieved a higher SFC than the symmetrical MSM when the crystallization was carried out at 3.0 °C/min and the occurrence of depressions in final SFC extended to the 0.4_{MSM} sample (Figure 3-3 (C)). Both 0.1 and 0.2_{MSM} samples presented an SFC value below those of the pure constituents albeit the strongest depression was detected for the 0.4_{MSM}.

Above the molar composition corresponding to the strongest depression, the suppression in solid formation is alleviated and the final SFC (%) plateaus to that of the pure MSM sample, which remained almost the same for both crystallization rates. This limitation or barrier to the formation of solid content could be explained by simple equilibrium considerations. At a faster rate, more liquid is trapped between the two components (MMS and MSM domains) this effect being greater when samples are MSM richer. It seems like it is the MSM domains that mainly hold the liquid portion. The depressions in SFC (%) were not mirrored in the phase diagram (monotectic) which was constructed using DSC data. Such correlations are however not surprising, as it is entirely conceivable that the lower or higher melting polymorphs do not necessarily account for a proportionate amount of the final SFC (%). Furthermore, given the sample mass and the manner in which the SFC samples were crystallized, no melt mediated transformations would have occurred. It should be noted, however, that the differences observed in the final SFC (%) over the entire range of compositions is in the order of less than 2%, which is borderline significant. We will therefore limit our interpretation of the final SFC (%) based solely on this data.

3.3.4. Relative Hardness

Relative hardness measurements based on constant speed and fixed depth penetrometry measurements for 0.1 and 3.0 °C/min cooling rates are shown Figure 3-10. When crystallized at 3.0 °C/min cooling rate, the relative hardness didn't significantly change for all samples. The 0.0 and 0.1_{MSM} samples displayed the same relative hardness for both rates at the 0.1 °C/min cooling rate, the relative hardness almost doubled for the 0.2_{MSM} and plateaued. This trend does not correlate with the depressions seen in SFC.

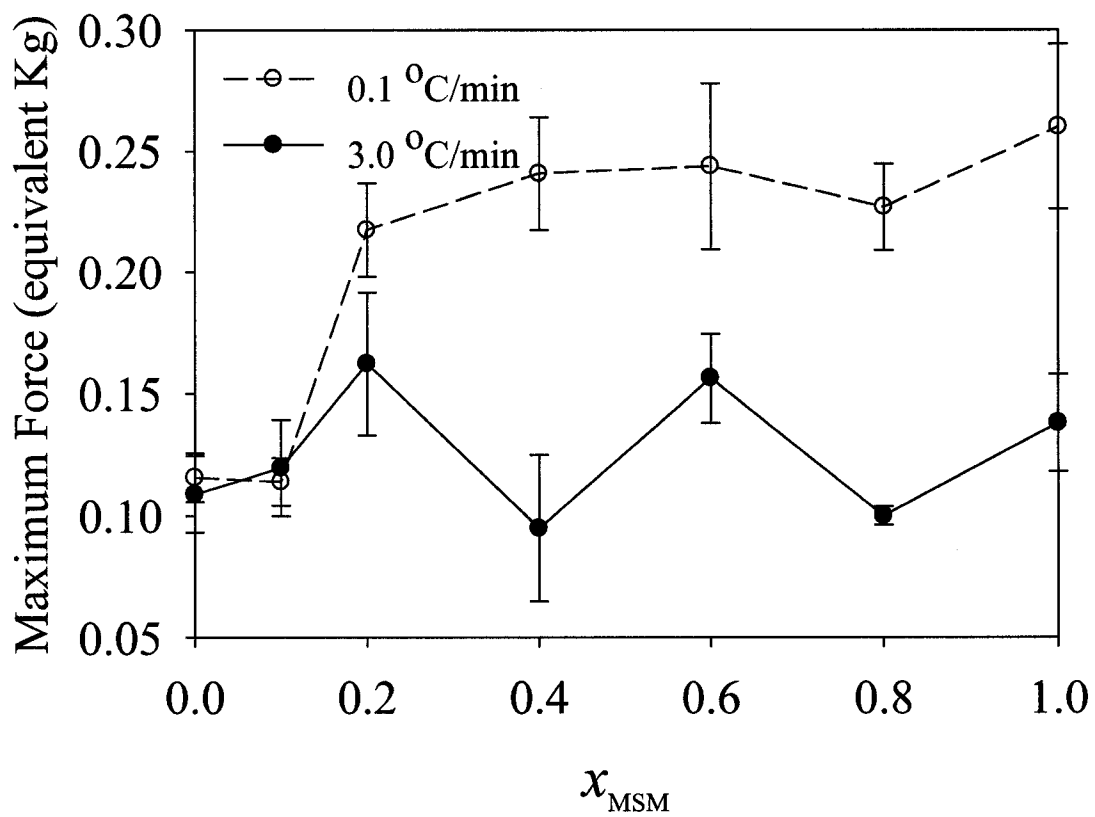


Figure 3-10. Relative hardness vs. MSM molar composition at 0.1 and 3.0 °C/min. Error bars are standard deviations, n= 10.

The increase in relative hardness seen for the 0.1 °C/min rate are probably due to stronger domain interaction initiated by a homogeneous distribution of the MSM phase. The lack of complete correlation between the hardness and the other methods of analysis is not surprising as hardness is a macroscopic rheological property, providing more information about inter-crystalline interactions. Conversely, XRD DSC, and SFC are microscopic in nature, providing information on intra-crystalline interactions.

3.3.3.5. Microscopy

The microstructure of samples processed at 0.1 °C/min is shown in Figure 3-11. Pure MMS has very distinct Maltese crosses which are indicative of spherulitic growth. Spherulites of three different sizes are observed and they are tightly packed. For the 0.1 _{MSM} molar composition, except for sparsely distributed spherulites with excellent contrast (one is seen in the micrograph), only the boundaries of the other crystallites are visible. Poor contrast is observed for the 0.2, 0.4, 0.6 and 0.8 _{MSM} molar compositions. In a study of the polymorphism, crystallization kinetics and microstructure of triplaminin (PPP) (Kellens M., 1992) proposed that such low contrast may be due to numerous spherulites which fuse into a tiny featureless mass. As a result irregular grains with random polarization and the superposition of grains with opposite orientation can result in near zero path length differences. The microstructure for samples processed at 3.0 °C/min (Figure 3-12) contains very similar microstructures except for the 0.8 and 1.0 _{MSM} molar compositions. The symmetric MSM sample formed a bridged network with dark spaces surrounded by small crystal networks with well defined Maltese crosses. These dark spaces may be composed of crystallites which did not have the sufficient driving force to form a network. The higher crystallization temperature of the symmetric TAG may also result in the more rapid crystallization which causes the liquid oil to be entrapped. Such a situation would then limit mass and heat transfer parameters and inhibit the crystallization of the entrapped liquid. This difference in microstructure possibly explains the anomaly in final SFC achieved by these pure TAGs compared to the 0.1 °C/min rate. This visible difference in microstructure can be attributed to different growth modes and rates as alluded to earlier (Table 3-3).

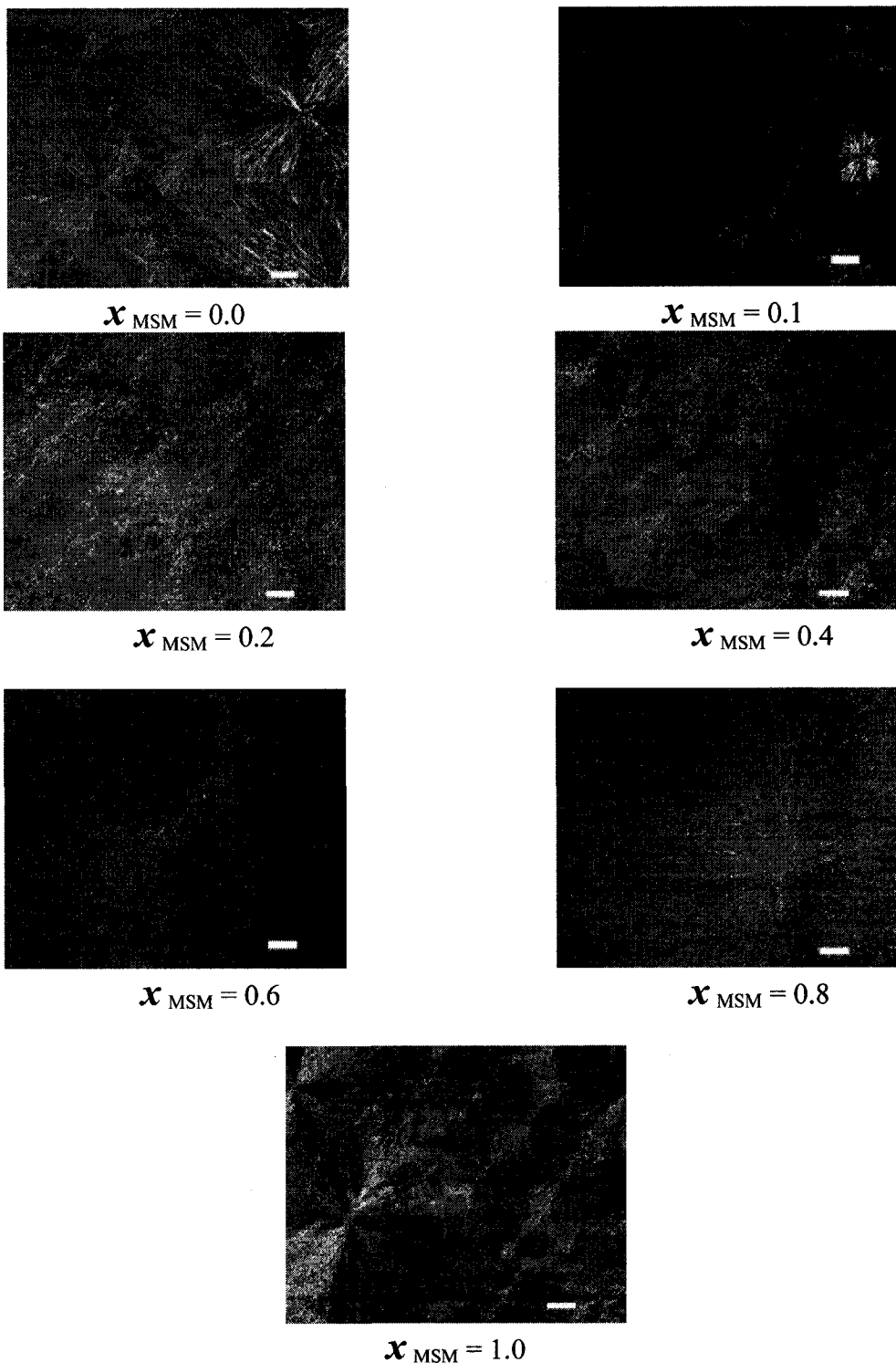


Figure 3-11. Microstructure of pure and binary mixtures of MSM and MMS crystallized at 3.0 °C/min. Magnification = 100 x. Bar = 1 μm

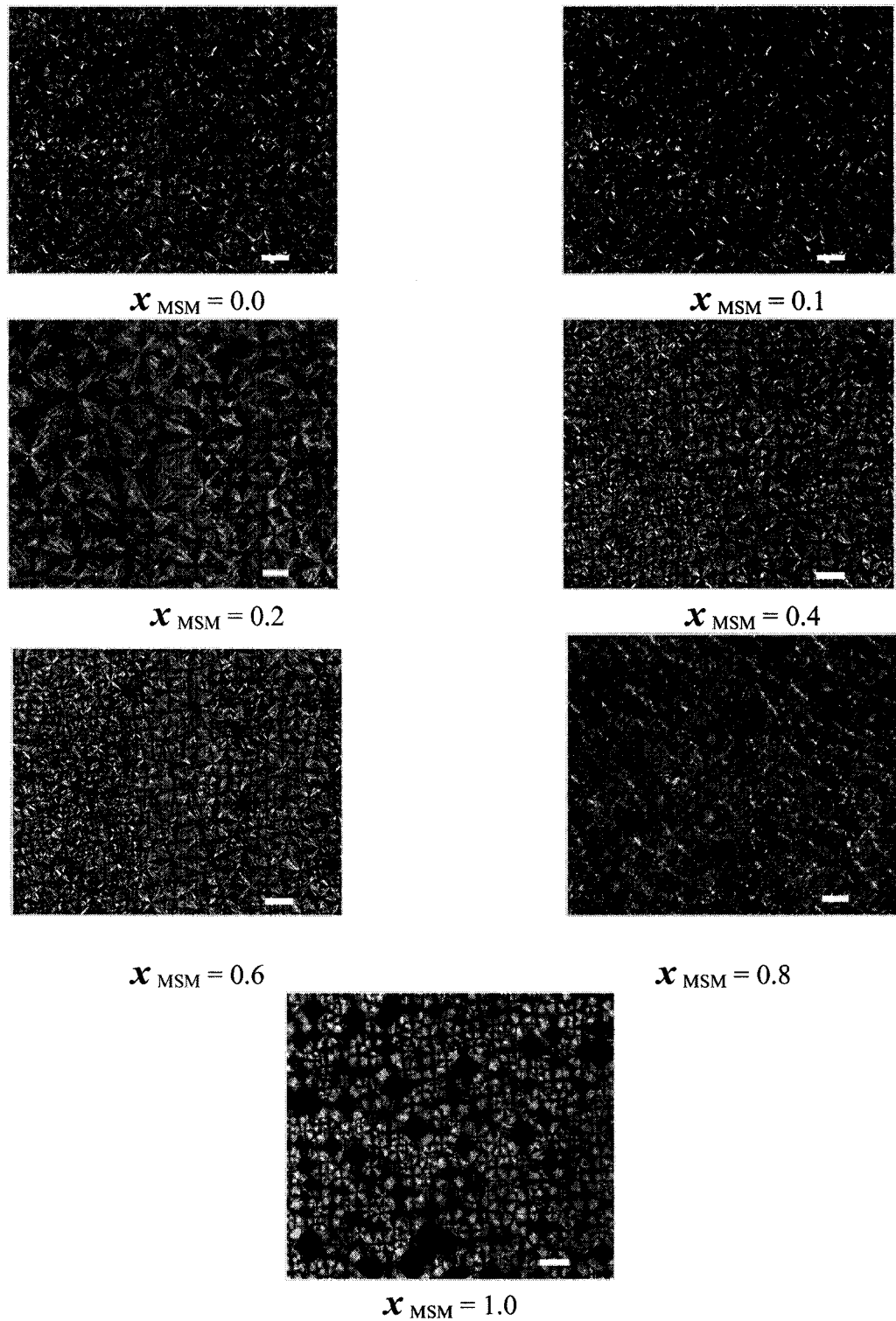


Figure 3-12 Microstructure of pure and binary mixtures of MSM and MMS crystallized at 3.0 °C/min. Magnification = 100 x. Bar = 1 μm

The 0.1_{MSM} sample has a similar microstructure to pure MMS which is also similar to 0.2_{MSM} but the latter has much larger crystal networks. After the 0.2_{MSM} molar composition, the 0.4 and 0.6_{MSM} molar compositions have similar morphologies but smaller crystallites. The 0.8_{MSM} molar composition stands out, as having Maltese crosses but the boundaries between crystals are not sharply separated but seem to be interlocked. They are also more homogeneously distributed.

It is difficult to relate changes in microstructure with Avrami data since samples crystallized on microscope slide as opposed to in an NMR tube are of a different mass, and furthermore will experience different mass and heat transfer limitation despite comparable cooling rates. Variations in crystallite size and shape were observed for α and β' polymorphs.

3.4. Conclusion

The phase behavior of the MSM and MMS binary mixtures was determined using an array of techniques providing insight into the crystallization processes that ranges from atomic level detail to macroscopic properties. The XRD spectra of the pure MSM and MMS samples indicate the α polymorph at 3.0 °C/min and the β' polymorph at 0.1 °C/min as the final crystalline structures. From the XRD data the primitive cell as well as the bilayer length and angle of tilt for the β' polymorph have been identified. The layered structure for the α polymorph could not be elucidated because of limitation of our XRD machine. With the given information, packing modes were proposed for the pure samples.

Phase diagrams constructed from DSC data indicate a monotectic behavior at both cooling rates. Thermodynamic models of both the solidus and liquidus lines provided insight as to the nature of the phase behavior of this binary mixture. Particularly, the use of the Bragg-Williams model strongly indicates that the two components, MSM and MMS, prefer to interact with one another over self interaction in solution. Further application of the modified Bragg-Williams model including data for the solid components clearly shows that the two solids are immiscible in the solid. These findings provide key insight into the interpretation of the XRD for the binary mixtures, as

it can be inferred from the DSC data that the XRD spectra for the mixtures are merely a superposition of XRD spectra resulting from domains of pure MSM and domains of pure MMS.

Melting behavior as shown by DSC melting thermograms and in corroboration with XRD data shows that the α polymorph formed at 3.0 °C/min transformed to the β' polymorph via melt mediated transformation. The formation of the β' polymorph was supported by the close overlay of melting temperatures.

The SFC results clearly reveal eutectic behavior that was not observed by DSC for both crystallization rates. The results of the Avrami fitting clearly show the presence of multiple segments, indicating at least two growth modes for all crystallization rates.

The results of the relative hardness experiments demonstrated a similar hardness for the 0.0 and 0.1 M_{MSM} molar compositions, followed by an increase to 0.2 M_{MSM} and plateau or leveling off of the hardness. In this region, the samples processed at 0.1 °C/min were harder.

The microscopy results demonstrated a spherulitic growth. Microstructure evolution was observed for both cooling rates, arriving at slightly different morphologies.

In conclusion, the phase behavior of the binary mixture of 1,3-dimyristoyl-2-stearoyl-*sn*-glycerol and 1,2-dimyristoyl-3-stearoyl-*sn*-glycerol has been studied using XRD, DSC, SFC, relative hardness and microscopy. While each technique, individually, provides specific information about the molecular structure or the macroscopic morphology, the global consideration of all experimental data has lead to more complete understanding of the binary phase behavior of this mixture. With this information further studies of more realistic fat models, such as ternary and quaternary mixtures, can be contemplated.

3.5. References

- Avrami, M., 1939. Kinetics of Phase Change. I. General Theory. *Journal of Chemical Physics* 7, 1103-1112.
- Bentley, P.H., McCrae, W., 1970. An Efficient Synthesis of Symmetrical 1,3 Diglycerides. *Journal of Organic Chemistry* 35, 2082-2083.
- Bockisch, M., 1998. *Fats and Oils Handbook* AOCS Press, Champaign, Illinois, p 838.
- Campos, R., Narine, S.S., Marangoni, A.G., 2002. Effect of cooling rate on the structure and mechanical properties of milk fat and lard. *Food Research International* 35, 971-981.
- Elisabettoni, P., Lognay, G., Desmedt, A., Culot, C., Itasse, N., Deffense, E., Durant, F., 1998. Synthesis and physicochemical characterization of mixed acid triglycerides that contain elaidic acid. *Journal of American Oil Chemists' Society* 75, 285-291.
- Harrison, W.A., 1980. *Electronic structure and the properties of solids: the physics of the chemical bond*. W. H. Freeman and Company, San Francisco, p 476.
- Inoue, T., Motoda, I., Hiramatsu, N., Suzuki, M., Sato, K., 1993. Phase behavior of binary mixture of palmitoleic acid (cis-9-hexadecenoic acid) and asclepic acid (cis-11-octadecenoic acid). *Chemistry and Physics of Lipids* 66, 209-14.
- Kellens, M., Meeussen, W., Hammersley, A., Reynaers, H., 1991. Synchrotron radiation investigations of the polymorphic transitions in saturated monoacid triglycerides. Part 2: polymorphism study of a 50:50 mixture of tripalmitin and tristearin during crystallization and melting. *Chemistry and Physics of Lipids* 58, 145-58.
- Kellens M., M.W., Reynaers H., 1992. Study of the Polymorphism and the Crystallization of Tripalmitin: A Microscopic Approach. *Journal of American Oil Chemists Society* 69, 906-911.
- Lee, A.G., 1977. Lipid phase transitions and phase diagrams. II. Mixtures involving lipids. *Biochimica et Biophysica Acta, Reviews on Biomembranes* 472, 285-344.

- MacNaughtan, W., Farhat, I.A., Himawan, C., Starov, V.M., Stapley, A.G.F., 2006. A differential scanning calorimetry study of the crystallization kinetics of tristearin-tripalmitin mixtures. *Journal of American Oil Chemists' Society* 83, 1-9.
- Moore, W.J., 1972. *Physical Chemistry*, Englewood Cliffs, New Jersey, pp 229-278.
- Sharples, A., 1966. Overall Kinetics of Crystallization Introduction to Polymer Crystallization. Edward Arnold, London, pp. 44-59.
- Timms, R., 2003. Physical Chemistry. In: *The Confectionary Fats Handbook: Properties, Production, and Application* The Oily Press, Bridgewater, pp. 9-63.
- Toro-Vazquez, J.F., Briceno-Montelongo, M., Dibildox-Alvarado, E., Charo-Alonso, M., Reyes-Hernandez, J., 2000. Crystallization kinetics of palm stearin in blends with sesame seed oil. *Journal of American Oil Chemists' Society* 77, 297-310.
- Vyazovkin, S., Wight, C.A., 1997. Kinetics in solids. *Annual Review of Physical Chemistry* 48, 125-149.

4. The binary phase behavior of 1, 3 – dipalmitoyl-2-stearoyl-sn-glycerol and 1, 2 – dipalmitoyl-3-stearoyl-sn-glycerol

4.1. Introduction

This third study reports on the polymorphism, crystallization, melting and rheological properties of the PSP/PPS binary system. Both PPS and PSP have been studied individually or as a part of other binary TAG systems (Gibon et al., 1986; van Langevelde et al., 1999). Many commercial vegetable shortening systems are made with fully hydrogenated (F.H.) canola, cottonseed, palm or soybean oils, all of which contain PSP and PPS in relatively small quantities. F.H. cottonseed oil contains approximately 11% PPS and F.H. palm oil 39% PSP while F.H. canola and soybean contain both isomers in concentrations of less than 2%. Despite being present in small quantities, PSP and PPS have been shown to influence key functional properties such as melting behavior and hardness when present in a shortening type system containing a wide variety of TAGs (Humphrey and Narine, 2004).

Samples were processed at two extreme crystallization rates, namely 0.1 °C/min and 3.0 °C/min, in order to investigate the influence of cooling rate on the above named properties.

4.2. Materials and Methods

The pure PSP and PPS TAGs were synthesized according to known procedures (Bentley and McCrae, 1970). Purity of all samples exceeded 98.0% as determined by gas chromatography fitted with a mass spectrometer detector. PSP and PPS samples were prepared and processed in a manner identical to LSL/LLS samples detailed in Chapter 2.

A version of this chapter has been submitted for publication to Chemistry and Physics of Lipids, May 2007.

4.3. Results and Discussion

4.3.1. XRD Results

Figure 4-1 shows the XRD spectra obtained at a cooling rate of 0.1 °C/min. The lowermost spectrum represents pure PPS (0.0 x_{PSP}). The stacked spectra above the pure PPS spectrum are for samples of increasing molar concentrations of PSP up to $x_{\text{PSP}} = 1.0$, which is the uppermost spectrum. Similar XRD spectra (not shown) were observed for all samples when cooled at 3.0 °C/min indicating that cooling rate did not impact the final polymorphic form of the TAGs.

In the long spacing region ($2\theta \leq 18^\circ$), two distinct peaks (P_1 and P_2) were resolved and their d values (d_1 , and d_2) are shown as a function of molar composition in Figure 4-2. As can be seen, all long spacing values observed are indicative of the same lamellar packing mode for all molar fractions. In the short spacing region ($2\theta > 18^\circ$), a single peak centered at the same position ($2\theta = 20.3 \pm 0.1$) was observed. It corresponds to a d -spacing of 4.1 ± 0.1 , characteristic of an α polymorph.

The α polymorph consists of loosely packed vertical chains (Timms, 2003) and may exist as a double chain length (DCL) and/or triple chain length (TCL) structure (Figure 4-2 (B)). A calculation based on the PSP and PPS chain length with no tilt yields a maximum lamellar periodicity of $L \sim 50 \text{ \AA}$ ($2\theta \sim 1.6^\circ$) for a DCL structure, and a minimum lamellar periodicity of $L \sim 77 \text{ \AA}$ ($2\theta \sim 1.1^\circ$) for a TCL structure. These large L values are associated with small diffraction 2θ values and cannot be resolved with our instrument. The long spacing peaks which were obtained with our instrument are harmonics of such fundamental peaks.

The miscibility of PSP and PSP TAGs in the solid state cannot be resolved by XRD since both molecules have the same size and similar unit cell parameters. Miscibility of the TAGs will be further elaborated on in the discussion of the DSC results.

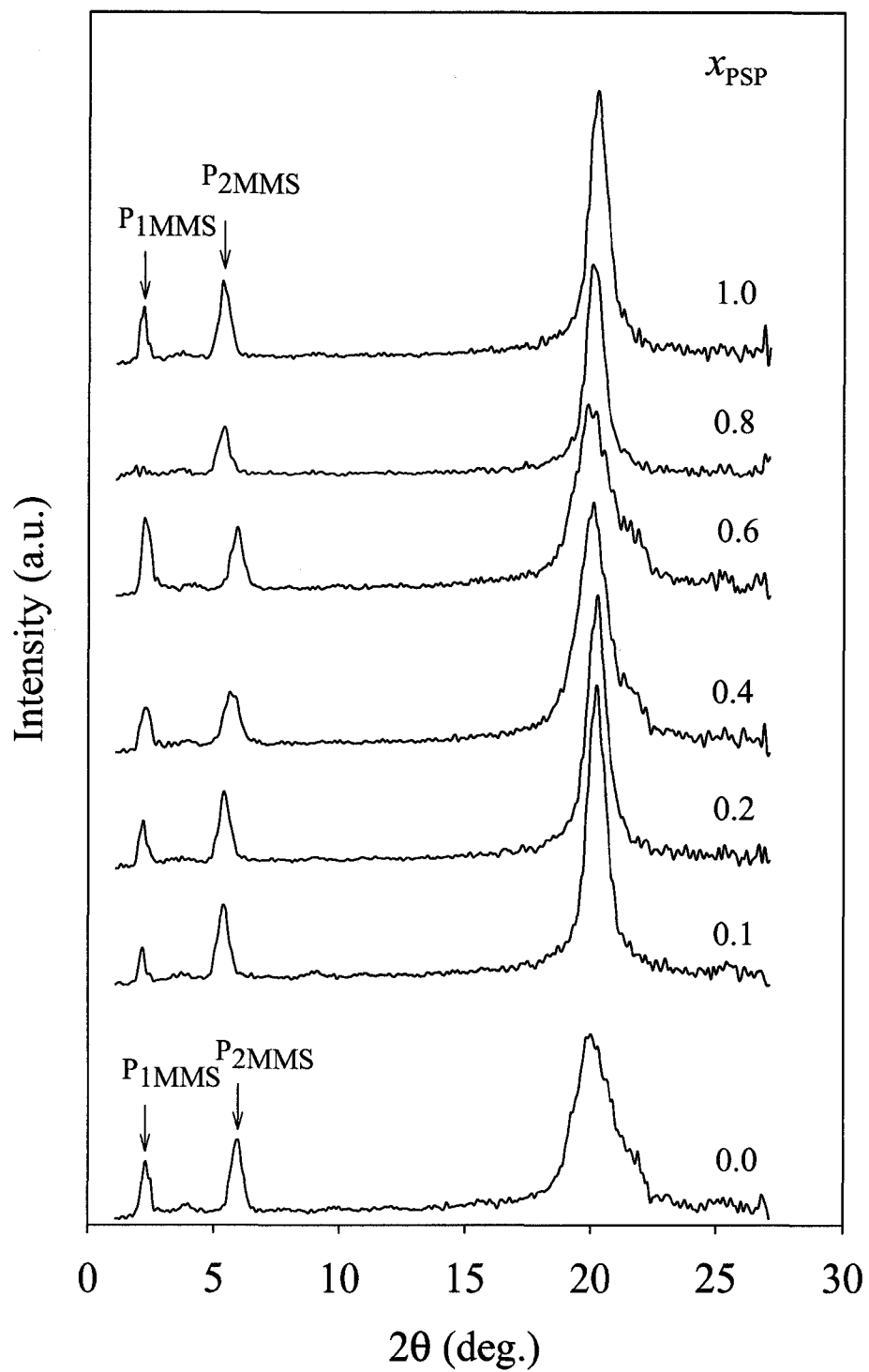


Figure 4-1. XRD spectra of PSP/PPS mixtures crystallized at 0.1°C/min.

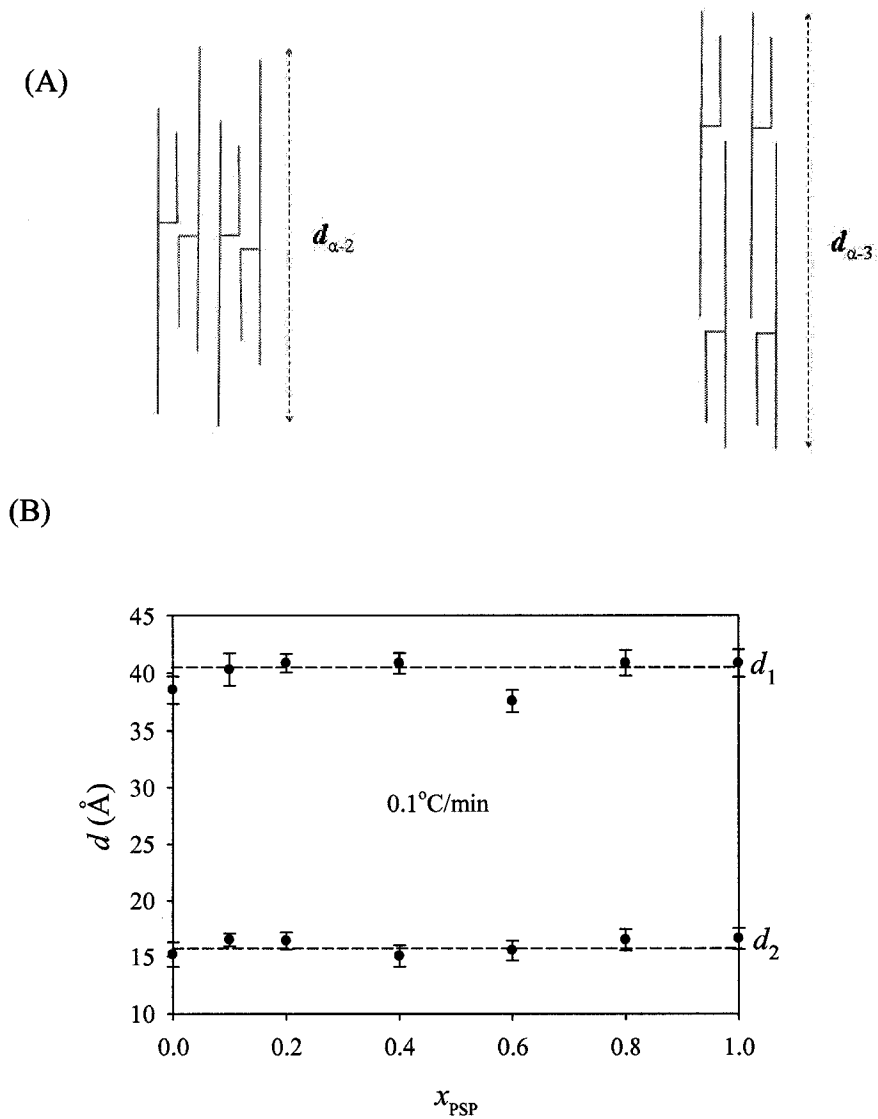


Figure 4-2. (A) Stacking mode of PSP/PPS mixtures (B) Variation of d_1 and d_2 long spacing as a function of the PSP molar fraction. Error bars are standard deviations, $n=3$.

4.3.2. DSC Results

4.3.2.1. Crystallization Behavior

Crystallization thermograms obtained at 0.1 and 3.0 °C/min are shown in Figure 4-3 (A) and (B), respectively. At the 0.1 °C/min cooling rate; a narrow, sharp and symmetrical peak (P₁) was observed for 0.0 x_{PSP} . As PSP fraction increased, the peaks became more asymmetric but had similar widths at half maximum up to 0.4 x_{PSP} . A second peak (P₂) appeared for the 0.4, 0.5 and 0.6 x_{PSP} mixtures as shown in the insert of Figure 4-3 (A).

These peaks were well resolved which allowed for a good estimation of their position, width and area. It was obvious that a second thermal event started to appear for PSP content as low as 0.1 but couldn't be resolved until 0.4 x_{PSP} as it was small compared to the main peak. The individual areas of the peaks were estimated after a simple deconvolution of the signal into two components and are shown in Figure 4-3 (C).

Multiple peaks are indicative of a phase separation or de-mixing during the crystallization process (MacNaughtan et al., 2006). P₁ can be safely attributed to the crystallization of a PPS phase and P₂ to the crystallization of a PSP phase. One can postulate that for all the PPS/PSP binary mixtures, there appears two separate phases, a PSP phase which crystallizes first (by virtue of its higher crystallization temperature) followed by the crystallization of a PPS phase. The ratios of the full width at half maximum (FWHM) of P₂ to the normalized peak height were ~ 20, 6 and 4 °C/(W/g) for the 0.4 x_{PSP} , 0.5 x_{PSP} and 0.6 x_{PSP} samples, respectively, indicating better packing and an increase in distribution homogeneity of the PSP domains. As can be seen in Figure 4-3 (C), the crystallization enthalpy of the PPS phase increased while that of PSP phase decreased with increasing x_{PSP} . The two curves were almost symmetrical about $x_{PSP} = 0.5$ and evidenced that while there is a phase separation in the solid state, an interchange coupling exists between the different domains (PPS-PPS and PSP-PSP).

The crystallization peaks broadened at 3.0 °C/min (Figure 4-3 (B)) compared to the crystallization at 0.1 °C/min (Figure 4-3 (A)). This peak broadening is due to the incorporation of more species from the melt due to a higher thermodynamic driving force. The peaks also shifted to higher temperatures (~2 °C) at 3.0 °C/min (Figure 4-3 (D)).

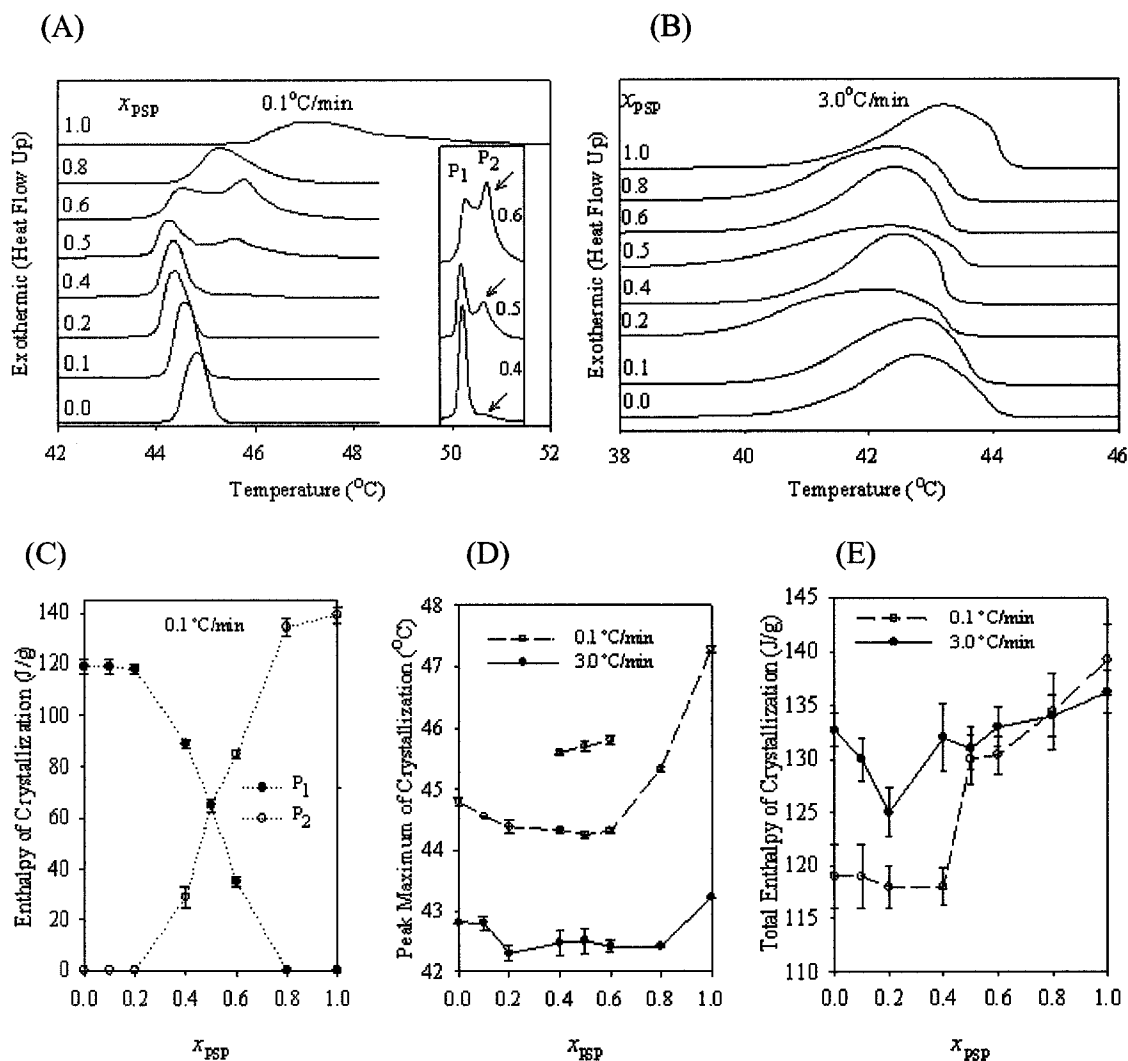


Figure 4-3. (A) Crystallization curves of PSP/PPS binary mixtures vs. PSP molar fraction at 0.1 °C/min. Insert highlights the crystallization curves of the 0.4, 0.6 and 0.8 x_{PSP} molar compositions, (B) Crystallization curves of PSP/PPS binary mixtures vs. PSP molar fraction at 3.0 °C/min, (C) Enthalpy of crystallization of the resolved crystallization peaks P_1 and P_2 vs. PSP molar fraction at 0.1 °C/min, (D) Peak maximum of crystallization vs. PSP molar fraction at 0.1 and 3.0 °C/min, (E) Total enthalpy of crystallization vs. PSP molar fraction at 0.1 and 3.0 °C/min. Error bars are standard deviations, $n=3$.

At 0.1 °C/min a slight depression in crystallization temperature is observed between 0.1 – 0.6 x_{PSP} (Figure 4-3 (D).) and between 0.2 – 0.8 x_{PSP} at 3.0 °C/min. At the 3.0 °C/min cooling rate, less time is spent just above the crystallization temperature resulting in relatively less lamellar organization taking place prior to nucleation; thus the shift to higher temperatures. All peaks demonstrated an asymmetrical shape and subtle difference were observed in their widths but there was no definite evidence of a phase separation.

Figure 4-3 (E) shows the total enthalpy of crystallization as a function of x_{PSP} at 0.1 and 3.0 °C/min. The enthalpies of crystallization were higher at the faster cooling rate for the samples 0.0 – 0.4 x_{PSP} inclusive and were similar for the 0.6 – 1.0 x_{PSP} mixtures. This suggests that more molecules are coming into the solid state from the melt despite of the fact that their packing – and therefore their interactions – is not ideal. Therefore, the aggregate enthalpies at 3.0°C/min were higher than at 0.1°C/min. Clearly, the domain separation seen at the 0.1 °C per min crystallization rate is motivated by more ordered domains with increased intermolecular forces, as opposed to the 3°C per minute, where the converse is true.

4.3.2.2. Melting Behavior

For the 0.1 °C/min cooling rate (Figure 4-4 (A)), melting DSC curves for the 0.0-0.6 x_{PSP} molar compositions demonstrated two melting peaks (P_1 and P_2) separated by a melt mediated crystallization peak. At the 3.0 °C/min crystallization rate similar melting profiles were observed (Figure 4-4 (B)). This is indicative of a polymorphic transformation. The less stable polymorph obtained at these cooling rates transforms via melt mediated crystallization to a thermodynamically more stable polymorph which finally melts. Based on XRD results, the lower melting peak P_1 could be safely assigned to the α form and the higher melting peak P_2 to the β' form.

Peak maximum of melting versus PSP molar composition for P_1 and P_2 observed when crystallized at 0.1 °C/min and 3.0 °C/min overlay very closely as shown in Figure 4-4 (C). This suggests that the same transformation occurred when melting the samples at both cooling rates. The peak maximum of melting for the lower melting peak is almost

constant, while the peak maximum of melting of the higher melting peak displayed a eutectic behavior.

The enthalpies of the respective ($P_1 - \alpha$) and ($P_2 - \beta'$) melting peaks were estimated by a direct measure of the area between the endotherm and a linear baseline. At both cooling rates, the area of P_1 decreased, while the area of P_2 increased with increasing PSP composition (Figure 4-4 (D)). For the 0.1 °C/min crystallization rate, ~90% of the pure PPS directly melted without transforming to the more stable polymorph.

With increasing PSP content, and up to 0.6_{PPS}, the amount of the melted material without transformation decreased to zero almost linearly. There was no melting prior to recrystallization for the 0.8_{PSP} and 1.0_{PSP} samples indicating that it is mainly the phase containing PSP that undergoes the polymorphic transformation. Cooling rate did not influence significantly the overall transformation. The lower melting peak ($P_1 - \alpha$) can therefore be assigned to the melting of the non transformed PPS phase and the second peak ($P_2 - \beta'$) primarily to the melting of the transformed PSP phase.

4.3.2.3. Phase Diagram of the PSP/PPS Binary System

The PPS/PSP binary phase diagram was constructed from the melting thermograms shown in Figure 4-4 (A). The peak maximum of melting temperature was used to represent the liquidus line and the end of melting temperature of the said peaks was used to represent the solidus line. The phase diagram displayed a eutectic phase behavior with a eutectic point $x_E = 0.2$ _{PSP} at both cooling rates. The phase diagram constructed using the 0.1 °C/min data is shown in Figure 4-5 (A).

A common thermodynamic model based on the Hildebrand equation (Inoue et al., 1993; Lee, 1977) and detailed in Chapter 2 (Section 2.3.2.3) was used to simulate the phase boundaries in the *Temperature–molar fraction* phase diagram.

When assuming an ideal solution and complete immiscibility of the components PPS and PSP in the solid phase, the model did not fit the experimental data. However, the model predicted a eutectic at the 0.2_{PSP} molar composition which correlates with the experimental data.

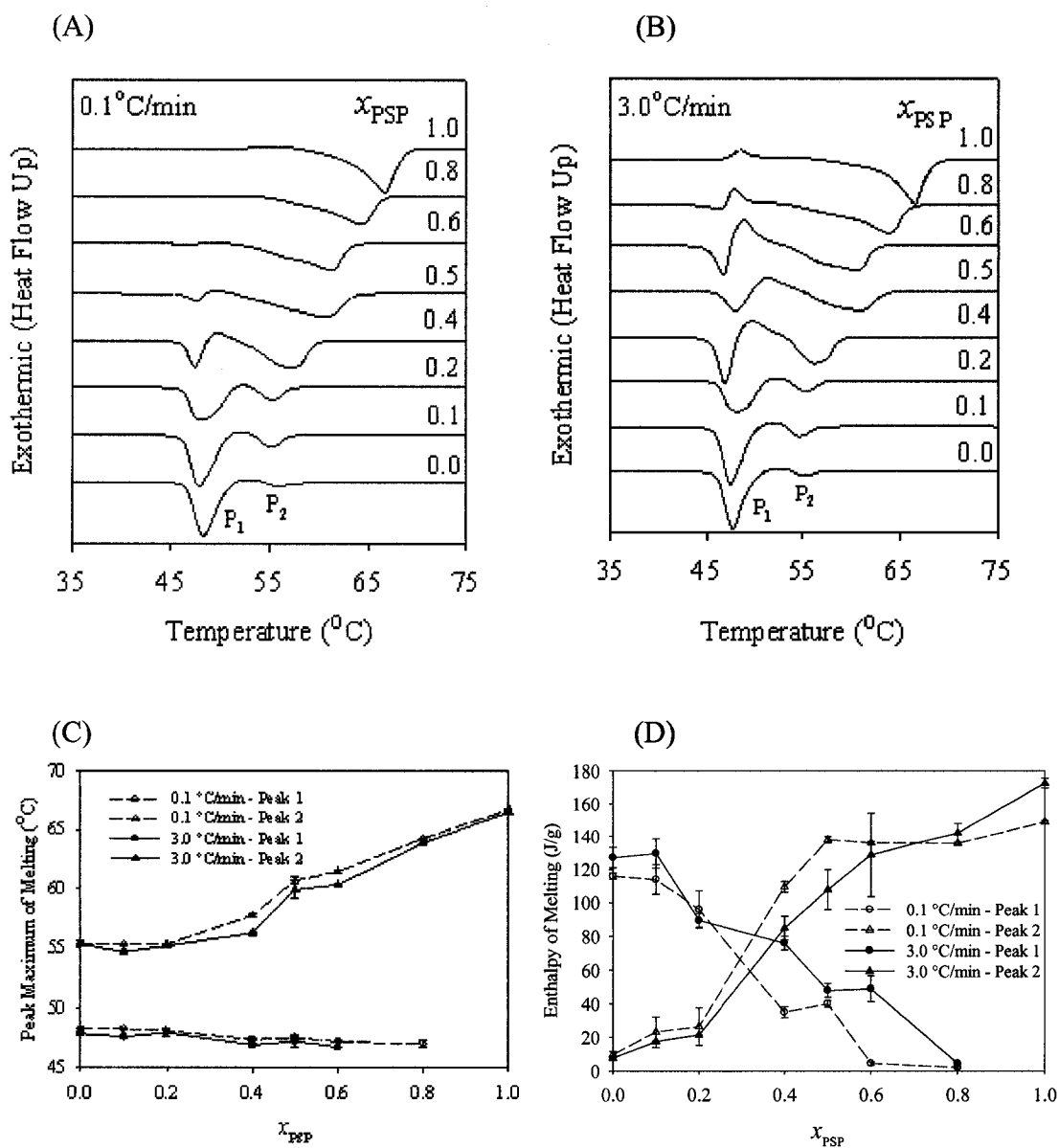


Figure 4-4. (A) Melting curves of PSP/PPS binary mixtures as a function of PSP molar fraction at $0.1\text{ }^{\circ}\text{C}/\text{min}$, (B) Melting curves of PSP/PPS binary mixtures as a function of PSP molar fraction at $3.0\text{ }^{\circ}\text{C}/\text{min}$, (C) Enthalpy of melting as a function of PSP molar fraction at 0.1 and $3.0\text{ }^{\circ}\text{C}/\text{min}$, (D) Enthalpy of melting as a function of PSP molar fraction at 0.1 and $3.0\text{ }^{\circ}\text{C}/\text{min}$. Error bars are standard deviations, $n=3$.

The so-called Bragg-Williams approximation (detailed in Chapter 2) has been used to take into account the deviation from an ideal behavior. The Bragg-Williams approximation is appropriate for the description of the non-ideality of mixing of mixtures of components with similar molecular structure and molar volume such as PPS and PSP. In this approximation, the non-ideality of mixing is characterized by a non-ideality parameter, ρ .

ρ is the energy difference between (A–B) pair and the average of (A–A) pair and (B–B) pair. For ideal mixing, ρ is zero. Positive ρ reflects a tendency of like molecules to cluster, which beyond some critical value, ρ_c , leads to a phase separation. A negative ρ reflects a tendency for order, i.e. the formation of AB pairs is energetically more favorable compared with AA or BB pair formation. (Lee, 1977)

The experimental liquidus and solidus lines have been most closely reproduced by this model when assuming non-ideal mixing in both liquid and solid states.

The liquidus line $x_A^L = x_A^L(T)$ and the solidus line $x_A^S = x_A^S(T)$ have been obtained by solving the simultaneous equations 2 and 3 (Chapter 2). The parameters ρ_L and ρ_S were optimized and the fitting of the calculated curve to the experimental points was judged by visual inspection. The calculated curves for the 0.1 °C/min rate are represented by the solid line in Figure 4-5. The best fit was achieved using $\rho_L = -0.9 \text{ kJmol}^{-1}$ and $\rho_S = +6.0 \text{ kJmol}^{-1}$.

The small negative value for ρ_L suggests close to ideal mixing in the liquid state with a small tendency for PPS-PSP formation over PSP-PSP and PPS-PPS formation. However, a relatively large positive ρ_S indicates that PSP and PPS are immiscible in the solid state. This is expected since the solidus line is flat between 0.0 – 0.8_{PSP} molar compositions.

The phase diagrams for 1.0 and 3.0 °C/min were very similar as can be inferred from the close overlay of peak maxima of melting for both cooling rates (Figure 4-4 (C)). Cooling rate clearly did not influence the phase behavior of this system nor its polymorphism as discussed earlier.

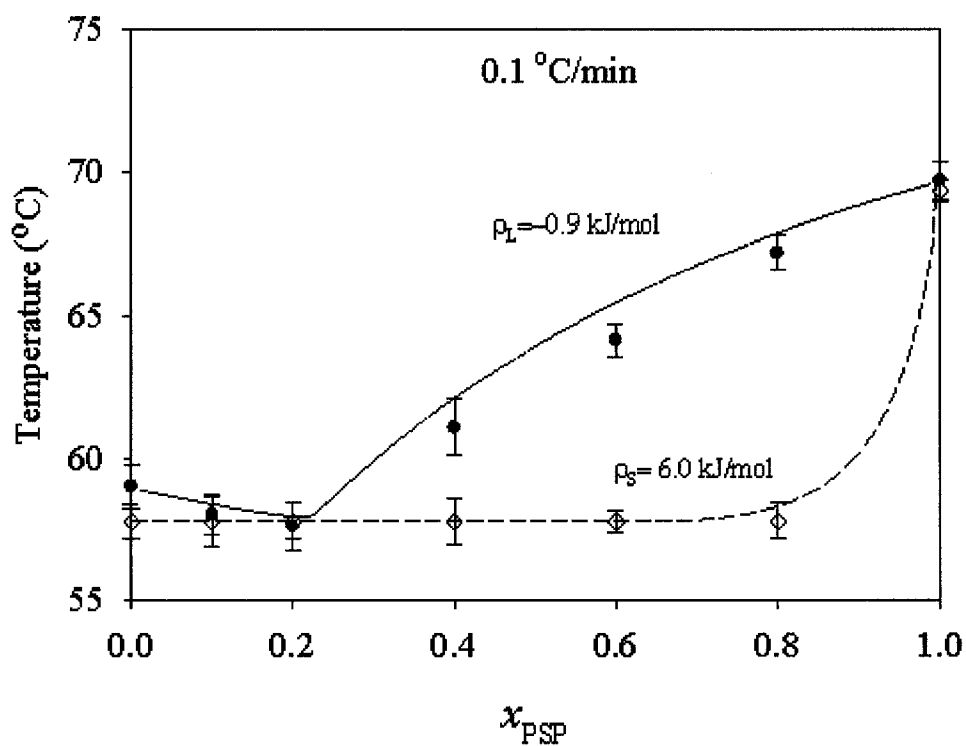


Figure 4-5. Phase diagram of the PSP/PPS binary system constructed using DSC data obtained for the samples crystallized at 0.1 °C/min. Simultaneous fit of the liquidus and solidus lines (solid lines) considering nonideality of mixing, using equations 6 and 7. Error bars are standard deviations, $n=3$.

4.3.2.4. Determination of Energy of Activation for Nucleation

Activation energies of nucleation were calculated as outlined in Chapter 2. Variation and fit of the normalized nucleation rate $\frac{J}{J_{max}}$ vs $\sqrt{\beta}$ and its variation and fit as a function of $\frac{1}{\sqrt{\phi}}$ for each sample were plotted. From the fit of these plots, k and X were determined respectively. All exponential fits to experimental data were excellent. Table 4-1 lists the results (k , Z , X , and Q_m) of these fits.

The calculated activation energy is higher for the asymmetric PPS than the symmetric PSP (see Figure 4-6) suggesting that the symmetric TAG has a greater tendency for ease of nucleation possibly due to less steric hindrance to packing. A depression in activation energy was observed at 0.2 PSP, followed by a maximum value at 0.6 PSP. The depression in activation energy correlates with the eutectic point as determined from the thermodynamic phase diagram but it is unclear why the maximum was observed. The assignment of the activation energy as calculated to an isolated nucleation mechanism cannot be fully justified. The DSC experimental technique do not provide complete isolation of an elementary mechanism such as nucleation (or nuclei growth) uncomplicated by other physical processes such as diffusion. The calculated value for the activation energy is therefore global in nature and incorporates the activation energies of several crystallization mechanisms.

4.2.3.3. Solid Fat Content (SFC)

The SFC (%) versus time curves, obtained at 0.1°C/min and 3.0 °C/min crystallization rate, is shown in Figure 4-7 (A) and (B), respectively.

All curves demonstrated two distinct segments of growth, each representing a distinct rate and growth mode. Except for the SFC trace of the 1.0 PSP sample which stands out with a steeper slope in its first segment, all the SFC (%) versus time curves have similar shapes. However, their induction time differ significantly. Its evolution vs. composition (Figure 4-7 (C)) is clearly dictated by the eutectic behavior.

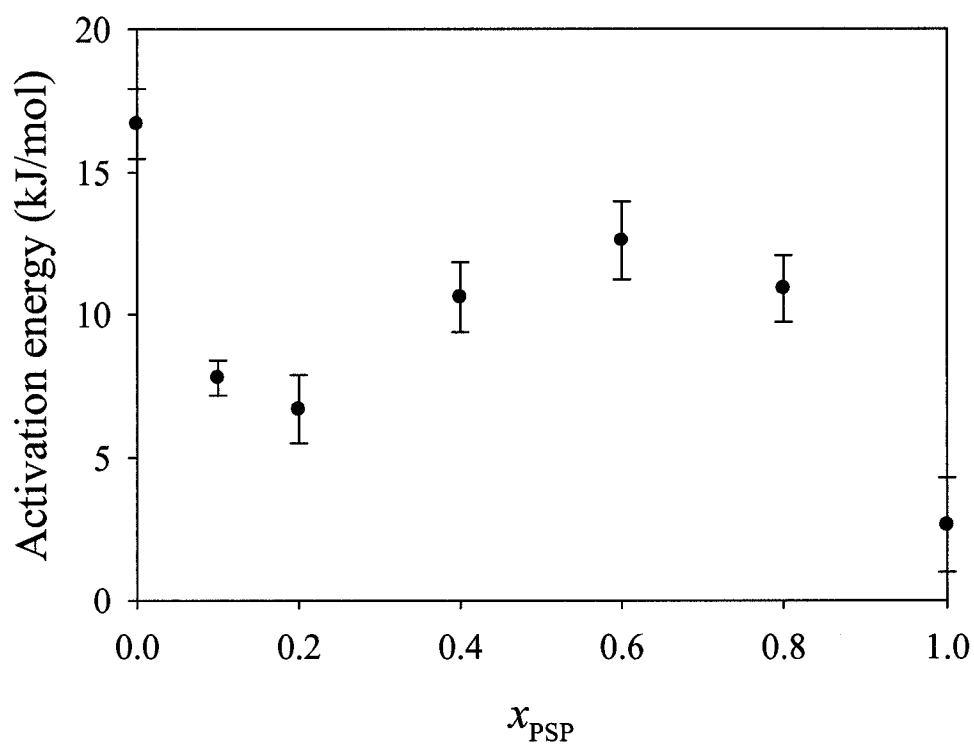


Figure 4-6. Activation energy of nucleation vs. PSP molar composition. Error bars are standard deviations, $n=3$

x_{PSP}	k ($K^{-1/2}s^{-1/2}$)	Z ($Jg^{-1}K^{-1/2}s^{1/2}$)	X	Q_m^* (kJ/mol)
0.0	0.07 ± 0.01	39.9 ± 1.1	0.58 ± 0.04	16.8 ± 1.2
0.1	0.09 ± 0.02	32.9 ± 1.2	1.33 ± 0.02	7.9 ± 1.0
0.2	0.09 ± 0.01	32.3 ± 1.1	0.29 ± 0.05	6.7 ± 1.2
0.4	0.07 ± 0.02	40.0 ± 1.1	0.37 ± 0.04	10.6 ± 1.3
0.6	0.06 ± 0.03	44.0 ± 1.2	0.40 ± 0.02	12.7 ± 1.4
0.8	0.06 ± 0.02	50.8 ± 1.1	0.30 ± 0.02	11.0 ± 1.2
1.0	0.07 ± 0.01	38.2 ± 1.3	0.10 ± 0.02	2.6 ± 1.6

*Molar energy of activation was calculated as $Q = Z*X*MW$. The average molecular weight used for PSP and PPS was 835 g/mol

Table 4-1. Exponential constants (k , Z and X) and energy of activation for nucleation (Q_m) for pure and binary mixtures of PSP and PPS crystallized at 0.1 °C/min

As can be seen for both rates, the induction time was maximum for the eutectic composition ($x_E = 0.2_{\text{PSP}}$), decreased with increasing PSP at the right side of x_E and decreased with increasing PPS at the left side of x_E . The induction time of the asymmetric PPS was higher than that of the symmetric PSP which may be due to the latter's propensity to pack more readily.

The SFC (%) versus time segments were fitted to a modified form of the Avrami model that takes into consideration the variances within the growth curve (Narine et al., 2006) as detailed in Chapter 2. The calculated Avrami constant (A) and exponent (n) are presented in Tables 4-2 and 4-3.

For the 0.1 °C/min crystallization rate, the Avrami parameters calculated for the first segment of growth were almost the same ($A \sim 1.9 \times 10^{-5}$ and $n \sim 1.3$) for all samples. The Avrami constant, A, is dependent upon the nucleation rate, suggesting a similar nucleation rate for all samples. The exponent n is a function of the number of dimensions in which growth takes place. In the second segment of growth, the A values were found to be two orders of magnitude larger ($A \sim 1 \times 10^{-3}$), which corresponds to an increased rate of crystallization, while the n value was ~ 1 indicating a similar mode of growth. Note that the eutectic composition of 0.2_{PSP} did not reveal any different mode of growth.

At 3.0 °C/min the Avrami parameters in the first segment of growth were similar for the 0.0 – 0.8_{PSP} molar compositions ($A \sim 2.0 \times 10^{-5}$, $n \sim 1.3$) while the pure PSP (1.0_{PSP}) was different ($A = 5.24 \times 10^{-5}$, $n = 1.8$). These higher A and n values for pure PSP implies a higher crystallization rate as well as a different mode of growth ($n \sim 2$) respectively. In the second segment, the curves for all compositions were similar ($A \sim 1 \times 10^{-3}$, $n \sim 1$).

Except for different A values for the various segments, the Avrami index n was ~ 1 at both cooling rates, indicating a common mode of growth. There were however subtle differences in these non integer values for n.

Possible explanations put forward for such small dimensionalities of growth include changing rates of radial growth of domains, geometric restrictions to domain growth or differences in underlying geometries which influence growth among others (Yang and Nagle, 1988).

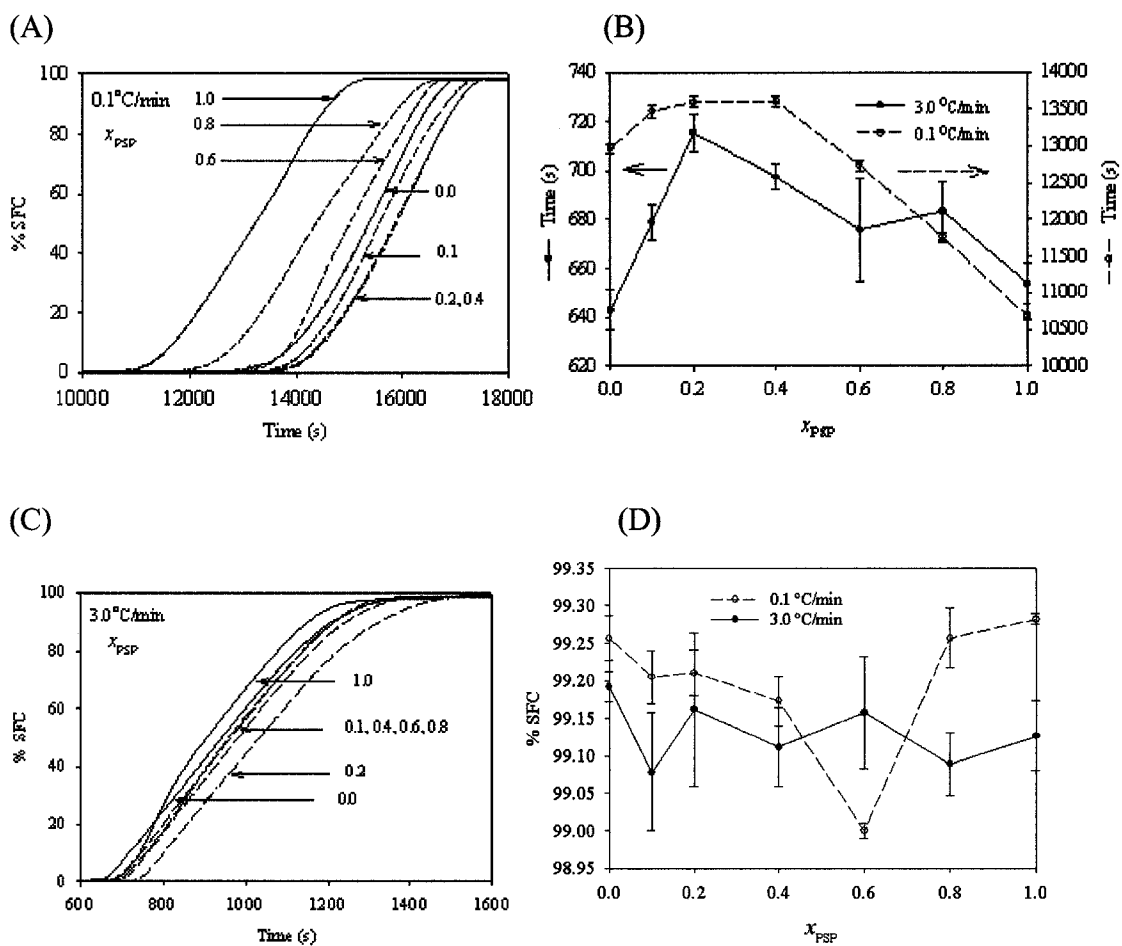


Figure 4-7. (A) SFC (%) vs. time plots for pure and binary mixtures of PSP and PPS at 0.1 °C/min (B) Induction time (s) vs. PSP molar composition at 0.1 and 3.0 °C/min, (C) SFC (%) vs. time plots for pure and binary mixtures of PSP and PPS at 3.0 °C/min (D) Final (%) SFC vs. PSP molar composition at 0.1 and 3.0 °C/min. Error bars are standard deviations, $n=3$

Sample	Segment 1		Segment 2	
	A (1×10^{-5}) (s^{-1})	n	A(1×10^{-3}) (s^{-1})	n
0.0	1.10 ± 1.70	1.2 ± 0.1	1.03 ± 0.03	1.2 ± 0.1
0.1	0.78 ± 0.25	1.3 ± 0.2	1.01 ± 0.17	1.2 ± 0.2
0.2	1.84 ± 0.40	1.3 ± 0.3	0.71 ± 0.10	1.2 ± 0.2
0.4	1.08 ± 0.50	1.3 ± 0.1	0.90 ± 0.10	1.2 ± 0.1
0.6	2.60 ± 0.60	1.2 ± 0.2	0.81 ± 0.14	1.1 ± 0.2
0.8	3.40 ± 0.60	1.2 ± 0.1	1.25 ± 0.05	1.1 ± 0.1
1.0	2.64 ± 1.11	1.5 ± 0.3	1.56 ± 0.06	1.1 ± 0.1

Table 4-2. Avrami constant (A) and exponent (n) determined using the modified form of the Avrami for samples crystallized at 0.1 °C/min.

Sample	Segment 1		Segment 2	
	A (1 x 10 ⁻⁵) (s ⁻¹)	n	A (1 x 10 ⁻³) (s ⁻¹)	n
0.0	1.10 ± 0.35	1.2 ± 0.1	1.03 ± 0.03	1.2 ± 0.1
0.1	0.80 ± 0.25	1.4 ± 0.1	1.01 ± 0.17	1.2 ± 0.1
0.2	1.84 ± 0.40	1.3 ± 0.2	0.71 ± 0.10	1.2 ± 0.2
0.4	1.10 ± 0.40	1.3 ± 0.2	0.89 ± 0.10	1.1 ± 0.1
0.6	2.56 ± 0.45	1.3 ± 0.2	0.81 ± 0.14	1.2 ± 0.1
0.8	3.40 ± 0.06	1.2 ± 0.3	1.25 ± 0.05	1.1 ± 0.2
1.0	5.24 ± 0.89	1.8 ± 0.1	1.56 ± 0.06	1.1 ± 0.1

Table 4-3. Avrami constant (A) and exponent (n) determined using the modified form of the Avrami for samples crystallized at 0.1 °C/min.

The final SFC (%) attained for all samples at both cooling rates is $99.2 \pm 0.1\%$ except for a depression at 0.6_{PSP} ($99.0 \pm 0.1\%$) at $0.1^\circ\text{C}/\text{min}$ (see Figure 4-7 (D)).

The depression in SFC (%) at 0.6_{PSP} did not correlate with the eutectic point ($x_E = 0.2_{\text{PSP}}$) which was determined from the phase diagram constructed using DSC data. Such correlations are however not surprising, as it is entirely conceivable that the lower or higher melting polymorphs do not necessarily account for a proportionate amount of the final SFC (%).

4.3.4. Relative Hardness

At $0.1^\circ\text{C}/\text{min}$ all molar compositions (see Figure 4-8) were of similar relative hardness ($0.31 \pm 0.04 \text{ Kg}$) except for a depression at 0.6_{PSP} ($0.21 \pm 0.01 \text{ Kg}$), while at $3^\circ\text{C}/\text{min}$ there were no depressions and the average relative hardness was ($0.44 \pm 0.03 \text{ Kg}$). Notably, samples were harder at the higher cooling rate, where smaller crystallites are formed. Relative hardness correlated very well with the final SFC (%) at both cooling rates.

4.3.5. Microscopy

Well defined crystallites were observed for all compositions at $3.0^\circ\text{C}/\text{min}$ (Figure 4-9) as evidenced by the presence of Maltese crosses except for the eutectic composition of 0.2_{PSP} . The 0.0 and 0.1_{PSP} samples both have relatively large crystallites, but at the 0.2_{PSP} molar composition there is an abrupt change in the crystallite size and the Maltese pattern is absent. From the 0.4_{PSP} composition and above, clearly defined crystallites with Maltese crosses are again obvious and they increase in size with increasing PSP composition. This kind of structure is clearly motivated by the PSP phase. At the $0.1^\circ\text{C}/\text{min}$ cooling rate, there is no obvious trend in the evolution of microstructure with increasing PSP composition (see Figure 4-10). The 0.0 and 0.1_{PSP} are similar, but at the eutectic composition 0.2_{PSP} , the crystallites increase in size, and the intercrystalline boundaries are widely spaced. At 0.4_{PSP} crystallites were similar to those observed for the 0.2_{PSP} sample. At 0.6_{PSP} , smaller crystallites of two different sizes are observed. Larger crystallites are again present at 0.8

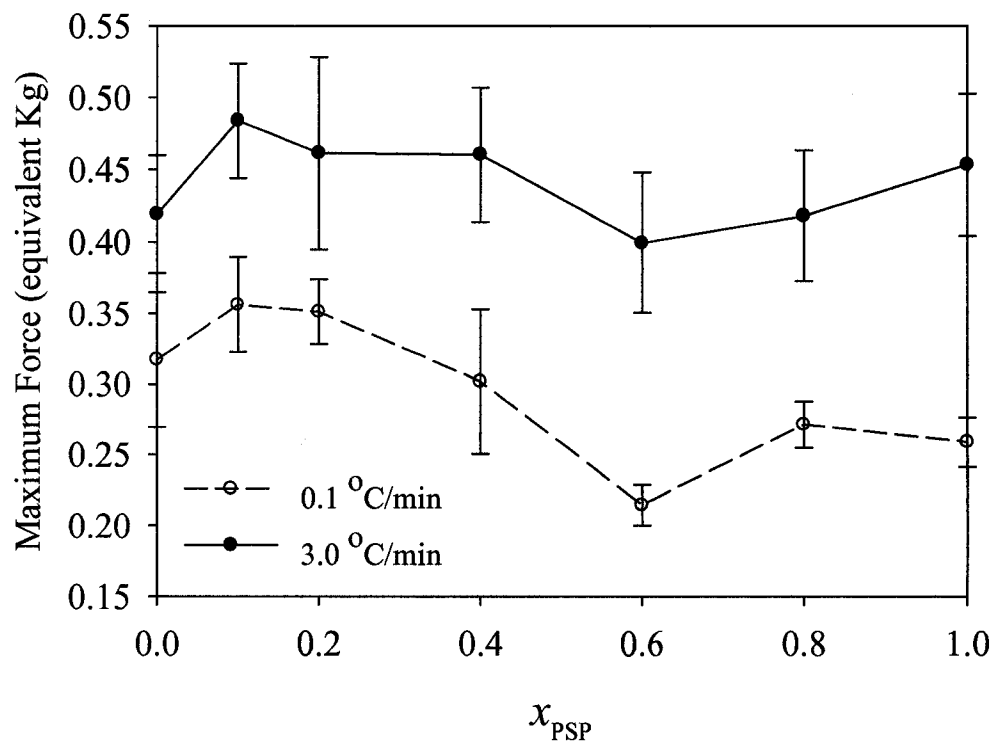


Figure 4-8. Relative hardness vs. PSP molar composition at 0.1 and 3.0 °C/min. Error bars are standard deviations, n= 3

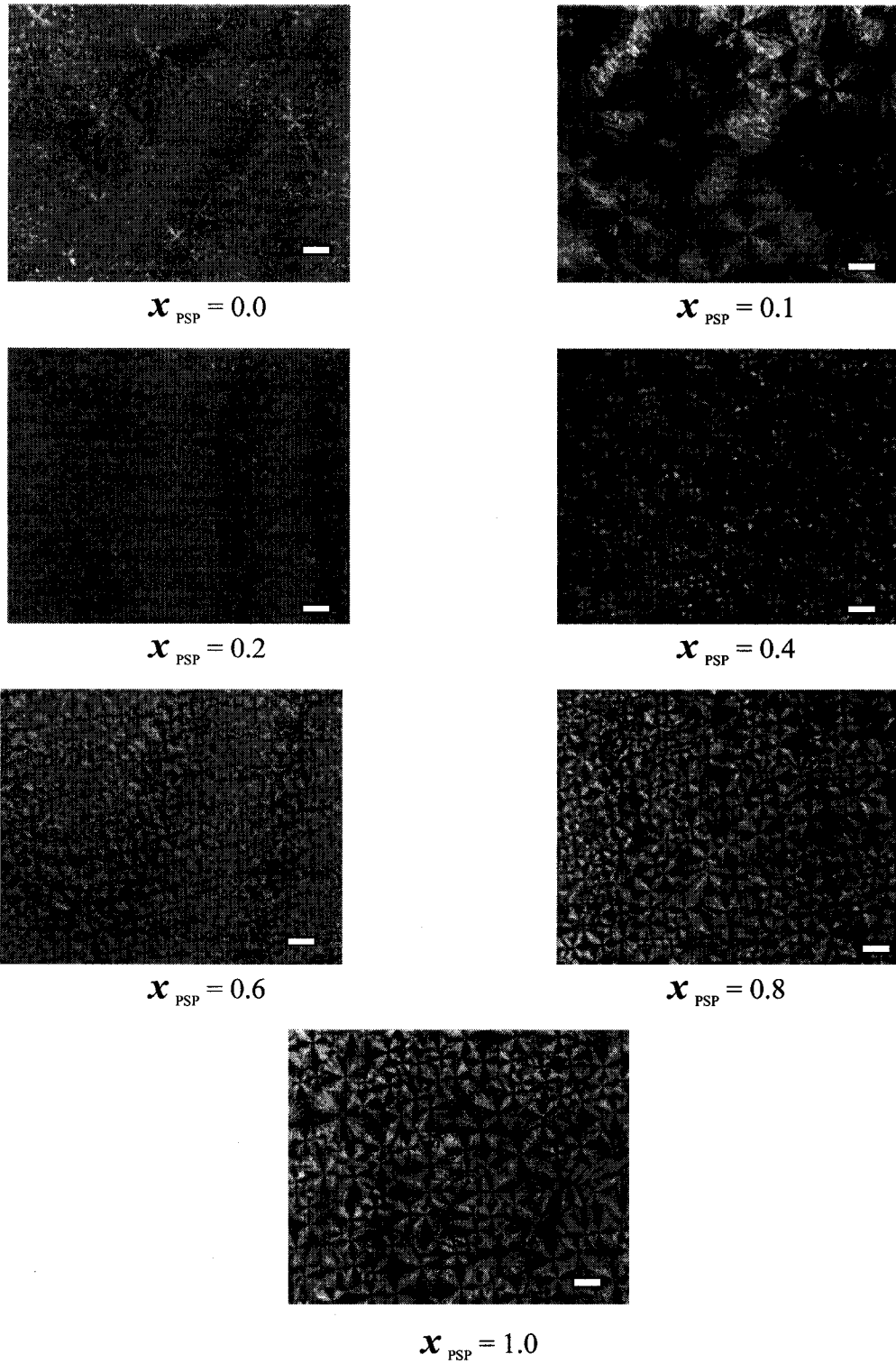


Figure 4-9. Microstructure of pure and binary mixtures of PSP and PPS crystallized at 3.0 °C/min. Magnification = 100 x. Bar =1 μm

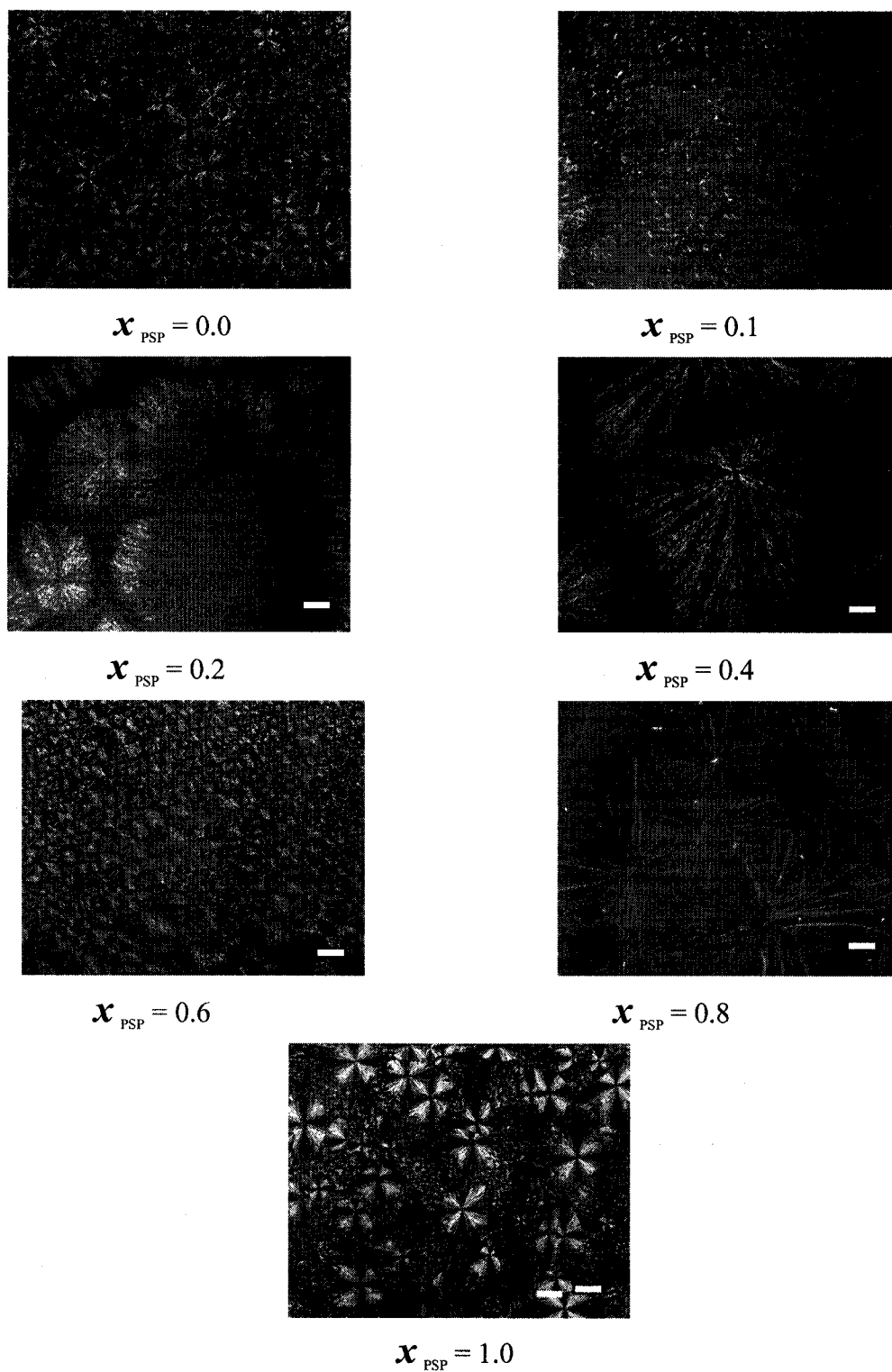


Figure 4-10. Microstructure of pure and binary mixtures of PSP and PPS crystallized at 0.1 °C/min. Magnification = 100 x. Bar =1 μm

x_{PSP} followed by a mix of small and large crystallites for 1.0 x_{PSP} . Cooling rate therefore has a marked impact upon microstructure; however this does not correlate with changes seen in hardness and SFC. At the eutectic point however, at both cooling rates, the change in microstructure clearly deviated from the general trends seen. The different geometric patterns of growth observed in the microstructures may have contributed to the small non integer changes observed in the Avrami index n discussed earlier.

4.4. Conclusion

The phase behavior of the binary mixture of 1,3-dipalmitoyl-2-stearoyl-*sn*-glycerol and 1,2-dipalmitoyl-3-stearoyl-*sn*-glycerol has been studied using XRD, DSC, SFC, relative hardness and microscopy providing insight into the crystallization processes that ranges from molecular to macroscopic levels.

The XRD spectra of the pure PSP and PPS samples indicate the α polymorph was crystallized at both 3.0 °C/min and 0.1 °C/min. Phase diagrams constructed from DSC data indicated a eutectic behavior at both cooling rates. The application of a thermodynamic model based on the Hildebrand equation indicated that PSP and PPS are immiscible in the solid state. This finding provided a key insight into the interpretation of the XRD for the binary mixtures, as it can be inferred the XRD spectra for the mixtures are merely a superposition of XRD spectra resulting from domains of pure PSP and domains of pure PPS. During heating, the α polymorph transformed to the β' polymorph via melt mediated transformation. Final SFC (%) correlated with relative hardness; however no softening or SFC (%) depression was associated with the eutectic composition of 0.2 x_{PSP} . Two distinct segments or kinetic steps were observed for SFC (%) versus time curves; however Avrami treatment of these curves revealed very similar growth modes ($n \sim 1$) despite different growth rates. Variations in microstructure were observed which did not necessarily evolve a specific feature as a function of PSP composition particularly at the 0.1 °C/min rate. However, at the eutectic composition at both cooling rates, very distinct microstructures were observed.

4.5. References

- Bentley, P.H., McCrae, W., 1970. An Efficient Synthesis of Symmetrical 1,3 Diglycerides. *Journal of Organic Chemistry* 35, 2082-2083.
- Gibon, V., Durant, F., Deroanne, C., 1986. Polymorphism and intersolubility of some palmitic, stearic, and oleic triglycerides: PPP, PSP, and POP. *Journal of American Oil Chemists' Society* 63, 1047-1055.
- Humphrey, K.L., Narine, S.S., 2004. A comparison of lipid shortening functionality as a function of molecular ensemble and shear: Crystallization and melting. *Food Research International* 37, 11-27.
- Inoue, T., Motoda, I., Hiramatsu, N., Suzuki, M., Sato, K., 1993. Phase behavior of binary mixture of palmitoleic acid (cis-9-hexadecenoic acid) and asclepic acid (cis-11-octadecenoic acid). *Chemistry and Physics of Lipids* 66, 209-14.
- Lee, A.G., 1977. Lipid phase transitions and phase diagrams. II. Mixtures involving lipids. *Biochimica et Biophysica Acta, Reviews on Biomembranes* 472, 285-344.
- MacNaughtan, W., Farhat, I.A., Himawan, C., Starov, V.M., Stapley, A.G.F., 2006. A differential scanning calorimetry study of the crystallization kinetics of tristearin-tripalmitin mixtures. *Journal of American Oil Chemists' Society* 83, 1-9.
- Narine, S.S., Humphrey, K.L., Bouzidi, L., 2006. Modification of the Avrami model for application to the kinetics of the melt crystallization of lipids. *Journal of the American Oil Chemists' Society* 83, 913-921.
- Timms, R., 2003. Physical Chemistry. In: *The Confectionary Fats Handbook: Properties, Production, and Application* The Oily Press, Bridgewater, pp. 9-63.
- van Langevelde, A., van Malssen, K., Sonneveld, E., Peschar, R., Schenk, H., 1999. Crystal packing of a homologous series beta prime-stable triacylglycerols. *Journal of American Oil Chemists' Society* 76, 603-609.
- Yang, C.P., Nagle, J.F., 1988. Phase transformations in lipids follow classical kinetics with small fractional dimensionalities. *Physical Review A: Atomic, Molecular, and Optical Physics* 37, 3993-4000.

5. General Conclusions

The objectives of this study as listed in Chapter 1 will now be re-visited and discussed based on the findings of Chapters 2, 3 and 4. The results from each binary TAG system studied will be compared and correlations between the various analytical techniques inferred for each system.

The metastable α and β' polymorphs were observed for these systems as determined by XRD. During melting however, transformations to more thermodynamically stable polymorphs occurred. The α polymorph was formed for the PSP/PPS system and the β' polymorph was formed for the LSL/LLS systems at both 0.1 and 3.0 °C/min cooling rates. For the MSM/MMS system, the α polymorph was formed at 3.0 °C/min and the β' polymorph was formed at 0.1 °C/min. This trend shows that as chain length mismatch (CLM) increases in the sequence PSP/PPS \rightarrow MSM/MMS \rightarrow LSL/LLS, the formation of the more thermodynamically stable polymorph (β') is favored. The MSM/MMS system which has a CLM of 4 (between the PSP/PPS (CLM =2) and LSL/LLS (CLM =6) forms both polymorphs depending upon the cooling rate. It seems that greater chain length mismatch allows for more overlap of the triacylglycerol chains at the methyl terrace forming a more closely packed structure. In each binary system, similar polymorphism, stacking mode and angles of tilt (in the case of β') were observed for all the mixtures indicating similar sub cells and lamellar packing. Furthermore, the symmetric and asymmetric TAGs were not discernable based on their XRD spectra.

The melting thermograms for the pure symmetric and asymmetric TAGs are shown in Figure 5-1. A single main melting peak is seen for all symmetric TAGs, at both cooling rates. The melting temperature of this main melting peak increases as the chain length of the substituted fatty acid is increased. Longer chain lengths allow for greater Van-der-Waals interactions between the chains. For the asymmetric TAGs, more complex melting behavior is observed. For all samples except LLS at 0.1 °C/min, multiple melting peaks (endotherms) are observed which are mediated by crystallization peaks (exotherms). This is referred to as melt mediated polymorphic transformation,

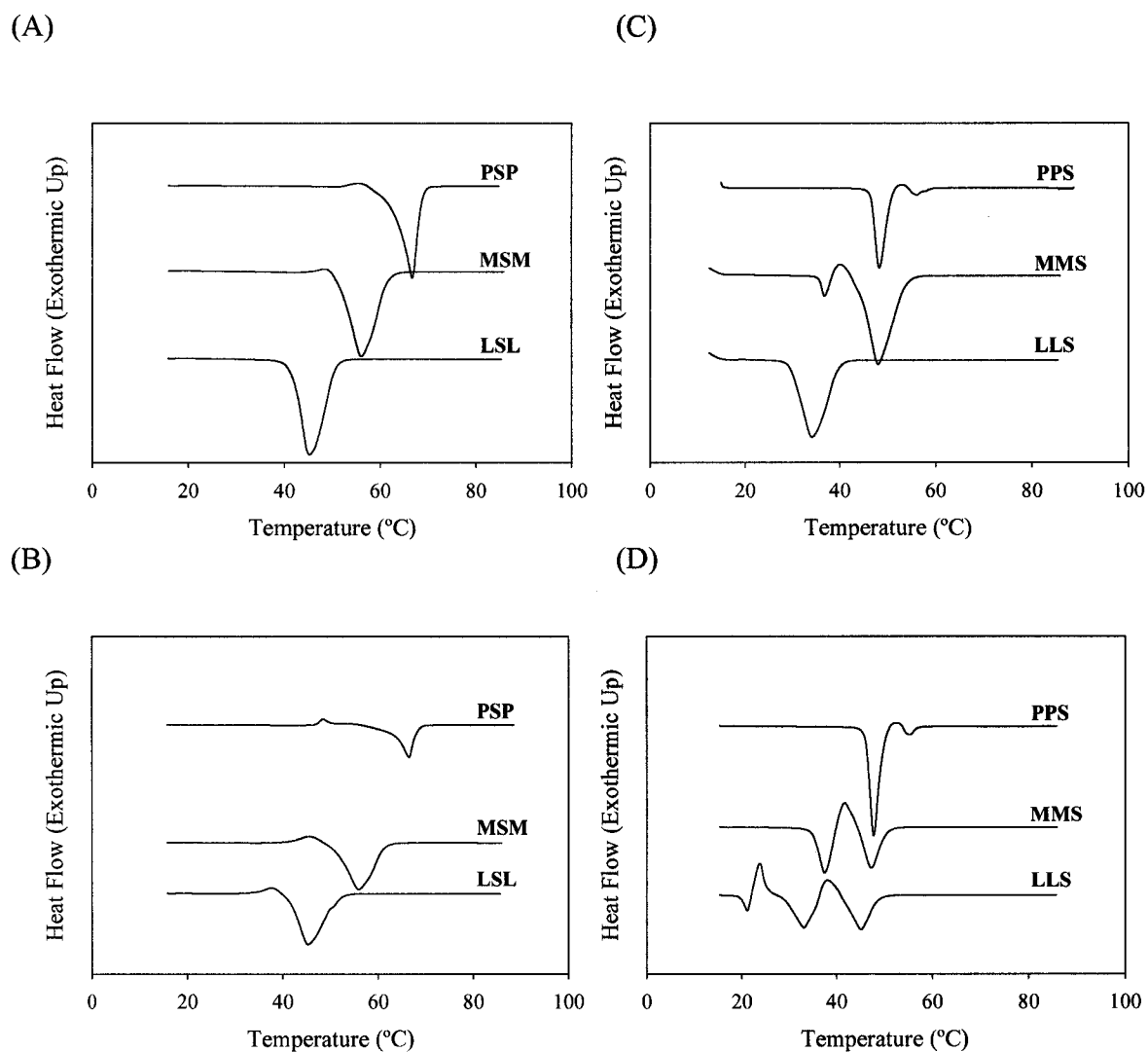


Figure 5-1. Melting curves (5.0 °C/min) of pure TAGs at 0.1 and 3.0 °C/min (A) Melting curves of LSL, MSM and PSP at 3.0 °C/min (B) Melting curves of LLS, MMS and PPS at 3.0 °C/min (C) Melting curves of LSL, MSM and PSP at 0.1 °C/min (D) Melting curves of LLS, MMS and PPS at 0.1 °C/min.

where the thermodynamically less stable polymorph melts and recrystallizes to a more stable form due to increased molecular mobility. The main difference observed between the symmetric and asymmetric TAGs in melting behavior is due to differences in packing during crystallization. Better interactions about the glycerol moiety in the symmetric TAGs may hinder polymorphic transformations (Elisabettoni et al., 1998).

As seen in the melting profile of the asymmetric TAGs, lower melting peaks are present despite XRD indicating that a single polymorph was formed. The non-detection of the less stable α polymorph may be due to its relative instability as well as presence in a small concentration.

The melting behavior of pure LLS is most interesting (Figure 5-1 (B)). At 3.0 °C/min, the three melting peaks are observed which can be attributed to α , β' , and β in order of increasing melting points. When cooled at 0.1 °C/min however (Figure 5-1 (D)), a single melting peak is observed which represents melting of the β' polymorph as shown by XRD. In the case of the 3.0 °C/min crystallization rate, the difference in free energy between the α and β' polymorphs may act as a driving force for the formation of the β polymorph (Sato, 1999). At the 0.1 °C/min cooling rate, the melting of an α polymorph was notably absent and the β' polymorph melted without transforming to the β polymorph. For MMS, two melting peaks were seen for both cooling rates; at 3.0 °C/min they were of similar area while at 0.1 °C/min the area of the lower melting peak was smaller than the area of the higher melting peak. The slower cooling rate would favor the formation of a more thermodynamically stable polymorph as longer time is spent at higher temperatures which possibly explains the difference in peak areas. Cooling rate did not influence melting behavior of the PPS sample which has the highest crystallization temperature. Based on the melting behavior observed for the asymmetric TAGs, it seems that a lower inertial mass favors polymorphic transformations during melting. In the case of MMS and PPS even at the 0.1 °C/min cooling rate, melt mediated transformations were still observed.

The phase diagrams created using DSC data of the LSL/LLS and PSP/PPS binary systems demonstrated eutectic behavior while MSM/MMS was monotectic (see Table 5-1). The eutectic phase behavior observed lends support to the hypothesis that positional

isomers can form eutectics. A thermodynamic model based on the Hildebrand equation was used to model the phase boundaries of the phase diagram. The non ideality of mixing parameter ρ was determined using the so called Bragg – Williams approximation. The ρ values for the solid (ρ_s) and liquid (ρ_L) states are presented in Table 5-1. They indicated that these systems are miscible in the liquid state (ρ_s negative) but immiscible in the solid state (ρ_L positive). Crystallization rate was observed to shift the eutectic composition in the LSL/LLS system from 0.1_{LSL} (3.0 °C/min) to 0.2_{LSL} (0.1 °C/min). This is possible since all mixtures crystallized in metastable states. A summary of the phase behavior is shown in Table 5-1.

SFC was monitored as a function of time and two distinct growth segments were observed for all samples except 0.1_{LSL} (at 3.0 °C/min) which had three segments and corresponded to the eutectic point. For all samples, the segments of the SFC – time curves were fitted to a modified form of the Avrami equation (Narine et al., 2006). For these segments, the so-called Avrami constant A was determined (a function of the nucleation and growth constants), and the so-called Avrami index n (a function of the number of dimensions in which growth takes place). The determined n values were found to be between 1-2. However their variations did not reveal a definite trend nor did they support the spherulitic growth which was observed for the majority of samples. The non – correlation between the n – values and morphology observed may be due to changing rates of radial growth, geometric restrictions to domain growth, polymorphic changes during crystallization, localized re-melt among other reasons (Narine et al., 2006; Yang and Nagle, 1988). $n \geq 3$ corresponds to a spherulitic growth while $n = 1$ corresponds to a rod – like growth from instantaneous nuclei and $n = 2$ to a rod – like growth from sporadic nuclei (Sharples, 1966).

Final SFC achieved by the symmetric TAGs was higher than the asymmetric TAG for both crystallization rates except for the MSM/MMS system at 3.0 °C/min where the converse was seen. Depressions in SFC were encountered for MSM/MMS and PSP/PPS systems at 0.1°C/min (Figure 5-2.(A)) and for all three systems at 3.0 °C/min (Figure 5-2.(B)). In the MSM/MMS system, the depression in SFC was shifted with cooling rate.

System	Phase Behavior		ρ (kJ/mol)	
	0.1 °C/min	3.0 °C/min	ρ_S	ρ_L
LSL/LLS x_{LSL}	Eutectic 0.2	Eutectic 0.1	+3.9	-1.2
MSM/MMS x_{MSM}	Monotectic	Monotectic	+2.6	+1.5
PSP/PPS x_{PSP}	Eutectic 0.2	Eutectic 0.2	+3.6	-0.9

Table 5-1. Summary of phase behavior and ρ values for the solidus and liquidus lines for the LSL/LLS, MSM/MMS and PSP/PPS binary systems.

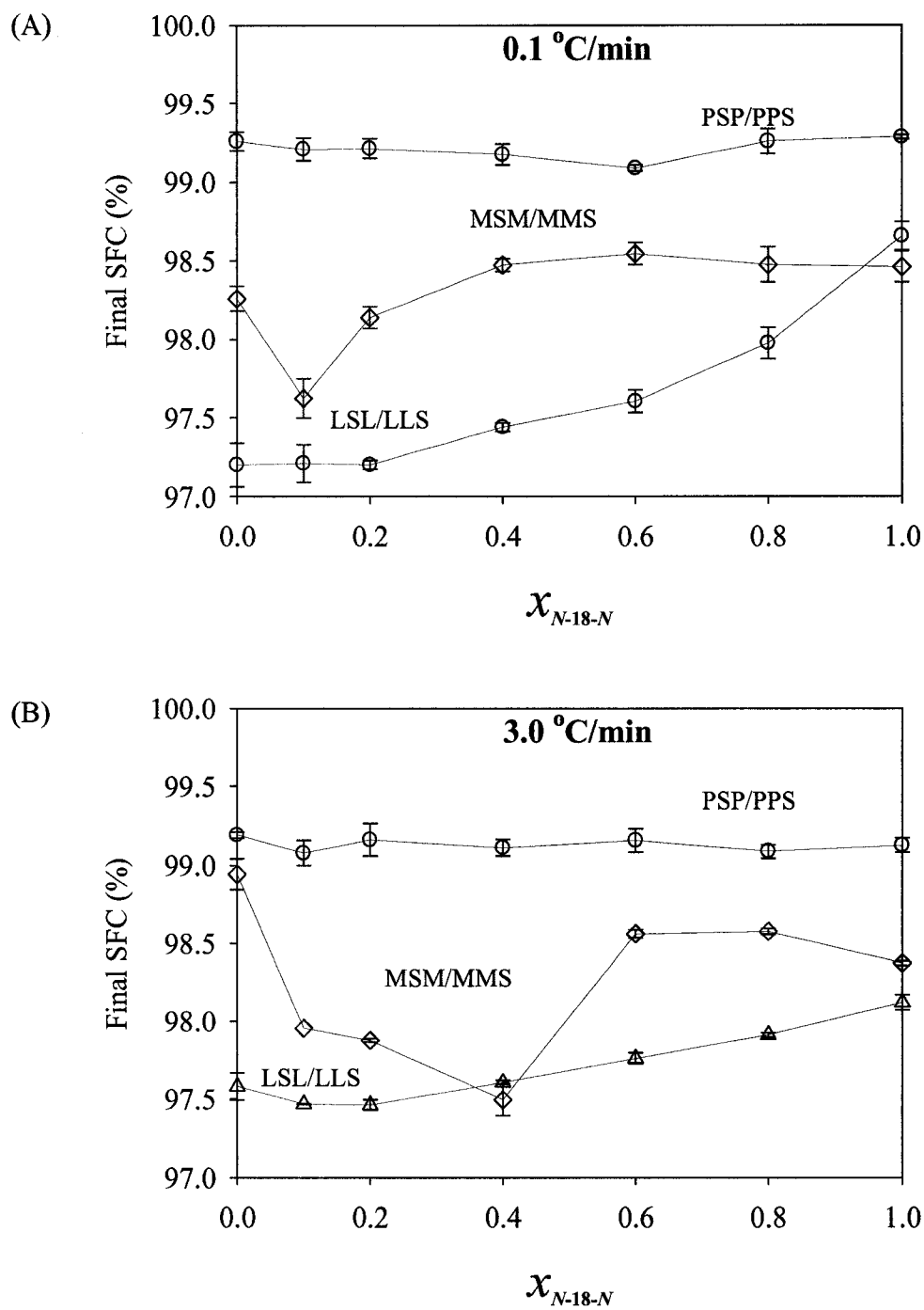


Figure 5-2. Final (%) SFC vs. (LSL, MSM, PSP) molar composition (A) Final (%) SFC vs. (LSL, MSM, PSP) molar composition at 0.1 °C/min (B) Final (%) SFC vs. (LSL, MSM, PSP) molar composition at 3.0 °C/min

The shift of the strongest depression from 0.4_{MSM} (3.0 °C/min) to 0.2_{MSM} (0.1 °C/min) would seem to be motivated by the reversal in SFC as a function of rate as seen for the pure samples, i.e. the depression at the slower cooling rate is motivated by the MMS phase.

Relative hardness measurements indicated softening and hardening effects (Figure 5-3) which did not necessarily correlate with the eutectic point or with the depressions in SFC. The PSP/PPS system was relatively the hardest followed by the MSM/MMS and LSL/LLS systems. In the case of the PSP/PPS system, SFC depression correlated with a softening effect at the 0.6_{PSP} molar composition. However there was no general correlation between the eutectic composition, SFC depression and relative hardness. Table 5-2 summarizes the correlations seen between the eutectic point, SFC and hardness.

The non – correlation between SFC and the eutectic point can be explained by the temperature at which each measurement was taken. In this study, the final SFC was taken at 15 °C, while the eutectics were seen above 20 °C in the LSL/LLS and PSP/PPS systems. Relative hardness is however dependent upon the relative strengths of the links between the crystal aggregates or spherulite (interparticle) (Shi et al., 2005). It must be noted however, that SFC and melting point are not always insensitive indicators of relative hardness.

Variations were observed in the morphologies, crystallite size and distribution in the crystal networks for all the samples. Spherulitic growth with its characteristic Maltese crosses was seen for all pure samples as shown in Figures 5-4.(A), (B) and (C) for pure LSL/LLS, MSM/MMS and PSP/PPS respectively.. The symmetric TAGs formed more distinct spherulites than the asymmetric TAGs. As expected, larger and fewer crystal entities were formed for the lower 0.1 °C/min crystallization rate. Differences in morphology would explain why there were variations in SFC and hardness; however no direct links could be made between a particular feature and property except for the MSM and MMS samples at 3.0 °C/min (Figure 5-4.(B)), where the microstructure suggests that MSM traps more liquid oil than MMS and thus its lower SFC.

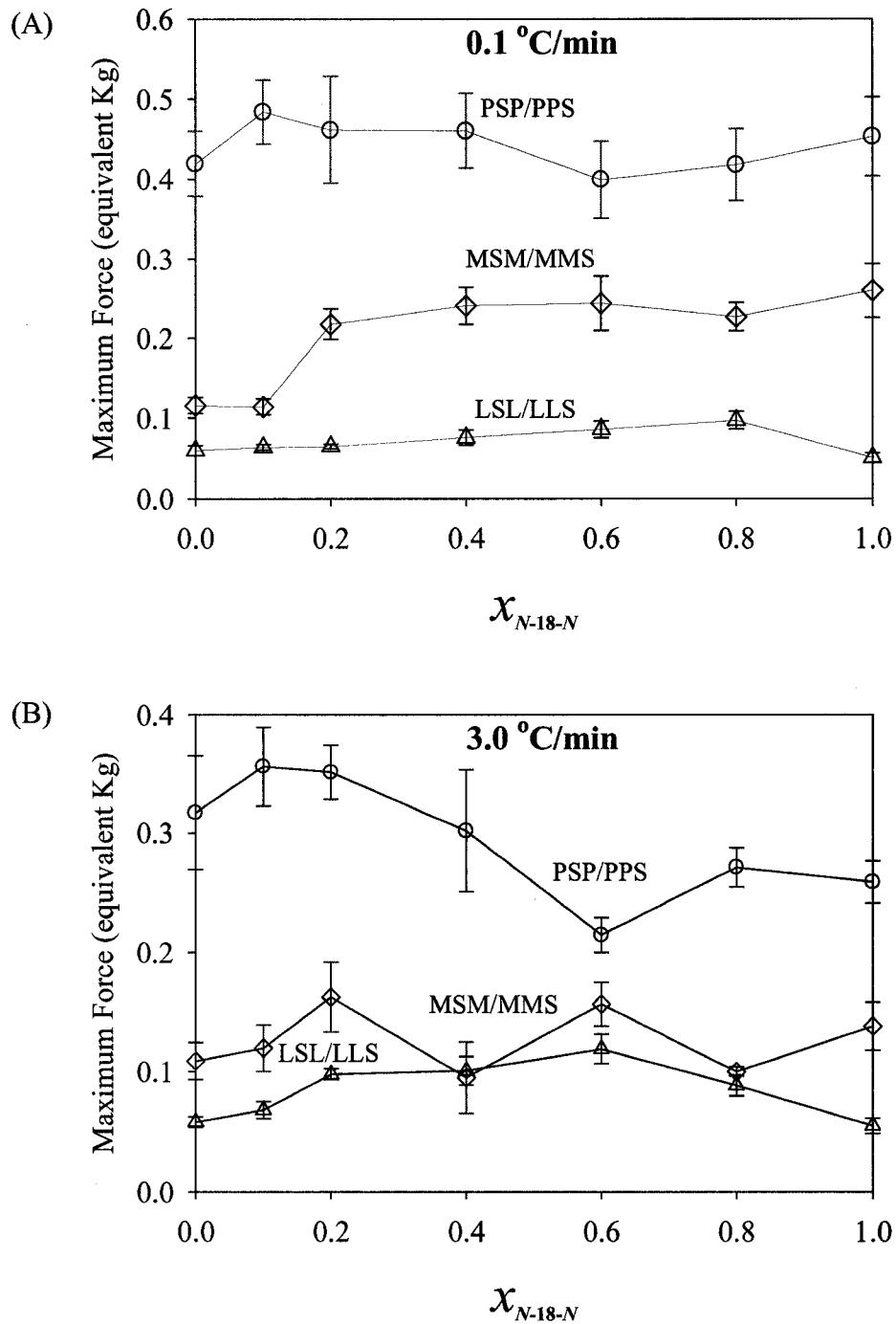
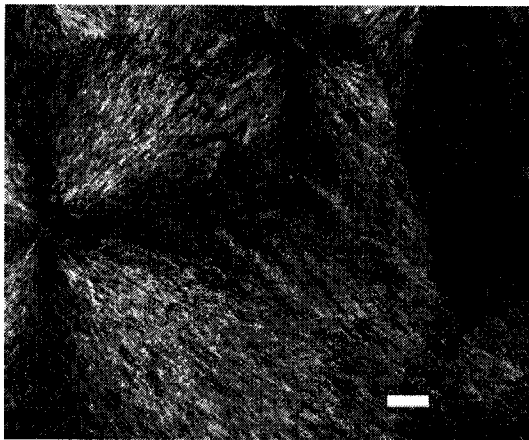


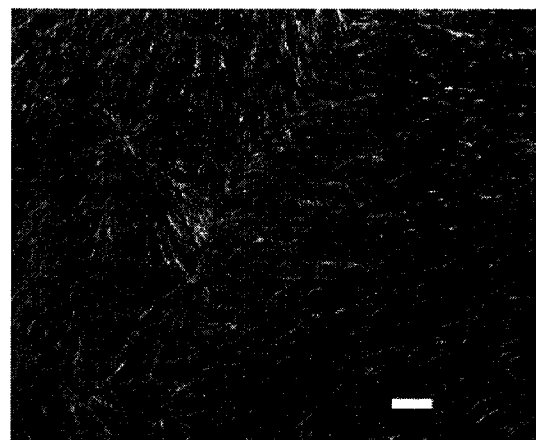
Figure 5-3. Relative hardness vs. (LSL, MSM, PSP) molar composition (A) Relative hardness vs. (LSL, MSM, PSP) molar composition at 0.1 °C/min (B) Relative hardness vs. (LSL, MSM, PSP) molar composition at 3.0 °C/min.

Analytical Technique	LSL/LLS x_{LSL}	MSM/MMS x_{MSM}	PSP/PPS x_{PSP}
0.1 °C/min			
DSC	0.1	Monotectic	0.2
SFC	No depression	0.1, 0.2	0.1, 0.2, 0.4, 0.6
Hardness	No softening	No softening	0.6
3.0 °C/min			
DSC	0.1	Monotectic	0.2
SFC	0.1, 0.2	0.1, 0.2, 0.4	No depression
Hardness	No softening	No softening	No softening

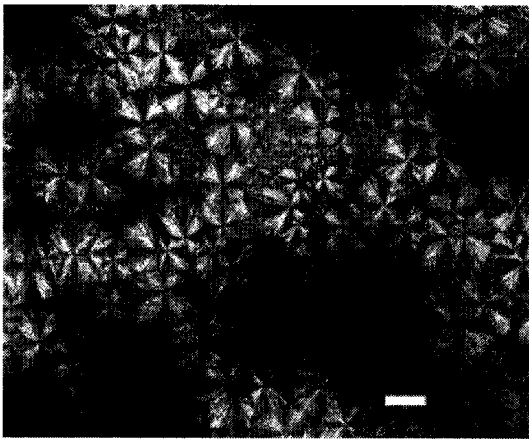
Table 5-2. Summary of correlations between eutectic composition, depressions in SFC and relative hardness at 0.1 and 3.0 °C/min.



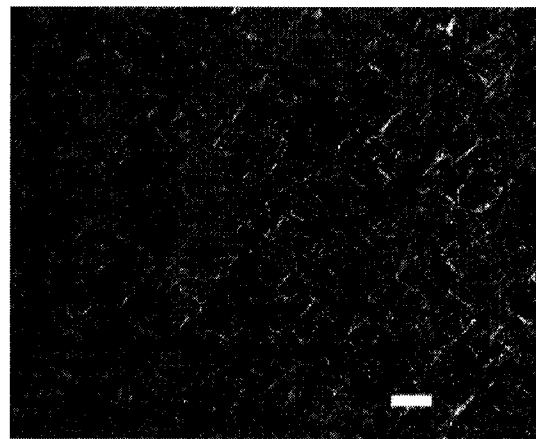
LSL – 0.1 °C/min



LLS – 0.1 °C/min

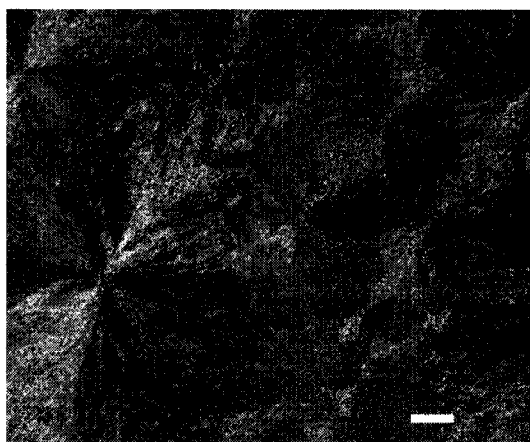


LSL – 3.0 °C/min



LLS – 3.0 °C/min

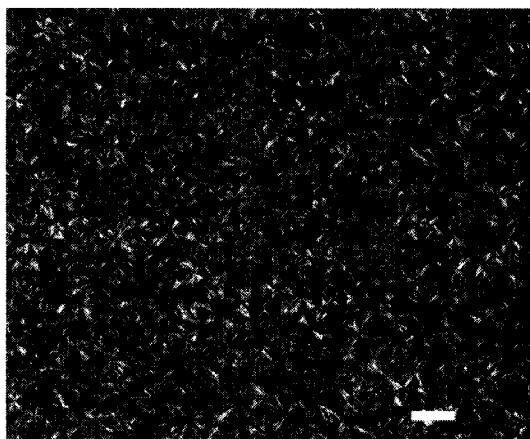
Figure 5 – 4. (A) Microstructure of LSL and LLS crystallized at 0.1 and 3.0 °C/min. Magnification = 100x. Bar = 1 μ m.



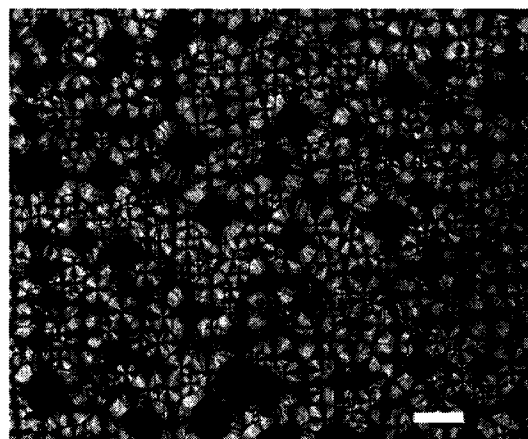
MSM – 0.1 °C/min



MMS – 0.1 °C/min

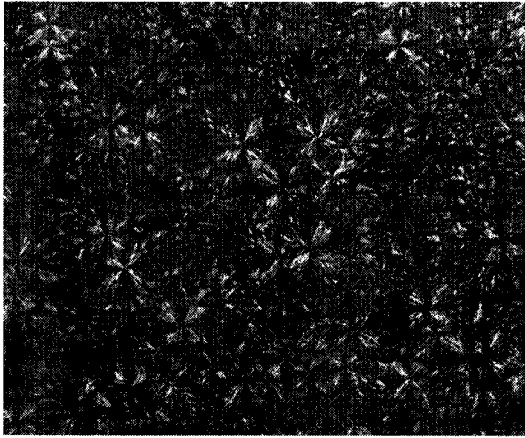


MSM – 3.0 °C/min



MMS – 3.0 °C/min

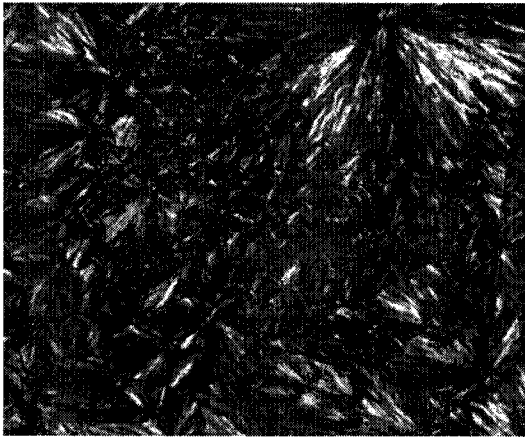
Figure 5 – 4. (B) Microstructure of MSM and MMS crystallized at 0.1 and 3.0 °C/min. Magnification = 100x. Bar = 1 μ m.



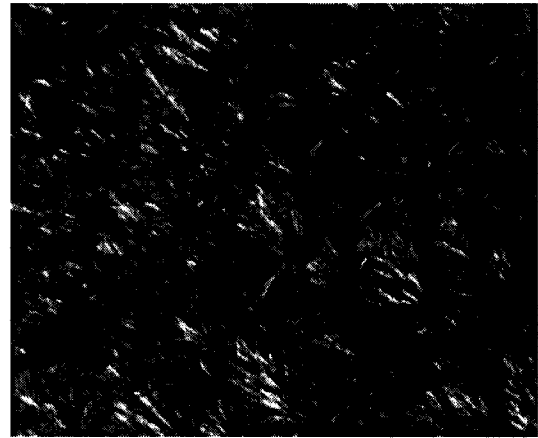
PSP – 0.1 °C/min



PPS – 0.1 °C/min



PSP – 3.0 °C/min



PPS –3.0 °C/min

Figure 5 -4. (C) Microstructure of PSP and PPS crystallized at 0.1 and 3.0 °C/min. Magnification = 100x. Bar = 1 μ m.

In the palmitic system, the differences between symmetric and asymmetric TAGs and crystallite size as a function of crystallization rate were not as pronounced as for the other two systems. Again this may be due to a small chain length mismatch and high inertial mass which do not favour dense packing. Recall that this system crystallized exclusively in the least densely packed α polymorph.

The results of this study suggests that “softening” or melting point depressions which are encountered in low trans – interesterified shortening systems as a result of the introduction of positional isomers, may be mitigated by processing solutions, without resorting to adding significant amounts of saturated fat. It is recommended that a homologous series of positional isomers of TAGs be investigated, so that a trend can be established. It would also be particularly interesting to study systems which melt close to room temperature (e.g. CSC/CCS and CiSCi/CiCiS), as eutectic effects are generally most undesirable in this temperature range. The crystallized pure and binary TAG mixtures should also be held isothermally for longer periods of time to allow the system to attain a state closer to equilibrium.

The result of this study does not disprove the hypothesis that positional isomerism and chain length mismatch lead to the formation of eutectics. The MSM/MMS system was different as it demonstrated monotectic behaviour, while PSP/PPS and LSL/LLS which have the lowest and highest chain length mismatch respectively demonstrated eutectic behaviour. The results of this study indicate the need to approach phase behavior studies using a number of tools which target and examine different levels of structure.

5.1. References

- Elisabettini, P., Lognay, G., Desmedt, A., Culot, C., Itasse, N., Deffense, E., Durant, F., 1998. Synthesis and physiochemical characterization of mixed acid triglycerides that contain elaidic acid. *Journal of American Oil Chemists' Society* 75, 285-291.
- Narine, S.S., Humphrey, K.L., Bouzidi, L., 2006. Modification of the Avrami model for application to the kinetics of the melt crystallization of lipids. *Journal of American Oil Chemists' Society* 83, 913-921.
- Sato, K., 1999. Solidification and phase transformation behaviour of food fats- a review. *Fett/Lipid* 101, 467-474.
- Sharples, A., 1966. Overall Kinetics of Crystallization. In: *Introduction to Polymer Crystallization*. Edward Arnold, London, pp. 44-59.
- Shi, Y., Boamin, L., Hartel, R.W., 2005. Crystal Morphology, Microstructure and Textural Properties of Model Lipid Systems. *Journal of American Oil Chemists' Society* 82, 399-408.
- Yang, C., Nagle, J., 1988. Phase transformations in lipids follow classical kinetics with small fractional dimensions. *Physical Review A* 37, 3993-4000.